DIRECT NUMERICAL SIMULATIONS OF FLUID-STRUCTURE INTERACTION IN THE RESPIRATORY AIRWAYS

by

Andriy Roshchenko

A thesis submitted in partial fulfillment of the requirements for the degree of

Doctor of Philosophy

in

Applied Mathematics

Department of Mathematical and Statistical Sciences
Department of Mechanical Engineering
University of Alberta

Abstract

This thesis presents recent developments in direct numerical simulations of fluid-structure interaction occurring in biological systems, with particular interest in the modeling of particle deposition within the human respiratory system.

Two numerical techniques are proposed. The first one is intended for direct numerical simulations of solid high aspect ratio micro-fibers in a general Newtonian fluid flow. For efficient and accurate resolution of the microscales, a micro-grid rigidly attached to the fiber in its spatial motion is introduced. The entire problem on the micro-grid is transformed with an Arbitrary Lagrangian-Eulerian method to a fixed reference domain and then solved with a Fictitious Domain Method. Using this algorithm, rotational behavior of fibers in a linear shear flow is studied. In view of our analysis, it is suggested that respiratory tract deposition for high aspect ratio fibers with complex shapes will be enhanced compared with the deposition of simple ellipsoidal fibers. Additionally, study of deposition enhancement due to magnetic field alignment of long straight ellipsoids in realistic airway bifurcation is performed. Results indicate that magnetic alignment of such particles can increase deep lung deposition by a factor of 1.42–3.46 depending on the fiber aspect ratio.

A second method is developed to allow direct numerical simulations of dynamical interaction between an incompressible fluid and a hyper-elastic incompressible solid. A Fictitious Domain Method is applied so that the fluid is extended inside the deformable solid volume and the velocity field in the entire computational domain is resolved in an Eulerian framework. Solid motion, which is tracked in a Lagrangian framework, is imposed through the body force acting on the fluid within the solid boundaries. Solid stress smoothing on the Lagrangian mesh is performed with a Zienkiewicz-Zhu patch recovery method. High-order Gaussian integration quadratures over cut elements are used in order to avoid sub-meshing within elements in the Eulerian mesh that are intersected by the Lagrangian

grid. The method is validated against previously reported results on numerical simulations of 3-D rhythmically contracting alveolated ducts. Observed flow patterns and alveolus dynamics for breathing conditions and geometrical parameters corresponding to different acinar generations in the respiratory system are comparable to those reported previously. This suggests that our new formulation can be successfully applied to numerical studies of coupled dynamics of air and airway walls in distal regions of the lungs.

Preface

Chapter 3 of this thesis is based on two papers previously published as:

- A. Roshchenko, W. H. Finlay, and P. D. Minev. The Aerodynamic Behavior of Fibers in a Linear Shear Flow. *Aerosol Science and Technology*, 45(10):1260–1271, Oct. 2011. I contributed by developing the numerical technique and implementing it in a computer code; I performed data acquisition and analysis as well as the manuscript composition. W. H. Finlay and P. D. Minev were the supervisory authors and were involved with concept formation and manuscript composition. W. H. Finlay assisted with results interpretation, while P. D. Minev contributed to numerical method development.

- R. C. Martinez, A. Roshchenko, P. D. Minev, and W. H. Finlay. Simulation of enhanced deposition due to magnetic field alignment of ellipsoidal particles in a lung bifurcation. *Journal of Aerosol Medicine and Pulmonary Drug Delivery*, 26(1):31–40, Feb. 2013.

  R. C. Martinez performed data acquisition and analysis as well as the manuscript composition. I contributed by developing the numerical method and computer code for the experiment and assisted with manuscript edits. P. D. Minev contributed to numerical method development and manuscript edits. W. H. Finlay was the supervisory author and was involved with concept formation and manuscript composition.

Review of the Fictitious Domain Method in chapter 2, development of the numerical technique and its verification in chapter 4 as well as concluding analysis in chapter 5 are my original research conducted under the supervision of P. D. Minev and W. H. Finlay.

To my parents Mykola Roshchenko and Svitlana Roshchenko. For their love and their support which gave me the courage to follow my dreams.

Присвячується моїм батькам, Миколі Рощенко та Світлані Рощенко. За їх любов і підтримку, що дали мені сміливості слідувати за моїми мріями.

Acknowledgements

It is with a great pleasure I would like to thank my supervisors Dr. Peter D. Minev and Dr. Warren H. Finlay for their mentorship and support during my graduate studies. I am grateful to them for their ideas and expert knowledge which they so readily shared with me whenever I encountered difficulties in my research and needed an advise. I consider myself very lucky to have them as my supervisors because it is for them my graduate school experience was very enjoyable.

I would like to thank members of my examining committee Professors Bin Han, Yaushu Wong, Marc Secanell Gallart and Mohammad Mofrad for providing their valuable feedback and asking insightful questions contributing to the quality of my thesis.

I wish to thank my dear friends Mehdi Azhdarzadeh and Laleh Golshahi from the Aerosol Research Laboratory of Alberta for been there for me whenever I needed time off from my studies.

Many thanks to Tara Schuetz, Graduate Coordinator at the Department of Mathematical and Statistical Sciences, for her cheer and smile and for the great professionalism while helping students with all the administrative aspects of the graduate school.

Finally, I wish to thank my family, my parents Mykola and Svitlana and my sister Tanya for been loving and supporting in everything I did. Special thanks to my beautiful lovely wife Maryna for her love, encouragement and patience, I love you very much.

Contents

List of Tables

List of Figures

Chapter 1

Introduction

We know that particle deposition behavior in the respiratory system is influenced by a combination of natural factors. Among them we can distinguish major aspects that include biological aspects determining respiratory system morphology, airway tissue composition and characteristics of the breathing cycle, and mechanical aspects determining coupled air and tissue dynamics, aerosol properties (particles shapes, densities, concentrations) and deposition mechanisms.

1.1 Respiratory system

Morphology of the respiratory system is typically described using morphometric lungs models which simplify and unify complicated real airway geometries being unique for each organism. Such models usually cover the tracheobronchial region of the respiratory system, which includes the trachea and all lung airways responsible for air transport, and the acinar region, which includes the respiratory bronchioles, alveolar ducts and terminal alveoli – the region with the largest volume and the place where gas exchange occurs in the lungs, see Figure 1.1. Referring to these two regions together they are called *thoracic* region of the respiratory system.

The third major region of the respiratory system is usually called *extrathoracic* region and it includes the oral and nasal cavities and the throat, which in turn is composed of the larynx and pharynx [Finlay, 2001].

The main function of the extrathoracic and tracheobronchial regions is to deliver air to the acinar region while filtering it from the foreign objects, such as particles or bacteria, on the way.

Morphometric lung models commonly adopt simple dichotomous splitting of a parent

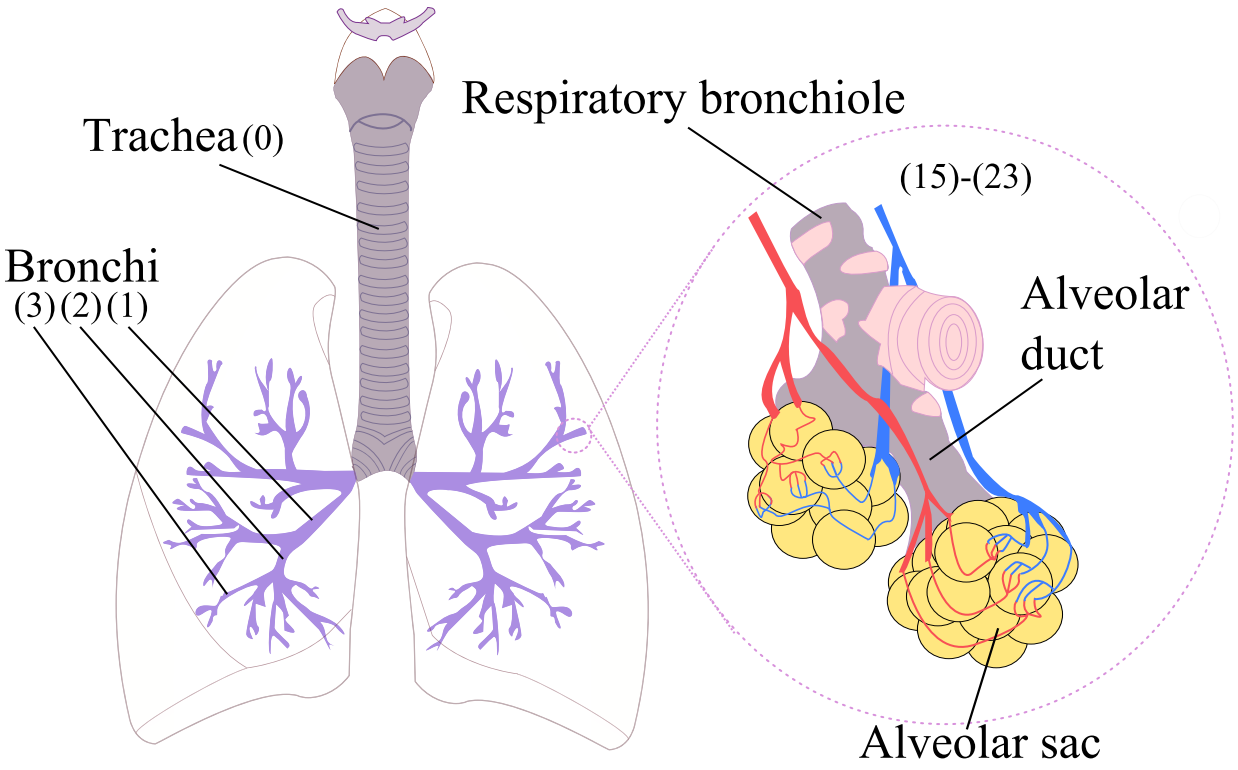

Figure 1.1: Schematic of lung morphology for tracheobronchial and acinar regions. Lung generations are marked according to Table 1.1. *Source: Wikipedia. Author: Rastrojo.*

airway into two daughter branches. Some models assume symmetric branching into two equal airways [Haefeli-Bleuer and Weibel, 1988; Finlay et al., 2000], while other models account for observed lung asymmetry and assume daughter airways with different diameters [Horsfield et al., 1971; Yeh and Schum, 1980].

In order to establish the relative location of airways with respect to each other, morphometric lung models assign a specific index to each airway generation indicating the number of dichotomous bifurcations preceding the airway. Thus, the trachea has generation number 0, it bifurcates into two bronchi with generation number 1 which are followed by four daughter airways of generation 2, *etc.*, see Figure 1.1, and refer to Table 1.1 for a complete set of morphological parameters and airway numbering based on [Finlay et al., 2000].

Customarily, the acinar region is numbered as well, such that indexes between 0 and 3 correspond to partly alveolated respiratory bronchioles and indexes between 4 and 8 to alveolar ducts ending with alveolar sacs. For example, zero acinar generation $z' = 0$ corresponds to generation number 15 in the symmetric lung model [Finlay et al., 2000], Table 1.1.

Generation		Number	Diameter	Length	Volume	Re
Lung	Acinar		(mm)	(mm)	(cm^3)	
0		1	18.1	124.5	32.1	1406.9
1		2	14.1	36.1	11.4	903
2		4	11.2	28.6	11.2	568.4
3		8	8.85	22.8	11.2	359.7
4		16	7.06	17.8	11.1	225.4
5		32	5.65	11.3	9	140.8
6		64	4.54	8.97	9.3	87.6
7		128	3.64	8.28	11	54.7
8		256	2.86	7.45	12.2	34.8
9		512	2.18	6.53	12.5	22.8
10		1,024	1.62	5.55	11.8	15.4
11		2,048	1.21	4.54	10.7	10.3
12		4,096	0.92	3.57	9.7	6.76
13		8,192	0.73	2.77	9.5	426
14		16,384	0.61	2.19	10.5	2.55
15	0	32,768	0.49	1.34	21.8	1.59
16	1	65,536	0.48	1.09	34.9	0.81
17	2	131,072	0.39	0.91	44.2	0.5
18	3	262,144	0.39	0.81	73.8	0.25
19	4	524,288	0.35	0.68	116.2	0.14
20	5	1,048,576	0.33	0.68	215.8	0.07
21	6	2,097,152	0.3	0.68	377.8	0.04
22	7	4,194,304	0.28	0.65	675	0.02
23	8	8,388,608	0.24	0.73	1257.3	0.01

Table 1.1: Airway morphology parameters, Reynolds numbers (calculated for inhalation flow rate of 18 liters/min), and the corresponding generation volumes of the symmetric lung geometry based on [Finlay et al., 2000].

In addition to the aforementioned symmetric lung model by [Finlay et al., 2000], another widely used model is the so called symmetric Weibel A model described in [Haefeli-Bleuer and Weibel, 1988]; among asymmetric models, it is worth noting the morphometric description by [Yeh and Schum, 1980]. All models provide geometrical parameters, including airway diameters, lengths; some of them additionally provide branching angles and angles of inclination to gravity, which are useful for estimating inhaled particle sedimentation.

1.2 Particle deposition

1.2.1 Experimental approach

Experimental *in–vivo* studies of aerosol deposition in human or animal subjects have been successful in determining cumulative (total) deposition of selected aerosols, but at the same time they have many practical limitations. Environmental aerosols, that are toxic (such as asbestos fibers) or have the potential to harm the subject (such as carbon nanotubes [Li et al., 2010]) can not be studied *in–vivo* from an ethical point of view. The cumulative deposition approach measures only how different concentrations are between inhaled and exhaled aerosols. And based on this information, conclusions on aerosol mass retainment are made [Emmett et al., 1982; Jaques and Kim, 2000]. Measuring total deposition does not tell the whole story: where in the lungs and in what amounts various aerosols deposit under different breathing patterns remains unknown at a morphological level. Indirect *in–vivo* methods exist to study local deposition patterns of nontoxic aerosols. The most common are the studies based on retention of radio or magnetically labeled aerosols [Redman et al., 2011; Fok et al., 1996], and analysis of aerosol bolus[1] inhalation data [Kim and Hu, 1998; Ma and Darquenne, 2012; Sturm, 2014].

A large body of knowledge about local particle deposition has been generated using *in–vitro* experimental data from studies on airway replicas [Borojeni et al., 2014; Kelly et al., 2004; Oldham and Phalen, 2002; Doorly et al., 2008] and airway idealized models [Oldham et al., 1997; Zhang and Finlay, 2005; Javaheri et al., 2013; Golshahi et al., 2013; Azhdarzadeh et al., 2014]. Such studies are restricted to extrathoracic and bronchial airways only. Acinar geometries, due to their small sizes, are very difficult to construct and experiment with at full size, although, recently there have been attempts towards modelling and simulation of fluid dynamics within alveolar geometries using microfluidic devices [Kumar Mahto et al., 2012].

1.2.2 Mathematical modeling

It is apparent that experimental techniques do not entirely satisfy the demand for scientific data related to aerosol deposition in the lungs. As we mentioned earlier, experimental

[1] [Golshahi and Finlay, 2009] define aerosol bolus as a volume of gas, which contains particles, that is surrounded by particle-free air *i.e.*, aerosol particles are not distributed evenly throughout the entire breath but are instead confined to a small bolus within the inspired air. Analysis is performed on the expired aerosol concentration which has been found to be a good tracer for convective mixing within defined segments of the respiratory system [Heyder et al., 1988].

techniques supply information on total lung deposition studies but are lacking in predicting accurate local depositions through the entire range of airway bifurcations. Certain aerosols can not be tested on living humans, and it is not ethical to perform experiments on children or other vulnerable demographic groups. Moreover, experimental studies in a strict sense are only valid within the domain of the specific test subjects, specific particle sizes and shapes, lung capacities and breathing patterns. While idealized airway models such as Alberta Idealized Throat [Stapleton et al., 2000] avoid the inter-subject variability issue by averaging individual airway geometries, they do not solve the other practical problems mentioned above.

At the same time, with the latest advances in inhalation drug therapy and with continuing concerns about known and emerging aerosols that pose health risks to the human population, there is strong interest and demand for more information about regional deposition sites within lungs for a wide variety of aerosols under different breathing patterns. Potentially, particle deposition modeling can fill the gaps in the knowledge left open by experimental approaches. A combination of scientific disciplines such as mathematics, biology, and continuum mechanics are required for proper construction of respiratory deposition models and calls for serious interdisciplinary studies. Inevitably, mathematical modeling will require idealization of actual morphological or mechanical characteristics of the lung–aerosol system. Good mathematical models will not necessarily perform adequately for all possible cases, but within certain limits, must allow analytical or numerical solution of idealized equations employing physically and biologically realistic assumptions. And usually, the fewer assumptions that are made regarding the fluid mechanics or morphology of the system, the more complicated the mathematical model that has to be built.

There are two types of particle deposition models categorized by the approach for finding deposition within individual airways. When analytical relations are used to predict deposition in each airway, such models are called analytical and they are well capable of predicting deposition efficiencies in the whole respiratory system. Examples of such models are [Asgharian and Yu, 1988; Balásházy et al., 1990; Asgharian et al., 2001; Choi and Kim, 2007; Zhou et al., 2008]. In order to develop analytical expressions for deposition probabilities these models decouple airway fluid dynamics from particle transport. Hence, assuming laminar flow regimes with possible correction factors accounting for turbulence in the trachea and extrathoracic region, corresponding deposition equations are used within a lung morphology simplified to a system of bifurcating tubes. Such simplifications work well at predicting total particle deposition in the respiratory system but they may result in local deposition efficiencies several times greater or smaller than those obtained with

other methods [Zhang et al., 2009b]. The second type of models, which are best suited for predicting local deposition and transport of particles within a single or a few consecutive airway bifurcations, are the so called computer simulation models or computational fluid dynamics (CFD) models. These models are different in that the fluid flow in all its complexity is resolved locally in a single or even in a span of few airway bifurcations. They naturally allow for the most realistic airway geometries to be studied but at the same time, the complexity of the respiratory system restricts their application to a limited number of elementary morphological elements within larger components of the respiratory system. Examples of computational deposition models grouped by the lung region are: for extrathoracic airways [Liu et al., 2007; Xi et al., 2014], for bronchi [Zhang et al., 2009b; Longest and Xi, 2007; Pilou et al., 2013], and for the alveolar region [Tsuda et al., 2008; Balásházy et al., 2008; Henry et al., 2012; Sznitman, 2013]. Once the fluid flow is resolved, particle dynamics equations are solved taking into account particle velocity, local fluid velocity, particle mass, and Brownian diffusion. For example, a typical equation of motion in a Lagrangian description for a spherical particle of diameter d_p and mass m_p can be written as [Sznitman, 2013]:

$$m_p \frac{d\boldsymbol{u}_p}{dt} = \boldsymbol{F}_D + \boldsymbol{F}_g + \boldsymbol{F}_{diff}, \tag{1.1}$$

with $\boldsymbol{F}_g = m_p \boldsymbol{g}$ being the force of gravity, $\boldsymbol{F}_D = -3\pi d_p \mu (\boldsymbol{u}_p - \boldsymbol{v})/C_C$ drag force on the particle surface exerted by a fluid with dynamic viscosity μ and local velocity $\boldsymbol{v}$ corrected using Cunningham slip correction factor C_C [Finlay, 2001], and random force due to Brownian diffusion $\boldsymbol{F}_{diff}$. It is also possible to study particle deposition in an Eulerian description solving for spatial concentration of monodisperse aerosol c $[m^{-3}]$ as in [Pilou et al., 2013]:

$$\frac{\partial c}{\partial t} + \boldsymbol{\nabla}\cdot(c\boldsymbol{u}_p) = 0, \tag{1.2}$$

where particles velocities are given by $\boldsymbol{u}_p = \boldsymbol{v} - \tau_p \boldsymbol{v}\cdot\boldsymbol{\nabla}\boldsymbol{v} - D\boldsymbol{\nabla}\ln c + O(\tau_p^2)$, with particle relaxation time $\tau_p = \rho_p d_p^2 C_C/18\mu$ having the meaning of the characteristic time of the particle velocity decay due to drag, diffusion coefficient D, dynamic viscosity μ and particle density ρ_p. The CFD approach works well for predicting local deposition efficiencies of spherical particles and for identification of localized sites of excessive deposition, which is important when looking for potential locations of lung disease when subjected to toxic aerosols or when targeted drug delivery in the lungs is desired.

Deposition of high aspect ratio particles

The particle deposition equations (1.1) and (1.2) use particle size d_p and density ρ_p (mass m_p) to determine deposition within the respiratory system. The shape of inhaled particles is another important parameter which has significant importance in deposition patterns for nonspherical aerosols. In contrast, equations (1.1) and (1.2) assume spherical particle shape and completely ignore rotational motion of the particles which can significantly alter computed locations of deposition sites. In reality only liquid particles and particles made by evaporation of liquid droplets have spherical shapes, while most other aerosols have a variety of different geometries. When an aerosol is known to be composed of nonspherical particles, then the particle dynamic shape factor χ can be used in equations (1.1) and (1.2) to account for altered behavior of the particles. The dynamic shape factor is defined as the ratio of the actual drag force of the nonspherical particle to the drag force of a sphere having the same volume and velocity as the nonspherical particle, [Hinds, 1999]:

$$\chi = \frac{F_D C_C(d_e)}{3\pi d_e \mu \, |\boldsymbol{u}_p - \boldsymbol{v}|}, \tag{1.3}$$

where d_e is an equivalent volume diameter *i.e.*, the diameter of a spherical particle with the same volume as that of the actual particle. Obviously, it is impossible to know $\boldsymbol{F}_D$ *a priori*, therefore values of χ are tabulated experimentally for selected shapes by averaging over all possible orientations [Davies, 1979; Dahneke, 1982; Johnson et al., 1987; Cheng et al., 1988]. With known χ, equation (1.1) can be applied to nonspherical particles using a corrected resistance force $\boldsymbol{F}_D = -3\pi d_e \mu(\boldsymbol{u}_p - \boldsymbol{v})\chi / C_C(d_e)$; similarly, correcting the particle relaxation time $\tau_p = \rho_p d_e^2 C_C(d_e)/18\mu\chi$, equation (1.2) can be extended to study the deposition of more general classes of nonspherical aerosols.

When dynamic shape factor is used, the actual particle is replaced with an equivalent volume sphere which feels the same resistance, averaged over all orientations, to linear motion as the actual particle, but resistance to rotation or torque on the particle surface is still ignored. Therefore, it is not reasonable to expect that the fluid dynamics of an arbitrary particle with complex geometry can be well approximated by a sphere with the same volume. Indeed, experiments with high aspect ratio straight particles [Anczurowski and Mason, 1967] and ellipsoids [Anczurowski and Mason, 1968] and theoretical results for prolate spheroids [Jeffery, 1922; Asgharian and Anjilvel, 1995] predict alignment of high aspect ratio particles parallel to streamlines and following them around bending and bifurcating airways in the lungs. This suggests that, contrary to the concept of equivalent volume diameter, particle length has insignificant effect on the equivalent aerodynamic

diameter[2] for most of the time. Thus, while aligned with the flow, high aspect ratio particles behave nearly identically to the spherical particles with diameters equal to the fibers diameters, and do not get intercepted as readily by airway walls as would be in the case of random orientation in the airway as assumed for the dynamic shape factor.

At the same time, fibrous aerosols, even those composed of fibers with simple geometries (which are usually man made), produce particle agglomerates when individual particles stick together or when they are contaminated with dust [Hwang, 1983]. Besides, real fibrous aerosols are far from being characterized as being symmetric or regular in shape, as is seen in Figure 1.2 and Figure 1.3.

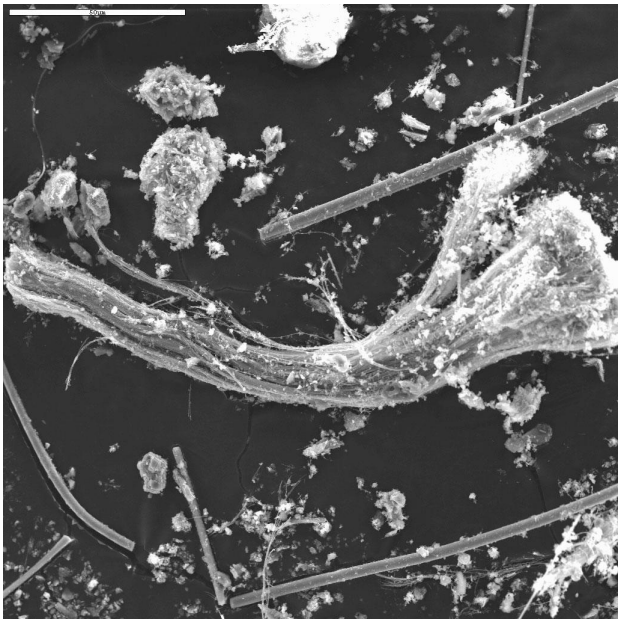

Figure 1.2: Chrysotile bundle, World Trade Center dust. Bar length corresponds to 50 μm. *Courtesy of the U.S. Geological Survey.*

Aerodynamics of high aspect ratio fibers of complex shapes can tremendously impact their deposition in the respiratory system, but simple analytical or existing CFD models are only partially able to account for this. Therefore, efficient mathematical and computational tools are required in order to address the dynamics of fibers of complex shape in the three dimensional flows such as are observed in the airways. Such tools should be able to resolve particle motion in all its complexity, accounting for the realistic fluid dynamics of the surrounding air in all airway bifurcations starting from the trachea.

[2]Diameter of a spherical particle with a density of 1000 kg/m^3 that has the same settling velocity as the actual particle.

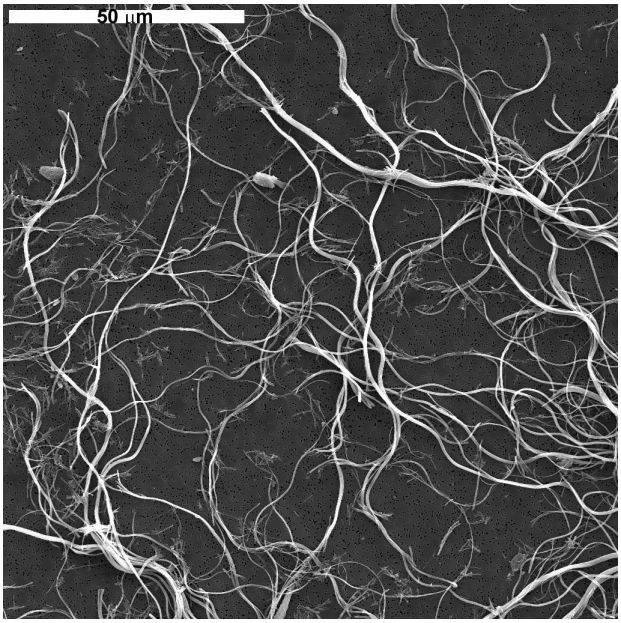

Figure 1.3: Union Internationale Contre le Cancer (UICC) Asbestos Chrysotile 'A' standard, *courtesy of the U.S. Geological Survey.*

Previously, very little has been done in this direction. To our knowledge, there have been only two attempts to study lung deposition of curved fibers. In one of them, performed by [Asgharian and Ahmadi, 1998], a bent fiber was made by attaching two ellipsoids at an angle to each other. Based on analytical results for drag force and torque for ellipsoids, the corresponding equations of motion were obtained for the link of ellipsoids. In another attempt, [Podgórski and Gradon, 1990] studied motion of deformable elongated fibrous particles in a pipe representing an airway between two bifurcations in a stationary fully laminar parabolic profile. Their equations of motion were based on expressions for body forces derived by [Cox, 1970] under the assumptions of circular particle cross–section with constant radius along the axis of symmetry and vanishing Reynolds number.

1.3 Fluid–Structure interaction

One important aspect that was significantly simplified in the described models in the previous section was the motion of airways during a normal breathing cycle. With recent developments in medical imaging technologies which provide an understanding of real airway geometries and their variability among subjects, modeling the respiratory system as a network of smooth bifurcating cylinders with dominant laminar airflow proves to be in-

adequate in explaining realistic particle deposition mechanisms as well as experimentally observed flow structures [Wall and Rabczuk, 2008]. In a more realistic model, local features of the airflow and its global characteristics within the lungs are determined by a combination of hydrodynamic resistance to flow in the narrow tubes and the compliance of the airway walls in such a way that tissue compliance plays a more important role in the global distribution of air within the respiratory system [Tawhai and Lin, 2011]. As more and more computational resources become available, CFD takes a leading role in providing insight into realistic mechanics of airflow interacting with lung tissues.

Particularly, in connection with ventilator-induced lung injuries, [Wall et al., 2010] point out that CFD studies on fixed airways can not provide information on the stresses occurring within lung tissues under mechanical ventilation. High shear stresses in airway walls caused by wrong ventilation frequencies and alveolar overexpansions can be predicted and corrected when fluid–structure interaction (FSI) algorithms are used in conjunction with patient–specific computer tomography (CT) models of the lungs. Additionally, [Wall et al., 2010] report that even though normalized flow distributions and secondary flow intensities are not very different when FSI simulations are applied to realistic upper bronchial geometries, major and secondary airflow patterns were different and in spite of a relatively small changes (of about 2%) in airway crossection areas. Such differences in airflow patterns may be less important for larger aerosols, but it may cause significant redistribution of deposition sites for sub–micron and nanoparticles which have a more pronounced tendency to follow the air flow.

Another example of the importance of the correct resolution of the coupled dynamics of air and airway walls is the flow mixing and particle deposition in the pulmonary acini. Historically, due to small dimensions and corresponding small Reynolds numbers, flows in the distal airways were considered kinematically reversible. Therefore, small particles reaching that far into the bronchial tree must have been following streamlines and as such exhaled the same way as they got there, with the only source of perturbation due to Brownian diffusion [Edwards, 1994; Darquenne and Paiva, 1994]. Instead, it was observed experimentally that acinar flow in complex alveolar geometries with time dependent wall motion is characterized by recirculating flow structures [Tsuda et al., 2002]. It was shown numerically [Tsuda et al., 1995; Henry et al., 2002] that such recirculatory flows may cause the formation of stagnation points within the fluid domain and can be associated with irreversible chaotic transport of massless particles.

Many studies since the year 2000 have covered the role of alveolar rhythmic expansion, different breathing regimes, the importance of ductal and alveolar flow rates and alveolar

topology in the particle deposition modeling in the distal airways. A summary of the major results has been recently reviewed by [Sznitman, 2013]. These advances were associated with increased availability of commercial CFD software and the assumption of geometrical self–similar expansion of the studied alveolar geometries, the latter supported by many sources, among them [Weibel, 1986; Gil et al., 1979]. At the same time, [Miki et al., 1993] reported that lung expansion undergoes geometric hysteresis, which can alter flow and particle deposition in the acini.

The dynamical interaction between a Newtonian fluid and a hyper-elastic solid governs many processes within human body. In recent years advances in development of FSI methods were tightly connected with numerical studies of various biological flows, not only within the respiratory system. Particularly, these techniques found their use in the study of cardiac valves [Dasi et al., 2009; Weinberg et al., 2010], evolution of arterial and cerebral aneurysms [Humphrey and Taylor, 2008; Sforza et al., 2009], pulse–wave propagation [van de Vosse and Stergiopulos, 2011], flow induced oscillations [Heil and Hazel, 2011] to name but a few.

Therefore, now with even more advanced computing technologies available, there is demand for new FSI numerical approaches providing facilities for studying internal biological flows within domains with elastic boundaries.

1.4 Summary of thesis

This thesis presents the development of modern numerical techniques for solving problems involving fluid-solid and fluid-elastic body interactions found in abundance in biological systems. Although the described methods do not carry any assumptions restricting their use elsewhere, they are developed keeping in mind their application to modeling deposition of high aspect ratio fibers of complex shapes subjected to realistic biological flows within the respiratory system.

In Chapter 2, development and evolution of the Fictitious Domain Method for Particulate Flows is outlined as it is used to solve problems addressed in the present thesis.

In Chapter 3, a computational technique for simulating the dynamics of micro-fibers of arbitrary shapes in a general flow structure is presented. This technique is characterized by the use of a micro-grid rigidly attached to the fiber in its spatial motion and by the application of Arbitrary Eulerian-Lagrangian and Fictitious Domain methods for efficient resolution of fluid flow around the particle. Then, two numerical studies based on this technique are presented. The first study characterizes rotational behavior of high aspect

ratio fibers in a linear shear flow, a local approximation to the ductal flow in the lungs. The second one is the study of enhanced deposition of magnetically aligned high aspect ratio fibers in a realistic airway bifurcation.

Chapter 4 presents development of the finite element scheme for simulations of dynamical interaction between a hyper-elastic solids and a Newtonian fluid. The numerical approach is based on the Fictitious Domain Method, where the fluid domain is extended into the entire computational domain and the effect of solid stress is imposed through a body force acting on the fluid in the solid volume. Validation tests are presented and proof of concept simulations in a 3-D alveolated duct are performed.

Chapter 5 discusses results of previous chapters and points out directions for future research.

Chapter 2

Overview of the Fictitious Domain Method (FDM)

2.1 Introduction

In the following we present a development of the Fictitious Domain Method (FDM) for particulate flows from its first complete description in [Glowinski et al., 1999] to its present form that we use in subsequent chapters. In the FDM framework, calculations are performed on a fixed domain with rigid particles moving inside the domain. Time discretization, based on the operator splitting, is employed, allowing for separate treatment of the numerical operators in the computational model.

First, we describe the FDM formulation with Distributed Lagrange Multiplier (DLM) proposed by [Glowinski et al., 1994, 1999]. In this formulation, the Lagrange multiplier acts as an additional body force per unit volume required to assert the rigid–body motion in the solid and it is similar to the pressure in the Navier–Stokes equations, which can be interpreted as a Lagrange multiplier imposing the incompressibility constraint [Glowinski et al., 1999].

Then, the formulation by [Diaz-Goano et al., 2003] follows, where instead of the DLM, a global Lagrange multiplier is introduced, allowing simpler handling of large solid fractions suspended in the fluid.

Afterward, we describe the [Veeramani et al., 2007] approach, which eliminates the global Lagrange multiplier from the set of governing equations and allows us to explicitly resolve the interaction force between the fluid and the solid.

Finally, we briefly mention a moving grid procedure for very small particles proposed

in [Dechaume et al., 2010] which is based on the [Veeramani et al., 2007] formulation of the FDM.

2.2 Governing Equations

Consider the flow of an incompressible fluid with density ρ_f and dynamic viscosity $\mu = \rho_f \nu$ around a moving solid particle with density ρ_p and volume V_p. The fluid flow is governed by the Navier–Stokes equations

$$\rho_f \frac{D\boldsymbol{v}}{Dt} = \boldsymbol{\nabla}\cdot\sigma, \qquad \boldsymbol{\nabla}\cdot\boldsymbol{v} = 0 \qquad \text{in } \Omega_f, \tag{2.1}$$

with volume occupied by the fluid denoted Ω_f, fluid velocity field $\boldsymbol{v}$, full material derivative

$$\frac{D\boldsymbol{v}}{Dt} = \frac{\partial \boldsymbol{v}}{\partial t} + \boldsymbol{v}\cdot\boldsymbol{\nabla}\boldsymbol{v},$$

and fluid stress tensor $\boldsymbol{\sigma}$ defined through the fluid pressure p and velocity rate of strain $\mathbb{D}[\boldsymbol{v}]$ as

$$\boldsymbol{\sigma} = -p\mathbb{I} + 2\mu\mathbb{D}[\boldsymbol{v}], \tag{2.2}$$

such that $\mathbb{D}[\cdot] = \frac{1}{2}[\boldsymbol{\nabla}(\cdot) + \boldsymbol{\nabla}^T(\cdot)]$. The gravitational term $\rho_f \boldsymbol{g}$, where $\boldsymbol{g}$ is the vector of gravitational acceleration, in equation (2.1) has been combined into the pressure p for convenience of notation. Additionally, a no–slip boundary condition $\boldsymbol{v} = \boldsymbol{U} + \boldsymbol{\omega}\times\boldsymbol{r}$ on the particle surface $\partial\Omega_p$ is imposed, such that $\boldsymbol{r} = (\boldsymbol{x} - \boldsymbol{X})$, where $\boldsymbol{x}$ is a point on the particle boundary; $\boldsymbol{U}$, $\boldsymbol{\omega}$, and $\boldsymbol{X}$ are respectively the particle centroid velocity, angular velocity, and center of mass position. Schematics of the fluid domain with immersed solid are illustrated in Figure 2.1.

The particle motion is governed by the following equations:

$$\begin{aligned} \rho_p V_p \frac{d\boldsymbol{U}}{dt} &= V_p(\rho_p - \rho_f)\boldsymbol{g} + \boldsymbol{F} \\ \frac{d(\mathbb{I}_p\boldsymbol{\omega})}{dt} &= \boldsymbol{T}, \qquad \frac{d\boldsymbol{\vartheta}}{dt} = \boldsymbol{\omega}, \qquad \frac{d\boldsymbol{X}}{dt} = \boldsymbol{U} \end{aligned} \tag{2.3}$$

where $\mathbb{I}_p$ is the solid inertia tensor and $\boldsymbol{\vartheta}$ is the rotation vector (vector pointing along the rotation axis with modulus equal to the rotation angle). Here, $\boldsymbol{F}$ is the total hydrodynamic force, and $\boldsymbol{T}$ is the torque about the center of mass acting on the particle surface; they can

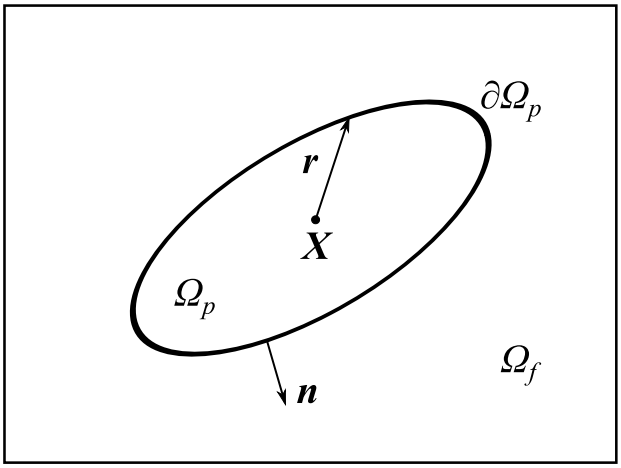

Figure 2.1: Typical computational domain for problems solved with the Fictitious Domain Method. Illustrated: fluid domain Ω_f, particle domain Ω_p and particle boundary $\partial\Omega_p$.

be expressed as

$$\boldsymbol{F} = \int_{\partial\Omega_p} \boldsymbol{\sigma}\cdot\boldsymbol{n} dS \tag{2.4}$$

and

$$\boldsymbol{T} = \int_{\partial\Omega_p} \boldsymbol{r}\times(\boldsymbol{\sigma}\cdot\boldsymbol{n}) dS. \tag{2.5}$$

where $\boldsymbol{n}$ is the outward normal to $\partial\Omega_p$.

2.3 Distributed Lagrange Multiplier

2.3.1 Weak formulation for the combined fluid–solid system

Following the argument of [Glowinski et al., 1994, 1999] we can derive a weak formulation of the governing equations for the combined fluid–solid system (2.1)–(2.3) such that the hydrodynamic torques and surface forces appearing in the equations (2.3) are eliminated.

The combined formulation is made possible by defining the combined trial velocity

space, which restricts functions on $\partial\Omega_p$ to satisfy a rigid body motion constraint:

$$\begin{aligned}\hat{\boldsymbol{V}}_{\boldsymbol{v}} = \{(\boldsymbol{v}, \boldsymbol{U}, \boldsymbol{\omega}) |\ & \boldsymbol{v} \in \boldsymbol{H}^1(\Omega_f),\ \boldsymbol{U} \in \mathbb{R}^3,\ \boldsymbol{\omega} \in \mathbb{R}^3, \\ & \boldsymbol{v} = \boldsymbol{U} + \boldsymbol{\omega} \times \boldsymbol{r} \text{ on } \partial\Omega_p, \text{ and } \boldsymbol{v} = \boldsymbol{v}_{\partial\Omega}(t) \text{ on } \partial\Omega\}\end{aligned} \tag{2.6}$$

with the corresponding test space

$$\begin{aligned}\hat{\boldsymbol{V}} = \{(\hat{\boldsymbol{\varphi}}, \hat{\boldsymbol{\psi}}, \hat{\boldsymbol{\varpi}}) |\ & \hat{\boldsymbol{\varphi}} \in \boldsymbol{H}^1(\Omega_f),\ \hat{\boldsymbol{\psi}} \in \mathbb{R}^3,\ \hat{\boldsymbol{\varpi}} \in \mathbb{R}^3, \\ & \hat{\boldsymbol{\varphi}} = \hat{\boldsymbol{\psi}} + \hat{\boldsymbol{\varpi}} \times \boldsymbol{r} \text{ on } \partial\Omega_p, \text{ and } \hat{\boldsymbol{\varphi}} = 0 \text{ on } \partial\Omega\},\end{aligned} \tag{2.7}$$

where $\partial\Omega$ is the outside boundary of the computational domain $\partial\Omega = \partial\Omega_f \setminus \partial\Omega_p$.

Using the fluid momentum equation (2.1) with the test functions (2.7) and integrating the right hand side by parts we obtain:

$$\int_{\Omega_f} \rho_f \frac{D\boldsymbol{v}}{Dt} \cdot \hat{\boldsymbol{\varphi}}\ d\Omega = \int_{\partial\Omega_p} \boldsymbol{\sigma} \cdot \hat{\boldsymbol{\varphi}} \cdot \boldsymbol{n}\ \partial S - \int_{\Omega_f} \boldsymbol{\sigma} : \mathbb{D}[\hat{\boldsymbol{\varphi}}]\ d\Omega, \tag{2.8}$$

where $\boldsymbol{n}$ is the normal pointing inside Ω_p.

Similarly, multiplying (2.3) with the corresponding test functions, we find:

$$\begin{aligned}\rho_p V_p \left(\frac{d\boldsymbol{U}}{dt} - \frac{\rho_r - 1}{\rho_r} \boldsymbol{g} \right) \cdot \hat{\boldsymbol{\psi}} &= \int_{\partial\Omega_p} \boldsymbol{\sigma} \cdot \boldsymbol{n} \cdot \hat{\boldsymbol{\psi}}\ \partial S \\ \frac{d(\mathbb{I}_p \boldsymbol{\omega})}{dt} \cdot \hat{\boldsymbol{\varpi}} &= \int_{\partial\Omega_p} (\boldsymbol{r} \times (\boldsymbol{\sigma} \cdot \boldsymbol{n})) \cdot \hat{\boldsymbol{\varpi}}\ \partial S,\end{aligned} \tag{2.9}$$

where $\rho_r = \frac{\rho_p}{\rho_f}$ is the relative density of the particle in the fluid. From the definition of the test functions, the following relation $\hat{\boldsymbol{\varphi}} = \hat{\boldsymbol{\psi}} + \hat{\boldsymbol{\varpi}} \times \boldsymbol{r}$ is satisfied on $\partial\Omega_p$; therefore, the surface integral on the right hand side of (2.8) becomes:

$$\int_{\partial\Omega_p} \boldsymbol{\sigma} \cdot \hat{\boldsymbol{\varphi}} \cdot \boldsymbol{n}\ \partial S = \int_{\partial\Omega_p} \boldsymbol{\sigma} \cdot \hat{\boldsymbol{\psi}} \cdot \boldsymbol{n}\ \partial S + \int_{\partial\Omega_p} \boldsymbol{\sigma} \cdot (\hat{\boldsymbol{\varpi}} \times \boldsymbol{r}) \cdot \boldsymbol{n}\ \partial S, \tag{2.10}$$

which can be rewritten using $\boldsymbol{a} \cdot (\boldsymbol{b} \times \boldsymbol{c}) = \boldsymbol{b} \cdot (\boldsymbol{c} \times \boldsymbol{a})$ as

$$\int_{\partial\Omega_p} \boldsymbol{\sigma} \cdot \hat{\boldsymbol{\varphi}} \cdot \boldsymbol{n}\ \partial S = \int_{\partial\Omega_p} \boldsymbol{\sigma} \cdot \hat{\boldsymbol{\psi}} \cdot \boldsymbol{n}\ \partial S + \int_{\partial\Omega_p} \hat{\boldsymbol{\varpi}} \cdot (\boldsymbol{r} \times (\boldsymbol{\sigma} \cdot \boldsymbol{n}))\ \partial S. \tag{2.11}$$

Inserting equation (2.11) into equation (2.8) and adding to it equations (2.9) we find that the surface integrals on the right hand side cancel and the resulting combined equation of motion reads:

$$\int_{\Omega_f} \rho_f \frac{D\boldsymbol{v}}{Dt}\cdot\hat{\boldsymbol{\varphi}}\; d\Omega + \rho_p V_p \left(\frac{d\boldsymbol{U}}{dt} - \frac{\rho_r - 1}{\rho_r}\boldsymbol{g}\right)\cdot\hat{\boldsymbol{\psi}} + \frac{d(\mathbb{I}_p\boldsymbol{\omega})}{dt}\cdot\hat{\boldsymbol{\varpi}} = -\int_{\Omega_f} \boldsymbol{\sigma} : \mathbb{D}[\hat{\boldsymbol{\varphi}}]\; d\Omega. \qquad (2.12)$$

With an additional requirement that the pressure

$$p \in \boldsymbol{L}^2_0(\Omega_f) = \left\{ q \in \boldsymbol{L}^2(\Omega_f) \Big| \int_{\Omega_f} q\; d\Omega = 0 \right\},$$

we state the weak form of the incompressibility constraint:

$$\int_{\Omega_f} q\boldsymbol{\nabla}\cdot\boldsymbol{v}\; d\Omega = 0 \text{ for all } q \in \boldsymbol{L}^2(\Omega_f). \qquad (2.13)$$

2.3.2 A Fictitious Domain Formulation

In order to obtain a fictitious domain formulation, we seek to extend the fluid problem from Ω_f to the entire $\Omega = \Omega_f \cup \Omega_p$, while continuing to satisfy the no–slip boundary condition on the solid surface $\partial\Omega_p$. Such an approach improves the computational performance of the method by allowing solution of the problem on a fixed grid covering the entire domain Ω. Following [Glowinski et al., 1999], extension of the formulation (2.12) onto Ω is performed in two steps:

1. Obtain a combined weak formulation in Ω_p and add it to (2.12), producing a new weak formulation which covers the whole Ω.

2. Enforce rigid–body motion as a side constraint through a Lagrange multiplier defined in Ω_p, effectively removing the rigid–body motion constraint from the combined equation.

In order to produce the combined equation of motion over the Ω_p domain, we have to extend the rigid–body constraint for the velocity $\boldsymbol{v}$ and the corresponding velocity test functions $\hat{\boldsymbol{\varphi}}$ from the particle boundary $\partial\Omega_p$ into Ω_p. Then, the appropriate functional

spaces can be defined as:

$$\begin{aligned}\boldsymbol{V_v} = \{(\boldsymbol{v},\boldsymbol{U},\boldsymbol{\omega})|\ \boldsymbol{v}\in\boldsymbol{H}^1(\Omega),\ \boldsymbol{U}\in\mathbb{R}^3,\ \boldsymbol{\omega}\in\mathbb{R}^3,\\ \boldsymbol{v}=\boldsymbol{U}+\boldsymbol{\omega}\times\boldsymbol{r}\text{ in }\Omega_p,\text{ and }\boldsymbol{v}=\boldsymbol{v}_{\partial\Omega}(t)\text{ on }\partial\Omega\}\end{aligned} \tag{2.14}$$

and the test space

$$\begin{aligned}\boldsymbol{V} = \{(\boldsymbol{\varphi},\boldsymbol{\psi},\boldsymbol{\varpi})|\ \boldsymbol{\varphi}\in\boldsymbol{H}^1(\Omega),\ \boldsymbol{\psi}\in\mathbb{R}^3,\ \boldsymbol{\varpi}\in\mathbb{R}^3,\\ \boldsymbol{\varphi}=\boldsymbol{\psi}+\boldsymbol{\varpi}\times\boldsymbol{r}\text{ in }\Omega_p,\text{ and }\boldsymbol{\varphi}=0\text{ on }\partial\Omega\},\end{aligned} \tag{2.15}$$

where $\partial\Omega$ is set as before: $\partial\Omega = \partial\Omega_f \setminus \partial\Omega_p$.

Using (2.14) and (2.15) we find that in Ω_p

$$\frac{D\boldsymbol{v}}{Dt} = \frac{d\boldsymbol{U}}{dt} + \frac{d\boldsymbol{\omega}}{dt}\times\boldsymbol{r} + \boldsymbol{\omega}\times\frac{d\boldsymbol{r}}{dt}, \tag{2.16}$$

which, remembering $\boldsymbol{r} = \boldsymbol{x} - \boldsymbol{X}$ and $d\boldsymbol{r}/dt = \boldsymbol{v} - \boldsymbol{U}$, results in

$$\frac{D\boldsymbol{v}}{Dt} = \frac{d\boldsymbol{U}}{dt} + \frac{d\boldsymbol{\omega}}{dt}\times\boldsymbol{r} + \boldsymbol{\omega}\times(\boldsymbol{\omega}\times\boldsymbol{r}) \quad \text{ in } \Omega_p. \tag{2.17}$$

Testing (2.17) with $\rho_p\boldsymbol{\varphi}$ within solid domain yields:

$$\int\limits_{\Omega_p}\rho_p\frac{D\boldsymbol{v}}{Dt}\cdot\boldsymbol{\varphi}\ d\Omega = \int\limits_{\Omega_p}\rho_p\left(\frac{d\boldsymbol{U}}{dt} + \frac{d\boldsymbol{\omega}}{dt}\times\boldsymbol{r} + \boldsymbol{\omega}\times(\boldsymbol{\omega}\times\boldsymbol{r})\right)\boldsymbol{\varphi}\ d\Omega;$$

and applying the rigid–body constraint from (2.15), we obtain:

$$\int\limits_{\Omega_p}\rho_p\frac{D\boldsymbol{v}}{Dt}\cdot\boldsymbol{\varphi}\ d\Omega = \rho_p V_p\frac{d\boldsymbol{U}}{dt}\cdot\boldsymbol{\psi} + \frac{d(\mathbb{I}_p\boldsymbol{\omega})}{dt}\cdot\boldsymbol{\varpi}. \tag{2.18}$$

In order to derive the last equation, we have used

$$\int\limits_{\Omega_p}\boldsymbol{r}\ d\Omega = 0,$$

and

$$\rho_p\int\limits_{\Omega_p}\boldsymbol{r}\times\left(\frac{d\boldsymbol{\omega}}{dt}\times\boldsymbol{r}\right)\ d\Omega\cdot\boldsymbol{\varpi} = \mathbb{I}_p\frac{d\boldsymbol{\omega}}{dt}\cdot\boldsymbol{\varpi},$$

plus the Jacobi identity for the triple cross product:

$$\rho_p \int_{\Omega_p} (\boldsymbol{r}\times(\boldsymbol{\omega}\times(\boldsymbol{\omega}\times\boldsymbol{r}))) \; d\Omega\cdot\boldsymbol{\varpi} = \boldsymbol{\omega}\times(\mathbb{I}_p\boldsymbol{\omega})\cdot\boldsymbol{\varpi}.$$

Multiplying (2.18) with ρ_f/ρ_p and adding it to (2.12), and taking into account that the rigid–body constraint implies $\mathbb{D}[\boldsymbol{\varphi}] = 0$ and

$$-\int_{\Omega_p} \boldsymbol{\sigma} : \mathbb{D}[\boldsymbol{\varphi}] \; d\Omega = 0,$$

the combined weak formulation on the entire domain Ω becomes:

$$\int_{\Omega} \rho_f \frac{D\boldsymbol{v}}{Dt}\cdot\boldsymbol{\varphi} \; d\Omega + \frac{\rho_r - 1}{\rho_r}\left[\rho_p V_p \left(\frac{d\boldsymbol{U}}{dt} - \boldsymbol{g}\right)\cdot\boldsymbol{\psi} + \frac{d(\mathbb{I}_p\boldsymbol{\omega})}{dt}\cdot\boldsymbol{\varpi}\right] = -\int_{\Omega} \boldsymbol{\sigma} : \mathbb{D}[\boldsymbol{\varphi}] \; d\Omega. \quad (2.19)$$

The definition of the combined velocity space strongly enforces the rigid-body constraint in Ω_p for both the resulting velocity $\boldsymbol{v}$ and the corresponding test function $\boldsymbol{\varphi}$. [Glowinski et al., 1999] propose to relax the rigid body constraint by removing it from the combined velocity space (2.14) and instead enforce it in a weak sense as a side constraint through an appropriate DLM.

Finally, the weak formulation with the solid motion constraint relaxed using the DLM reads:

Find $\boldsymbol{v} \in \boldsymbol{W} = \{\boldsymbol{\varphi} \in \boldsymbol{H}^1(\Omega)|\ \boldsymbol{\varphi} = \boldsymbol{v}_{\partial\Omega} \text{ on } \partial\Omega\}$, $p \in L^2_0(\Omega)$, $\boldsymbol{\lambda} \in \boldsymbol{\Lambda}(t) = H^1(\Omega_p)$, $\boldsymbol{U} \in \mathbb{R}^3$, $\boldsymbol{\omega} \in \mathbb{R}^3$ satisfying:

$$\begin{aligned}\int_{\Omega} \rho_f \frac{D\boldsymbol{v}}{Dt}\cdot\boldsymbol{\varphi} \; d\Omega + \int_{\Omega} \boldsymbol{\sigma} : \mathbb{D}[\boldsymbol{\varphi}] \; d\Omega + \frac{\rho_r - 1}{\rho_r}\left[\rho_p V_p \left(\frac{d\boldsymbol{U}}{dt} - \boldsymbol{g}\right)\cdot\boldsymbol{\psi} + \frac{d(\mathbb{I}_p\boldsymbol{\omega})}{dt}\cdot\boldsymbol{\varpi}\right] = \\ = \langle\boldsymbol{\lambda},\ \boldsymbol{\varphi} - (\boldsymbol{\psi} + \boldsymbol{\varpi}\times\boldsymbol{r})\rangle_{\Omega_p(t)}\end{aligned} \quad (2.20)$$

for all $\boldsymbol{\varphi} \in \boldsymbol{W}_0$, $\boldsymbol{\psi} \in \mathbb{R}^3$ and $\boldsymbol{\varpi} \in \mathbb{R}^3$, coupled with

$$\int_{\Omega} q\boldsymbol{\nabla}\cdot\boldsymbol{v} \; d\Omega = 0 \text{ for all } q \in L^2(\Omega), \quad (2.21)$$

and

$$\langle\boldsymbol{\eta},\ \boldsymbol{v} - (\boldsymbol{U} + \boldsymbol{\omega}\times\boldsymbol{r})\rangle_{\Omega_p(t)} = 0 \text{ for all } \boldsymbol{\eta} \in \Lambda(t), \quad (2.22)$$

with an appropriate inner product $\langle \cdot, \cdot \rangle_{\Omega_p(t)}$ in $\Lambda(t)$. For example, [Glowinski et al., 1999] use the standard $H^1(\Omega_p)$ inner product

$$\langle \boldsymbol{\eta},\ \boldsymbol{\varphi} \rangle_{\Omega_p(t)} = \int\limits_{\Omega_p(t)} (\boldsymbol{\eta} \cdot \boldsymbol{\varphi} + \boldsymbol{\nabla}\boldsymbol{\eta} : \boldsymbol{\nabla}\boldsymbol{\varphi})\ d\Omega.$$

2.4 Global Lagrange Multiplier

The Fictitious Domain Method (FDM) with the Distributed Lagrange Multiplier (DLM), described in the previous section, is found to be robust and useful for simulations involving one or a few solid particles. Unfortunately, application of FDM with DLM to fluidized beds was complicated by the requirement to impose the rigid–body constraint separately for each solid domain.

The method proposed in [Diaz-Goano et al., 2003] develops on the [Glowinski et al., 1999] approach, but instead of using for each particle its own Lagrange multiplier, they use a global Lagrange multiplier defined in the whole computational domain $\Omega = \Omega_f \cup \Omega_p$.

In order to derive the new formulation, [Diaz-Goano et al., 2003] propose to define a new velocity field $\boldsymbol{u}(\boldsymbol{x}, t) \in L^2(\Omega)$ such that

$$\boldsymbol{u}(\boldsymbol{x}, t) = \boldsymbol{U}(t) + \boldsymbol{\omega}(t) \times (\boldsymbol{x} - \boldsymbol{X}) \quad \text{in } \Omega_p, \tag{2.23}$$

and $\boldsymbol{u}(\boldsymbol{x}, t) = 0$ in Ω_f.

The momentum equation for $\boldsymbol{u}$ in Ω_p can be derived from (2.3) taking into account (2.4) and remembering that $\int\limits_{\Omega_p} \boldsymbol{\omega} \times \boldsymbol{r}\ d\Omega = 0$:

$$\begin{aligned} \rho_p V_p \frac{d\boldsymbol{U}}{dt} = \frac{d}{dt} \int\limits_{\Omega_p} \rho_p \boldsymbol{U}\ d\Omega = \frac{d}{dt} \int\limits_{\Omega_p} \rho_p (\boldsymbol{U} + \boldsymbol{\omega} \times \boldsymbol{r})\ d\Omega = \\ = \frac{d}{dt} \int\limits_{\Omega_p} \rho_p \boldsymbol{u}\ d\Omega = \int\limits_{\Omega_p} (\rho_p - \rho_f) \boldsymbol{g}\ d\Omega + \int\limits_{\partial\Omega_p} \boldsymbol{\sigma} \cdot \boldsymbol{n}\ \partial S \end{aligned} \tag{2.24}$$

At this point, the stress tensor $\boldsymbol{\sigma}$ used in (2.24) is the fluid viscous stress defined over Ω_f. [Diaz-Goano et al., 2003] propose to extend this stress continuously inside Ω_p by extending the velocity field $\boldsymbol{v}$ and the pressure field p inside the solid. Note, that at this point $\boldsymbol{v}$ is not necessarily equal to $\boldsymbol{u}$ in Ω_p. Therefore, applying the divergence theorem to the surface

integral in (2.24) we find:

$$\int\limits_{\Omega_p} \frac{D}{Dt}(\rho_p \boldsymbol{u})\ d\Omega = \int\limits_{\Omega_p} (\rho_p - \rho_f)\boldsymbol{g}\ d\Omega + \int\limits_{\Omega_p} \boldsymbol{\nabla}\cdot\boldsymbol{\sigma}\ d\Omega, \tag{2.25}$$

which, using (2.2), becomes:

$$\int\limits_{\Omega_p} \frac{D}{Dt}(\rho_p \boldsymbol{u})\ d\Omega = \int\limits_{\Omega_p} (\rho_p - \rho_f)\boldsymbol{g}\ d\Omega + \int\limits_{\Omega_p} (-\boldsymbol{\nabla} p + \mu\boldsymbol{\nabla}^2\boldsymbol{v})\ d\Omega. \tag{2.26}$$

Introducing the following interaction force:

$$\boldsymbol{\mathcal{F}} = \begin{cases} -\rho_f \dfrac{D\boldsymbol{v}}{Dt} + \mu\boldsymbol{\nabla}^2\boldsymbol{v} - \boldsymbol{\nabla} p & \text{in } \Omega_p \\ 0 & \text{in } \Omega_f, \end{cases} \tag{2.27}$$

which is related to the total hydrodynamic force on the particle surface (2.4) through the relation

$$\boldsymbol{F} = \int\limits_{\Omega_p} (\boldsymbol{\mathcal{F}} + \rho_f \frac{D\boldsymbol{v}}{Dt})\ d\Omega,$$

the particle momentum equation takes form

$$\int\limits_{\Omega_p} \frac{D}{Dt}(\rho_p \boldsymbol{u} - \rho_f \boldsymbol{v})\ d\Omega = \int\limits_{\Omega_p} [(\rho_p - \rho_f)\boldsymbol{g} + \boldsymbol{\mathcal{F}}]\ d\Omega. \tag{2.28}$$

Using (2.27) we can now write an extended fluid momentum equation which holds in the entire domain Ω:

$$\rho_f \frac{D\boldsymbol{v}}{Dt} = -\boldsymbol{\nabla} p + \mu\boldsymbol{\nabla}^2\boldsymbol{v} - \boldsymbol{\mathcal{F}}, \qquad \boldsymbol{\nabla}\cdot\boldsymbol{v} = 0 \quad \text{in } \Omega. \tag{2.29}$$

Force per unit volume $\boldsymbol{\mathcal{F}}$ has the meaning of the global interaction force between the fluid and the solid and at the same time it enforces the rigid–body motion within the solid phase.

Additionally constraining the global velocity field $\boldsymbol{v}$ with

$$\boldsymbol{v} = \boldsymbol{u} \quad \text{in } \Omega_p, \tag{2.30}$$

which naturally follows from the no–slip boundary condition on the particle surface, the

momentum equation for the solid phase becomes

$$\int_{\Omega_p} \frac{D}{Dt}(\rho_p - \rho_f)\boldsymbol{u}\, d\Omega = \int_{\Omega_p} [(\rho_p - \rho_f)\boldsymbol{g} + \boldsymbol{\mathcal{F}}]\, d\Omega.$$

Adopting the notation $(\rho_p - \rho_f)V_p = \Delta M$ to denote the buoyant mass of the particle, and using (2.23), we find the equation for the particle centroid velocity:

$$\Delta M \frac{d\boldsymbol{U}}{dt} = \Delta M \boldsymbol{g} + \int_{\Omega_p} \boldsymbol{\mathcal{F}}\, d\Omega. \tag{2.31}$$

The angular velocity $\boldsymbol{\omega}$ is expressed from the same no–slip boundary condition on the particle surface, which implies:

$$\int_{\partial\Omega_p} (\boldsymbol{\omega}\times\boldsymbol{r})\times\boldsymbol{n}\, \partial S = \int_{\partial\Omega_p} (\boldsymbol{v} - \boldsymbol{U})\times\boldsymbol{n}\, \partial S,$$

and after applying Stokes' theorem turns into an expression for $\boldsymbol{\omega}$:

$$\boldsymbol{\omega} = \frac{1}{2V_p}\int_{\Omega_p} \boldsymbol{\nabla}\times(\boldsymbol{v} - \boldsymbol{U})\, d\Omega = \frac{1}{2V_p}\int_{\Omega_p} \boldsymbol{\nabla}\times\boldsymbol{v}\, d\Omega. \tag{2.32}$$

Collecting everything together, the following strong form of the Fictitious Domain Method can be stated:

$$\rho_f \frac{D\boldsymbol{v}}{Dt} = -\boldsymbol{\nabla}p + \mu\boldsymbol{\nabla}^2\boldsymbol{v} - \boldsymbol{\mathcal{F}}, \qquad \boldsymbol{\nabla}\cdot\boldsymbol{v} = 0 \qquad \text{in } \Omega, \tag{2.33}$$

$$\Delta M \frac{d\boldsymbol{U}}{dt} = \Delta M \boldsymbol{g} + \int_{\Omega_p} \boldsymbol{\mathcal{F}}\, d\Omega, \tag{2.34}$$

$$\boldsymbol{\omega} = \frac{1}{2V_p}\int_{\Omega_p} \boldsymbol{\nabla}\times\boldsymbol{v}\, d\Omega, \tag{2.35}$$

$$\boldsymbol{v} = \boldsymbol{U} + \boldsymbol{\omega}\times(\boldsymbol{x} - \boldsymbol{X}) \qquad \text{in } \Omega_p. \tag{2.36}$$

In such a formulation, $\boldsymbol{\mathcal{F}}$ is very similar to the Distributed Lagrange Multiplier in [Glowinski et al., 1999], but is different in the sense that it has a global effect on the fluid velocity through (2.33). Therefore, [Diaz-Goano et al., 2003] propose another Lagrange multiplier which is defined globally in Ω and has no restriction to be equal zero in Ω_f; it is defined as

a solution to the following boundary–value problem:

$$\begin{aligned} -\alpha\boldsymbol{\lambda} + \mu\boldsymbol{\nabla}^2\boldsymbol{\lambda} &= \boldsymbol{\mathcal{F}} \quad \text{in } \Omega, \\ \boldsymbol{\lambda} &= 0 \text{ on } \partial\Omega,\ \alpha > 0 \text{ is a constant.} \end{aligned} \tag{2.37}$$

The convenience of the equation (2.37) lies in its ability to be discretized with the global velocity space on domain Ω. Therefore, in such a formulation, the Lagrange multiplier does not require separate particle meshing and, in the case of many particles, the solution of equation (2.37) imposes the rigid–body constraint simultaneously for all off them.

Finally, after integrating $\boldsymbol{\mathcal{F}}$ by parts in Ω_p, the combined equations for a Fictitious Domain Method with global Lagrange multipliers can be obtained:

$$\rho_f \frac{D\boldsymbol{v}}{Dt} = -\boldsymbol{\nabla}p + \mu\boldsymbol{\nabla}^2\boldsymbol{v} + \alpha\boldsymbol{\lambda} - \mu\boldsymbol{\nabla}^2\boldsymbol{\lambda}, \qquad \boldsymbol{\nabla}\cdot\boldsymbol{v} = 0 \qquad \text{in } \Omega, \tag{2.38}$$

$$\Delta M \frac{d\boldsymbol{U}}{dt} = \Delta M\boldsymbol{g} - \int\limits_{\Omega_p} \alpha\boldsymbol{\lambda}\, d\Omega + \mu \int\limits_{\partial\Omega_p} \frac{\partial\boldsymbol{\lambda}}{\partial\boldsymbol{n}}\, \partial S, \tag{2.39}$$

$$\boldsymbol{\omega} = \frac{1}{2V_p} \int\limits_{\Omega_p} \boldsymbol{\nabla}\times\boldsymbol{v}\, d\Omega, \tag{2.40}$$

$$\boldsymbol{v} = \boldsymbol{U} + \boldsymbol{\omega}\times(\boldsymbol{x} - \boldsymbol{X}) \qquad \text{in } \Omega_p, \tag{2.41}$$

$$\frac{d\boldsymbol{\vartheta}}{dt} = \boldsymbol{\omega}, \qquad \frac{d\boldsymbol{X}}{dt} = \boldsymbol{U}. \tag{2.42}$$

2.5 A non–Lagrange multiplier version

A non-Lagrange multiplier version of the FDM has been derived by [Veeramani et al., 2007] and is based on the Global Lagrange Multiplier version presented in the previous section. Introducing proper operator splitting, the new formulation avoids using Lagrange multipliers for imposition of the rigid-body constraint; instead, the interaction force is resolved explicitly. In this new formulation, the end-of-step solid velocity is a solution to an implicit equation, which can be solved either iteratively in the case of pronounced rotational motion, or can be evaluated explicitly, when angular velocity is extrapolated from the previously computed quantities.

2.5.1 Combined formulation for fluid and solid

The new formulation starts off with the same idea of extending the fluid stress inside the solid phase, assuming that it is Newtonian, as described in the section 2.4. First, we state the non–dimensional versions of the equations (2.1) and (2.3) obtained by scaling the original equations with $L/\rho_f U^2$, with the fluid stress tensor $\boldsymbol{\sigma}$ extended inside Ω_p:

$$\frac{\partial \boldsymbol{v}}{\partial t} + \boldsymbol{v}\cdot\boldsymbol{\nabla}\boldsymbol{v} = -\boldsymbol{\nabla}p + \frac{1}{Re}\boldsymbol{\nabla}^2\boldsymbol{v}, \quad \boldsymbol{\nabla}\cdot\boldsymbol{v} = 0 \quad \text{in } \Omega_f, \tag{2.43}$$

$$\begin{aligned} &\frac{d\boldsymbol{U}}{dt} = \frac{\rho_r - 1}{\rho_r}\frac{1}{Fr}\boldsymbol{e}_g + \frac{1}{\rho_r V_p}\int_{\Omega_p} \boldsymbol{\nabla}\cdot\boldsymbol{\sigma}\, d\Omega \\ &\frac{d(\mathbb{I}_p\boldsymbol{\omega})}{dt} = \boldsymbol{T}, \qquad \frac{d\boldsymbol{\vartheta}}{dt} = \boldsymbol{\omega}, \qquad \frac{d\boldsymbol{X}}{dt} = \boldsymbol{U}, \end{aligned} \tag{2.44}$$

with no–slip boundary condition $\boldsymbol{v} = \boldsymbol{U} + \boldsymbol{\omega}\times(\boldsymbol{x} - \boldsymbol{X})$ on the particle surface $\partial\Omega_p$, solid inertia tensor $\mathbb{I}_p$, rotational vector $\boldsymbol{\vartheta}$ and $\boldsymbol{x}, \boldsymbol{U}, \boldsymbol{\omega}$ and $\boldsymbol{X}$ defined as previously, to be a point in the solid domain, particle centroid velocity, angular velocity and the center of mass position. The scaling coefficients $Re = UL/\nu$ and $Fr = U^2/gL$ are defined through the characteristic velocity U, the characteristic length L, the fluid kinematic viscosity ν and the magnitude of the gravity acceleration g, with gravity orientation given by the unit vector $\boldsymbol{e}_g$.

Then, the interaction force is defined over the entire domain $\Omega = \Omega_f \cup \Omega_p$ as proposed by [Diaz-Goano et al., 2003]:

$$\hat{\boldsymbol{\mathcal{F}}} = \begin{cases} -\dfrac{D\boldsymbol{v}}{Dt} + \dfrac{1}{Re}\boldsymbol{\nabla}^2\boldsymbol{v} - \boldsymbol{\nabla}p & \text{in } \Omega_p \\ 0 & \text{in } \Omega_f, \end{cases} \tag{2.45}$$

allowing to extend equation (2.43) from Ω_f to Ω:

$$\frac{\partial \boldsymbol{v}}{\partial t} + \boldsymbol{v}\cdot\boldsymbol{\nabla}\boldsymbol{v} = -\boldsymbol{\nabla}p + \frac{1}{Re}\boldsymbol{\nabla}^2\boldsymbol{v} - \hat{\boldsymbol{\mathcal{F}}}, \quad \boldsymbol{\nabla}\cdot\boldsymbol{v} = 0 \quad \text{in } \Omega, \tag{2.46}$$

and rewrite the particle momentum equation (2.44) as

$$\frac{d\boldsymbol{U}}{dt} - \frac{1}{\rho_r V_p}\int_{\Omega_p} \frac{D\boldsymbol{v}}{Dt}\, d\Omega = \frac{1}{\rho_r V_p}\int_{\Omega_p} \left[\frac{\rho_r - 1}{Fr}\boldsymbol{e}_g + \hat{\boldsymbol{\mathcal{F}}}\right]\, d\Omega. \tag{2.47}$$

Imposing the additional constraint $\boldsymbol{v} = \boldsymbol{u}$ in Ω_p, similarly to (2.30) in section 2.4, we

recognize that the fluid acceleration in Ω_p should be the same as the acceleration of the rigid particle, therefore we can write

$$\frac{d\boldsymbol{U}}{dt} = \frac{1}{V_p}\int\limits_{\Omega_p} \frac{D\boldsymbol{v}}{Dt}\, d\Omega \tag{2.48}$$

which turns (2.47) into

$$(\rho_r - 1)\frac{d\boldsymbol{U}}{dt} = \frac{1}{V_p}\int\limits_{\Omega_p} \left[\frac{\rho_r - 1}{Fr}\boldsymbol{e}_g + \hat{\boldsymbol{\mathcal{F}}}\right]\, d\Omega. \tag{2.49}$$

At this point, [Veeramani et al., 2007] propose to define the interaction force as

$$\boldsymbol{\mathcal{F}} = \begin{cases} \dfrac{1}{Fr}\boldsymbol{e}_g + \dfrac{1}{\rho_r - 1}\hat{\boldsymbol{\mathcal{F}}} & \text{in } \Omega_p \\ 0 & \text{in } \Omega_f, \end{cases}$$

and rewrite the final set of the governing equations (2.43) and (2.44) to obtain:

$$\frac{\partial \boldsymbol{v}}{\partial t} + \boldsymbol{v}\cdot\boldsymbol{\nabla}\boldsymbol{v} = -\boldsymbol{\nabla}p + \frac{1}{Re}\boldsymbol{\nabla}^2\boldsymbol{v} + (\rho_r - 1)(\boldsymbol{G} - \boldsymbol{\mathcal{F}}), \quad \boldsymbol{\nabla}\cdot\boldsymbol{v} = 0 \quad \text{in } \Omega, \tag{2.50}$$

$$\frac{d\boldsymbol{U}}{dt} = \frac{1}{V_p}\int\limits_{\Omega_p} \boldsymbol{\mathcal{F}}\, d\Omega, \qquad \boldsymbol{G} = \begin{cases} \dfrac{1}{Fr}\boldsymbol{e}_g & \text{in } \Omega_p \\ 0 & \text{in } \Omega_f, \end{cases} \tag{2.51}$$

$$\boldsymbol{\omega} = \frac{1}{2V_p}\int\limits_{\Omega_p} \boldsymbol{\nabla}\times\boldsymbol{v}\, d\Omega \quad \text{(the same as in section 2.4)}, \tag{2.52}$$

$$\boldsymbol{v} = \boldsymbol{U} + \boldsymbol{\omega}\times(\boldsymbol{x} - \boldsymbol{X}) \qquad \text{in } \Omega_p, \tag{2.53}$$

$$\frac{d\boldsymbol{\vartheta}}{dt} = \boldsymbol{\omega}, \qquad \frac{d\boldsymbol{X}}{dt} = \boldsymbol{U}. \tag{2.54}$$

Equation (2.53) should be recognized as a side constraint for the momentum equations (2.50) and (2.51). In the previous sections, we have established similar systems following [Glowinski et al., 1999] and [Diaz-Goano et al., 2003], who use Lagrange multipliers to impose the constraint (2.53). Instead, in the present formulation, [Veeramani et al., 2007] are able to derive an explicit equation for the interaction force $\boldsymbol{\mathcal{F}}$ eliminating the need in the Lagrange multipliers.

2.5.2 Discretization and operator splitting

A second order incremental pressure-correction scheme is used to decouple the velocity and pressure at each time step. This allows us to solve a sequence of elliptic problems for the velocity and the pressure, which significantly simplifies solution of the Navier-Stokes equations in real applications. The approach is as follows:

Predictor

The position and orientation of the particle at time step t^{n+1} are predicted explicitly by

$$\boldsymbol{X}^p = \boldsymbol{X}^{n-1} + 2\Delta t \boldsymbol{U}^n \qquad \boldsymbol{\vartheta}^p = \boldsymbol{\vartheta}^{n-1} + 2\Delta t \boldsymbol{\omega}^n$$

where Δt is the time step.

Advection–diffusion step

Then, we solve for $\boldsymbol{v}^*(\boldsymbol{x})$ from

$$\begin{aligned} \tau_0 \boldsymbol{v}^* - \frac{1}{Re}\boldsymbol{\nabla}^2 \boldsymbol{v}^* &= -\tau_1 \tilde{\boldsymbol{v}}^n - \tau_2 \tilde{\boldsymbol{v}}^{n-1} - \boldsymbol{\nabla} p^n + (\rho_r - 1)\boldsymbol{G}^p \qquad \text{in } \Omega, \\ \boldsymbol{v}^* &= \boldsymbol{v}_{\partial\Omega} \qquad \text{on } \partial\Omega \end{aligned} \tag{2.55}$$

where $\tau_0 = 3/(2\Delta t)$, $\tau_1 = -2/\Delta t$ and $\tau_2 = 1/(2\Delta t)$, with superscript $[\cdot]^p$ indicating parameters dependent on the predicted solid position $\boldsymbol{X}^p$ and orientation $\boldsymbol{\vartheta}^p$. In equation (2.55), we perform time splitting of the convective terms from the generalized Stokes problem as explained in [Minev and Ross Ethier, 1998]. In this approach, the material derivative on the left hand side of (2.50) is approximated with the second order backward difference scheme as:

$$\frac{\partial \boldsymbol{v}^{n+1}}{\partial t} + ((\boldsymbol{v}^{n+1})\cdot\boldsymbol{\nabla})\boldsymbol{v}^{n+1} \approx \frac{3\boldsymbol{v}^{n+1} - 4\tilde{\boldsymbol{v}}^n + \tilde{\boldsymbol{v}}^{n-1}}{2\Delta t} = \tau_0 \boldsymbol{v}^{n+1} + \tau_1 \tilde{\boldsymbol{v}}^n + \tau_2 \tilde{\boldsymbol{v}}^{n-1}, \tag{2.56}$$

with $\tilde{\boldsymbol{v}}^n(\boldsymbol{x}) = \boldsymbol{v}(\boldsymbol{Z}(t^n;\boldsymbol{x}), t^n)$ and $\tilde{\boldsymbol{v}}^{n-1}(\boldsymbol{x}) = \boldsymbol{v}(\boldsymbol{Z}(t^{n-1};\boldsymbol{x}), t^{n-1})$ being the velocities from the time levels n and $n-1$, which have been advected alongside an approximation to the characteristics. In such a formulation, $\boldsymbol{Z}(t^n;\boldsymbol{x})$ and $\boldsymbol{Z}(t^{n-1};\boldsymbol{x})$ are the solutions to the following terminal-value problem for pure advection equation between t^{n-1} and t^{n+1}:

$$\begin{cases} \dfrac{d\boldsymbol{Z}(s)}{ds} = \boldsymbol{v}(\boldsymbol{Z}(s), s), \\ \boldsymbol{Z}(t^{n+1}) = \boldsymbol{x}, \quad \boldsymbol{x} \in \Omega, \quad s \in [t^{n-1},\ t^{n+1}]. \end{cases} \tag{2.57}$$

Velocity projection

Project the approximation $\boldsymbol{v}^*(\boldsymbol{x})$ onto the solenoidal subspace of $\boldsymbol{L}^2(\Omega)$ in order to recover the divergence-free velocity $\boldsymbol{v}^{**}(\boldsymbol{x})$:

$$\tau_0(\boldsymbol{v}^{**} - \boldsymbol{v}^*) = -\boldsymbol{\nabla}(p^{n+1} - p^n) \qquad \text{in } \Omega \tag{2.58}$$

$$\boldsymbol{\nabla}\cdot\boldsymbol{v}^{**} = 0 \qquad \text{in } \Omega \tag{2.59}$$

$$(\boldsymbol{v}^{**} - \boldsymbol{v}^*)\cdot\boldsymbol{n} = 0 \qquad on\ \partial\Omega \tag{2.60}$$

where $\boldsymbol{n}$ is the outward normal to $\partial\Omega$.

Rigid body constraint

In the following, derivation of the explicit relation for $\boldsymbol{\mathcal{F}}$ is performed. It follows [Veeramani et al., 2007] and is based on the Marchuk–Yanenko splitting approach.

First, we predict the rigid body centroid velocity with the approximation to (2.48):

$$\tau_0\boldsymbol{U}^p + \tau_1\boldsymbol{U}^n + \tau_2\boldsymbol{U}^{n-1} = \frac{1}{V_p}\int\limits_{\Omega_p^p}(\tau_0\boldsymbol{v}^{**} + \tau_1\tilde{\boldsymbol{v}}^n + \tau_2\tilde{\boldsymbol{v}}^{n-1})\, d\Omega. \tag{2.61}$$

Then, since in (2.55) there was no interaction force term due to the solid, the following correction should be considered:

$$\tau_0(\boldsymbol{v}^{n+1} - \boldsymbol{v}^{**}) = -(\rho_r - 1)\boldsymbol{\mathcal{F}} \quad \text{in } \Omega, \tag{2.62}$$

as well as correction to the particle centroid velocity:

$$\tau_0(\boldsymbol{U}^{n+1} - \boldsymbol{U}^p) = \frac{1}{V_p}\int\limits_{\Omega_p^p}\boldsymbol{\mathcal{F}}\, d\Omega, \tag{2.63}$$

and the rigid–body constraint

$$\boldsymbol{v}^{n+1} - (\boldsymbol{U}^{n+1} + \boldsymbol{\omega}^{n+1}\times(\boldsymbol{x} - \boldsymbol{X}^p)) = 0 \qquad \text{in } \Omega_p^p. \tag{2.64}$$

The expression for the interaction force $\boldsymbol{\mathcal{F}}$ can be found by subtracting equation (2.63) from equation (2.62):

$$-(\rho_r - 1)\boldsymbol{\mathcal{F}} - \frac{1}{V_p}\int\limits_{\Omega_p^p}\boldsymbol{\mathcal{F}}\, d\Omega = \tau_0(\boldsymbol{v}^{n+1} - \boldsymbol{U}^{n+1} + \boldsymbol{U}^p - \boldsymbol{v}^{**}), \tag{2.65}$$

and plugging in the rigid-body constraint for $\boldsymbol{v}^{n+1} - \boldsymbol{U}^{n+1}$:

$$-(\rho_r - 1)\boldsymbol{\mathcal{F}} - \frac{1}{V_p}\int\limits_{\Omega_p^p} \boldsymbol{\mathcal{F}}\, d\Omega = \tau_0(\boldsymbol{\omega}^{n+1}\times(\boldsymbol{x} - \boldsymbol{X}^p) + \boldsymbol{U}^p - \boldsymbol{v}^{**}). \tag{2.66}$$

This can be further simplified, if we integrate (2.65) over the solid domain and use the integral of the rigid-body constraint

$$\int\limits_{\Omega_p^p} (\boldsymbol{v}^{n+1} - \boldsymbol{U}^{n+1})\, d\Omega = \int\limits_{\Omega_p^p} \boldsymbol{\omega}^{n+1}\times(\boldsymbol{x} - \boldsymbol{X}^p))\, d\Omega = 0$$

to find:

$$\int\limits_{\Omega_p^p} \boldsymbol{\mathcal{F}}\, d\Omega = \frac{\tau_0}{\rho_r}\int\limits_{\Omega_p^p} (\boldsymbol{v}^{**} - \boldsymbol{U}^p)\, d\Omega. \tag{2.67}$$

Plugging (2.67) into equation (2.66), we find the explicit form of the interaction force $\boldsymbol{\mathcal{F}}$ in the entire domain Ω:

$$\begin{aligned} -(\rho_r - 1)\boldsymbol{\mathcal{F}} = \tau_0\Bigg[\frac{1}{\rho_r V_p}\int\limits_{\Omega_p^p} (\boldsymbol{v}^{**} - \boldsymbol{U}^p)\, d\Omega + \\ + \boldsymbol{\omega}^{n+1}\times(\boldsymbol{x} - \boldsymbol{X}^p) + \boldsymbol{U}^p - \boldsymbol{v}^{**}\Bigg]\chi^p(\boldsymbol{x}), \end{aligned} \tag{2.68}$$

where χ^p is the indicator function such that

$$\chi^p = \begin{cases} 1 & \text{in } \Omega_p^p, \\ 0 & \text{in } \Omega_f^p. \end{cases}$$

The end of step particle centroid velocity can now be found from (2.63) as

$$\begin{aligned} \boldsymbol{U}^{n+1} &= \boldsymbol{U}^p + \frac{1}{\rho_r V_p}\int\limits_{\Omega_p^p} (\boldsymbol{v}^{**} - \boldsymbol{U}^p)\, d\Omega \\ &= \frac{\rho_r - 1}{\rho_r}\boldsymbol{U}^p + \frac{1}{\rho_r V_p}\int\limits_{\Omega_p^p} \boldsymbol{v}^{**}\, d\Omega, \end{aligned} \tag{2.69}$$

while the end of step fluid velocity becomes

$$\boldsymbol{v}^{n+1} = \boldsymbol{v}^{**} + \left[\boldsymbol{U}^{n+1} + \boldsymbol{\omega}^{n+1}\times(\boldsymbol{x} - \boldsymbol{X}^p) - \boldsymbol{v}^{**}\right]\chi^p. \tag{2.70}$$

If we employ equation (2.52) in the form

$$\boldsymbol{\omega}^{n+1} = \frac{1}{2V_p}\int\limits_{\Omega_p^p} \boldsymbol{\nabla}\times\boldsymbol{v}^{n+1}\, d\Omega$$

as an expression for the angular velocity, then it becomes apparent that the equation for the fluid velocity (2.70) is implicit and nonlinear. One way to address this would be to solve (2.70) iteratively, or, when the angular velocity of the solid is expected to be small, $\boldsymbol{\omega}$ can be extrapolated with

$$\boldsymbol{\omega}^{n+1} = \frac{1}{2V_p}\int\limits_{\Omega_p^p} \boldsymbol{\nabla}\times\boldsymbol{v}^{**}\, d\Omega. \tag{2.71}$$

Corrector

The position and orientation of the particle are corrected using

$$\boldsymbol{X}^{n+1} = \boldsymbol{X}^n + \frac{\Delta t}{2}(\boldsymbol{U}^{n+1} + \boldsymbol{U}^n) \text{ and } \boldsymbol{\vartheta}^{n+1} = \boldsymbol{\vartheta}^n + \frac{\Delta t}{2}(\boldsymbol{\omega}^{n+1} + \boldsymbol{\omega}^n). \tag{2.72}$$

Note, that all integrals in the described algorithm are evaluated in the solid domain Ω_p^p which is explicitly predicted at the beginning of each time step. Moreover, when the extrapolation (2.71) for the angular velocity is used, the resulting method becomes explicit in solid velocity as well. These simplifications, which significantly reduce the computational complexity of the algorithm per time step, will inevitably require very small time steps in order to maintain accuracy and stability. Therefore, the trade–off between the time step size and the complexity of the implicit iterations should be considered carefully for each particular problem.

2.6 A two-grid Fictitious Domain Method – multi-scale approach

The Fictitious Domain Methods presented in the previous sections are designed to simulate solid particles in domain, where the solid and fluid length scales are comparable. Particularly, the global Lagrange multiplier formulation in section 2.4 and non-Lagrange multiplier version from section 2.5 find their application in the simulations of sedimenting fluidized beds of many solid particles. These formulations assume that the governing equations defined on the computational domain $\Omega = \Omega_f \cup \Omega_p$ (Figure 2.1) are discretized on a grid $\mathcal{G}_H$ which fits Ω and such that the grid size H is well suited to resolve both fluid and solid phases.

However, there are some biological particulate flows, such as the flows of inhalable aerosols in the lungs, which are characterized by significant differences in the domain and suspended solid length scales. Particles reaching the tracheo-bronchial region are so small, compared to the airway dimensions, and their mass fraction is so insignificant, that the fluid flow at the lung airway scale is not affected by the solid inclusions. Therefore, it is sufficient to discretize the fluid dynamics equations on a grid $\mathcal{G}_H$ associated with the airway domain, having grid size H correspondent to the airway fluid flow length scale. On the other hand, rigid-body motion, in the cases when particles are non-spherical, can not be resolved well without resolving the correct hydrodynamic forces and torques imposed by the fluid on a particle surface. In this case, correct resolution of the fluid flow is only possible when the equations that describe coupled fluid-solid dynamics are discretized on a grid $\mathcal{G}_h$ with the grid size h correspondent to the particle length scale. In view of these arguments, correct modelling of the particle deposition in the lung airways will require $H \gg h$, which, if approached naively, demands so much computational resources, that application to realistic problems is not feasible.

In order to address the aforementioned problems, [Dechaume et al., 2010] propose a two-grid FDM for particles of a very small size. They introduce two grids, each of them fine enough to accurately resolve the flow on its corresponding scale. Therefore, when an object of a very small size is simulated within a much larger domain, the micro-scale grid $\mathcal{G}_h$ with the grid size h surrounds the object and is attached to its centre of mass following its motion. The macro-scale grid $\mathcal{G}_H$ with the grid size H covers the entire computational domain Ω and the micro-scale grid $\mathcal{G}_h$ becomes embedded in $\mathcal{G}_H$, see Figure 2.2.

The idea of the multiscale approach is to resolve the fluid flow on the macro-grid $\mathcal{G}_H$ first, without the presence of the solid, and then transfer the so computed velocity as

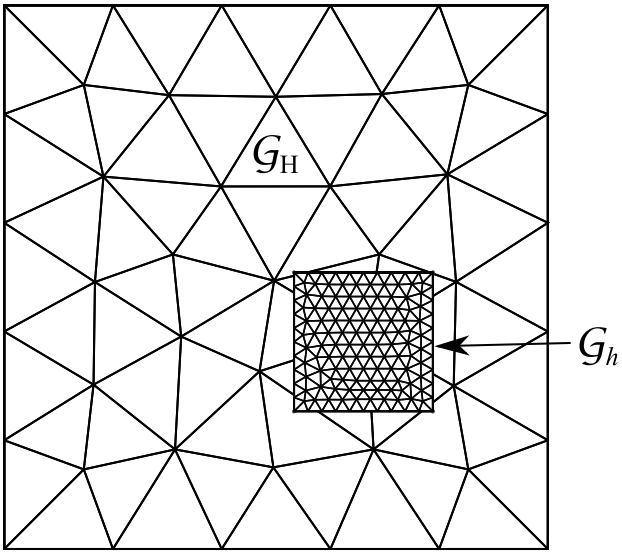

Figure 2.2: Computational grids in two-grid FDM formulation.

a Dirichlet boundary condition onto the micro-grid surface $\partial\mathcal{G}_h$, solving the micro-scale problem discretized on $\mathcal{G}_h$ with the spatial resolution appropriate for the object's size. The described approach is only consistent as long as the $H \gg h$ condition holds.

2.6.1 Governing equations

For solid micro-particles simulations the two-grid multiscale algorithm is combined with a slightly modified FDM formulation from Section 2.5.

The fluid flow on the macro-scale is governed by the Navier-Stokes equations:

$$\frac{\partial \boldsymbol{v}_H}{\partial t} + \boldsymbol{v}_H \cdot \boldsymbol{\nabla} \boldsymbol{v}_H = -\boldsymbol{\nabla} p_H + \frac{1}{Re_H} \boldsymbol{\nabla}^2 \boldsymbol{v}_H, \quad \boldsymbol{\nabla} \cdot \boldsymbol{v}_H = 0, \tag{2.73}$$

which are discretized on the macro-grid $\mathcal{G}_H$, with p_H, $\boldsymbol{v}_H$ being the fluid pressure and velocity and $Re_H = U_H L_H / \nu$ is the Reynolds number defined using the characteristic length and characteristic velocity appropriate for the macro-scale flow.

On the micro-grid $\mathcal{G}_h$, we discretize a modified version of the system (2.50)–(2.54):

$$\frac{\partial \boldsymbol{v}}{\partial t} + ((\boldsymbol{v}-\boldsymbol{U})\cdot\boldsymbol{\nabla})\boldsymbol{v} = -\boldsymbol{\nabla} p + \frac{1}{Re}\boldsymbol{\nabla}^2\boldsymbol{v} + (\rho_r - 1)(\boldsymbol{G} - \boldsymbol{\mathcal{F}}), \quad \boldsymbol{\nabla}\cdot\boldsymbol{v} = 0 \quad \text{in } \Omega, \tag{2.74}$$

$$\frac{d\boldsymbol{U}}{dt} = \frac{1}{V_p}\int\limits_{\Omega_p} \boldsymbol{\mathcal{F}}\, d\Omega, \qquad \boldsymbol{G} = \begin{cases} \dfrac{1}{Fr}\boldsymbol{e}_g & \text{in } \Omega_p \\ 0 & \text{in } \Omega_f, \end{cases} \tag{2.75}$$

$$\frac{d(\mathbb{I}_p\boldsymbol{\omega})}{dt} = \frac{1}{\rho_r}\int\limits_{\Omega_p} (\boldsymbol{x}-\boldsymbol{X})\times\frac{D\boldsymbol{v}}{Dt}\, d\Omega, \tag{2.76}$$

$$\boldsymbol{v} = \boldsymbol{U} + \boldsymbol{\omega}\times(\boldsymbol{x}-\boldsymbol{X}) \qquad \text{in } \Omega_p, \tag{2.77}$$

$$\frac{d\boldsymbol{\vartheta}}{dt} = \boldsymbol{\omega}, \qquad \frac{d\boldsymbol{X}}{dt} = \boldsymbol{U}, \tag{2.78}$$

where Ω is the domain covered by grid $\mathcal{G}_h$, Ω_f is the sub-domain of Ω containing fluid, and Ω_p is the solid sub-domain, such that $\Omega = \Omega_f \cup \Omega_p$. Similarly, the notation of the previous section is adopted here for quantities defined on Ω with the scaling performed using the characteristic length and the characteristic velocity based on the micro-scale parameters. Additionally, the micro-grid $\mathcal{G}_h$ is attached to the particle center of mass $\boldsymbol{X}$ so that particle is free to rotate in Ω.

One change we have to make to the system (2.50)–(2.54) is to introduce the total derivative in the equation (2.74) in a form which is natural for Arbitrary Lagrangian-Eulerian (ALE) methods. Indeed, since the micro-grid is moving with the particle centroid velocity, we have to reflect that in the governing equations as it is done in ALE. Although, since the grid motion is linear, *i.e.*, parallel translation, it is only the convective term that has to be modified.

Additionally, [Dechaume et al., 2010] propose to find the angular velocity by solving equation (2.76) instead of using for this purpose equation (2.52). Based on their numerical experiments, [Dechaume et al., 2010] conclude that for ellipsoids, equation (2.52) performs not as well as it does for spherical particles. Therefore, they use equation (2.76) which also follows from (2.77).

2.6.2 Algorithm description

Implementation of the approach is as follows.

1. Find solution on macro-grid

Resolve the Navier-Stokes equations (2.73) on the macro-grid $\mathcal{G}_H$ ignoring the effect of

the solid. Since the length scale of the solid is assumed much smaller than the length scale on $\mathcal{G}_H$, flow on the macro-grid does not "feel"the presence of the particle.

2. Predict position of the micro-grid at t^{n+1}

Predict position and orientation of the particle at time step t^{n+1}:

$$\boldsymbol{X}^p = \boldsymbol{X}^{n-1} + 2\Delta t \boldsymbol{U}^n \qquad \boldsymbol{\vartheta}^p = \boldsymbol{\vartheta}^{n-1} + 2\Delta t \boldsymbol{\omega}^n,$$

which also defines predicted position of $\mathcal{G}_h(t^{n+1})$ denoted as $\mathcal{G}_h^p$.

3. Transfer velocity from macro-grid as a boundary condition on micro-grid

Use the resulting velocity field on $\mathcal{G}_H$ to interpolate Dirichlet boundary conditions at $\partial\mathcal{G}_h^p$ boundary of $\mathcal{G}_h^p$. The interpolation can be performed with regular $\mathbb{P}_2$ basis functions. Zero velocity is prescribed on boundary nodes when they appear outside of the computational grid $\mathcal{G}_H$ as a result of particle motion.

4. Impose zero flux through micro–grid surface

In general, the interpolated velocity $\hat{\boldsymbol{v}}_H$ on $\partial\mathcal{G}_h^p$ produces non-zero flux through the surface. Therefore, we correct its normal component with the simple Lagrange multiplier problem

$$\begin{aligned} \boldsymbol{v}_{\partial\Omega}\cdot\boldsymbol{n} &= \hat{\boldsymbol{v}}_H\cdot\boldsymbol{n} + \hat{\boldsymbol{\lambda}} \qquad on\ \partial\Omega^p \\ \int_{\partial\Omega^p} \boldsymbol{v}_{\partial\Omega}\cdot\boldsymbol{n}\, dS &= 0, \end{aligned} \tag{2.79}$$

discretized on the micro-grid boundary $\partial\mathcal{G}_h^p$ the discrete version of the continuous boundary $\partial\Omega^p$.

5. Resolve fluid flow and solid motion on the micro-grid

Using the same time discretization and operator splitting as in section 2.5.2, we perform the following steps:

Solve for $\boldsymbol{v}^*(\boldsymbol{x})$:

$$\begin{aligned} \tau_0\boldsymbol{v}^* - \frac{1}{Re}\boldsymbol{\nabla}^2\boldsymbol{v}^* &= -\tau_1\tilde{\boldsymbol{v}}^n - \tau_2\tilde{\boldsymbol{v}}^{n-1} - \boldsymbol{\nabla}p^n + (\rho_r - 1)\boldsymbol{G}^p \qquad \text{in } \Omega^p, \\ \boldsymbol{v}^* &= \boldsymbol{v}_{\partial\Omega} \qquad on\ \partial\Omega^p \end{aligned} \tag{2.80}$$

discretized on $\mathcal{G}_h^p$. It is important to note here, that $\tilde{\boldsymbol{v}}^n(\boldsymbol{x}) = \boldsymbol{v}(\boldsymbol{Z}(t^n;\boldsymbol{x}), t^n)$ and $\tilde{\boldsymbol{v}}^{n-1}(\boldsymbol{x}) = \boldsymbol{v}(\boldsymbol{Z}(t^{n-1};\boldsymbol{x}), t^{n-1})$ are the velocities from the time levels n and $n-1$,

which have been advected alongside an approximation to the characteristics as before. Although, due to the left hand side of (2.74), the feet of the characteristics at time levels n and $n-1$, $\boldsymbol{Z}(t^n;\boldsymbol{x})$ and $\boldsymbol{Z}(t^{n-1};\boldsymbol{x})$ respectively, are the solutions to the modified terminal–value problem (2.57):

$$\begin{cases} \dfrac{d\boldsymbol{Z}(s)}{ds} = \boldsymbol{v}(\boldsymbol{Z}(s),s) - \boldsymbol{U}(s), \\ \boldsymbol{Z}(t^{n+1}) = \boldsymbol{x}, \quad \boldsymbol{x} \in \mathcal{G}_h^p, \quad s \in [t^{n-1},\ t^{n+1}]. \end{cases}$$

Solve for pressure p^{n+1} and incompressible velocity $\boldsymbol{v}^{**}$:

$$\begin{aligned} \tau_0(\boldsymbol{v}^{**} - \boldsymbol{v}^*) &= -\boldsymbol{\nabla}(p^{n+1} - p^n) && \text{in } \Omega^p \\ \boldsymbol{\nabla}\cdot\boldsymbol{v}^{**} &= 0 && \text{in } \Omega^p \\ (\boldsymbol{v}^{**} - \boldsymbol{v}^*)\cdot\boldsymbol{n} &= 0 && \text{on } \partial\Omega^p \end{aligned}$$

on $\mathcal{G}_h^p$, with $\boldsymbol{n}$ being the outward normal to $\partial\mathcal{G}_h^p$.

Resolve rigid body motion:
The rigid body velocity is first predicted by integrating the fluid acceleration in Ω_p^p on $\mathcal{G}_h^p$:

$$\tau_0\boldsymbol{U}^p + \tau_1\boldsymbol{U}^n + \tau_2\boldsymbol{U}^{n-1} = \frac{1}{V_p}\int\limits_{\Omega_p^p}\left(\frac{D\boldsymbol{v}}{Dt}\right)^{n+1} d\Omega, \tag{2.81}$$

where

$$\left(\frac{D\boldsymbol{v}}{Dt}\right)^{n+1} = \tau_0\boldsymbol{v}^{**} + \tau_1\tilde{\boldsymbol{v}}^n + \tau_2\tilde{\boldsymbol{v}}^{n-1}. \tag{2.82}$$

Then, we eliminate the Lagrange multiplier $\boldsymbol{\mathcal{F}}$ from the set of equations, which yields the end-of-step centroidal and angular velocities:

$$\boldsymbol{U}^{n+1} = \frac{1}{\rho_r V_p}\int\limits_{\Omega_p^p}\boldsymbol{v}^{**}\, d\Omega + \frac{\rho_r - 1}{\rho_r}\boldsymbol{U}^p, \tag{2.83}$$

and

$$\boldsymbol{\omega}^{n+1} = \frac{(\mathbb{I}_p^p)^{-1}}{\tau_0}\left(\frac{1}{\rho_r}\int\limits_{\Omega_p^p}(\boldsymbol{x}^{n+1}-\boldsymbol{X}^p)\times\left(\frac{D\boldsymbol{v}}{Dt}\right)^{n+1}\,d\Omega - \right. \\ \left. - \tau_1(\mathbb{I}_p\boldsymbol{\omega})^n - \tau_2(\mathbb{I}_p\boldsymbol{\omega})^{n-1}\right), \tag{2.84}$$

where $\mathbb{I}_p^p$ is the predicted inertia tensor, and integration over Ω_p^p is performed on the micro-grid $\mathcal{G}_h$.

Correct fluid velocity and solid position:
Finally, we have the end-of-step solution for the fluid on the micro-grid:

$$\boldsymbol{v}^{n+1}(\boldsymbol{x}) = \begin{cases} \boldsymbol{v}^{**}(\boldsymbol{x}), & in\ \Omega_f^p, \\ \boldsymbol{U}^{n+1} + \boldsymbol{\omega}^{n+1}\times(\boldsymbol{x}-\boldsymbol{X}^p), & in\ \Omega_p^p, \end{cases} \tag{2.85}$$

which could be imposed pointwise or in the L^2 sense on $\mathcal{G}_h^p$.

The position and orientation of the particle, as well as the end of step position of $\mathcal{G}_h^{n+1}$ are corrected using

$$\boldsymbol{X}^{n+1} = \boldsymbol{X}^n + \frac{\Delta t}{2}(\boldsymbol{U}^{n+1}+\boldsymbol{U}^n), \qquad \boldsymbol{\vartheta}^{n+1} = \boldsymbol{\vartheta}^n + \frac{\Delta t}{2}(\boldsymbol{\omega}^{n+1}+\boldsymbol{\omega}^n). \tag{2.86}$$

6. Next time step

Go to step 1, in order to perform another time step.

The algorithm is tested and validated in [Dechaume et al., 2010] on the problem of a sedimenting sphere in a tank, on the tumbling motion of an ellipsoid in a linear shear flow (Jeffery orbits [Jeffery, 1922]) and on the problem of a small ellipsoid migrating in a bifurcating pipe, which resembles the tracheo-bronchial airway bifurcation.

Chapter 3

Dynamics of solid particles in a fluid

This chapter is based on and follows closely previously published paper:
A. Roshchenko, W. H. Finlay, and P. D. Minev. The Aerodynamic Behavior of Fibers in a Linear Shear Flow. *Aerosol Science and Technology*, 45(10):1260–1271, Oct. 2011.
Some results presented in this chapter have been previously published in:
R. C. Martinez, A. Roshchenko, P. D. Minev, and W. H. Finlay. Simulation of enhanced deposition due to magnetic field alignment of ellipsoidal particles in a lung bifurcation. *Journal of Aerosol Medicine and Pulmonary Drug Delivery*, 26(1):31–40, Feb. 2013.

3.1 Introduction

Various factors influencing fiber deposition have been studied by numerous authors since the 1960's. However, a complete mechanistic model of fiber dynamics in narrow tubes like those of the airways in the lungs which would account for all major factors affecting deposition, including diffusion, gravitational sedimentation, inertial impaction and interception, as well as fiber shape, has not been developed yet.

When developing deposition models for inertial impaction and interception, recent advances have been observed in the study of how inertia influences the deposition of man-made fibers in the upper airways [Su and Cheng, 2009], though one of the problems yet to be self-consistently addressed is the orientation of the real fibers with respect to the flow direction in an airway. Fiber orientation depends on a number of factors such as airway geometry, type of fluid flow in the airway, and particle size and shape. Since airway geometry and flow conditions vary greatly along the particle path through the lungs, only general statements

about fiber orientation can be made.

Experiments with rods [Anczurowski and Mason, 1967], ellipsoidal bodies [Anczurowski and Mason, 1968], and theory developed by [Jeffery, 1922] for neutrally buoyant prolate spheroids, with the later extensions by [Asgharian and Anjilvel, 1995] in order to include inertia and [Podgórski and Gradon, 1990] for flexible slender bodies, allow us to expect alignment of long straight fibers with the flow in the lungs. But this expectation cannot be extended to all fibrous aerosols, since fibrous aerosols, even those composed of only straight fibers, when observed through a microscope [Hwang, 1983], reveal significant numbers of irregularly shaped particles. Such particles form when regular particles are contaminated with dust or several particles stick together to form particle aggregations, and due to their irregular shape cannot be expected to align with the flow.

Unfortunately, we know very little as to how fibers of different geometries will orient in an airway. In this regard, it is worth mentioning the analytical work by [Cox, 1970]. Ignoring fluid inertia, he derived an asymptotic expansion in terms of the ratio of the cross-sectional radius to the body length for force per unit length applied on a long solid slender body immersed in an undisturbed fluid flow. Worked examples present resistance to translation for long slender bodies with curved centerline. [Cox, 1971] further develops this approach and applies it to find the total force and torque on a long slender body in a linear shear flow. Unfortunately, [Cox, 1971] assumes an axisymmetric shape and so his analysis does not apply for arbitrary fiber shapes.

[Podgórski and Gradon, 1990, 1998] derived equations of motion for deformable and rigid elongated fibrous particles in an arbitrary flow structure. For deformable particles the derivation is done by considering local motion of thin slices forming the particle body. Dynamics of solid particles is considered as a limiting case of the flexible fibers with infinite elastic modulus [Podgórski and Gradon, 1998]. The equations are derived under the assumption of circular particle cross-section with constant radius along the axis of symmetry, and are easy to use when viscous drag per unit length exerted by the fluid is known, *e.g.* the case of creeping flow when the corresponding body forces are determined from slender body theory [Cox, 1970]. Using these equations [Podgórski and Gradon, 1990] report orientation, deformation and deposition efficiency for perfectly flexible slender particles under flow conditions representative of the lower human airways.

Additionally, [Asgharian and Ahmadi, 1998] approximated curved fibers with ellipsoids rigidly connected to each other under different angles. They derived a system of differential equations governing the full body motion of a fiber made of two ellipsoids by using analytical expressions for fluid forces and torque acting on a single ellipsoid. The system is solved

numerically and the results are used to study the deposition rate of such fibers in a narrow airway. Though the authors did not present a detailed description of the rotational motion for a single fiber, they did note a lack of orderly movement for their particles and showed dependence of deposition rates on particle geometry.

Since there is a lack of scientific data on how fluid flows influence the orientation of particles of various shapes, analytical models developed over the years [Harris and Fraser, 1976; Asgharian and Yu, 1988; Balásházy et al., 1990] and more recently, [Sturm and Hofmann, 2006; Zhou et al., 2008; Inthavong et al., 2009] offer formulae for deposition efficiencies only for long straight fibers. These models cover different flow conditions such as laminar flow in the lung airways (some authors assume that the fluid flow profile is uniform in the straight portions and radially dependent on the curved portions of the airways as in [Balásházy et al., 1990], while others assume it to be parabolic as in [Harris and Fraser, 1976]) and turbulent flow in the upper airways. In order to compensate for uncertainties about fiber orientation, all such formulae are developed by assuming one or more of three cases of fiber orientation: the fiber axis is aligned, perpendicular, or randomly oriented with respect to the flow. Using these assumptions, deposition models can be constructed by taking into account airway geometry, flow conditions, and expected fiber orientation at different points along the particle's trajectory through the airway.

It should be noted that both experiments and analytical deposition estimates for long fibers show that their deposition efficiency in the lungs increases when the particle's shape has a large interception cross section [Timbrell, 1970; Harris Jr and Timbrell, 1975] and when fibers (even straight ones) are oriented randomly in an airway [Harris and Fraser, 1976; Asgharian and Yu, 1988; Balásházy et al., 1990].

[Timbrell, 1970] characterizes different shapes and size distributions for two types of asbestos fibers – curly chrysotile fibers resembling bundles of long thin fibrils and straight "needle-like" amphiboles. He also describes an experiment on two groups of rats, in which it is found that after 10 weeks exposure to dust clouds of the Union Internationale Contre le Cancer (UICC) reference fibers, six times more (by weight) amphiboles are recovered from animal's lungs than chrysotile particles. They repeated the experiment in vitro on a bundle of 100 tubes, 1 cm long and 400 μm inner diameter, with flow conditions comparable with the narrow lung airways and confirmed that an estimated five to six times as much needle-like fibers as curly fibers penetrated the bundle. This difference is explained by the smaller penetration efficiency of curly fibers through narrow tubes as compared with needle-like shape particles. Higher ratios of penetrated masses for amphiboles and chrysotiles have also been observed in experiments on hollow casts of pig and human lungs [Timbrell, 1970].

More recently, [Harris Jr and Timbrell, 1975] proposed a deposition model and mathematical estimates for three particles – a single straight rod, two attached straight rods, or three rods orthogonal to each other – all under an assumption of random orientation in the airway. Their idea is that a randomly oriented straight rod may behave in an airway like a particle of general shape, while the two other configurations represent aggregations of simple particles. Their mathematical formulation is based on adapting a mathematical model for straight fibers as described in [Harris and Fraser, 1976]. They compared the deposition of the three particles of interest with the deposition of single straight particles in an ordered tumbling motion. Their results predict differences in deposition efficiencies for particles aligned with the flow and for randomly oriented particles. They also found that increased interception cross section for particle aggregations and random orientation of single particles both decrease the probability of particle deposition in the peripheral lung airways, but increase deposition probabilities for the upper airways.

New noninvasive magnetic targeting method that relies on increasing local interception deposition have been presented in [Martin and Finlay, 2008b,a] and studied *in vivo* by [Redman et al., 2011]. The method is based on the result of [Jeffery, 1922] predicting that straight fiber particles will spend most of their time in the stream aligned with the fluid streamlines. This allows elongated high aspect ratio particles to reach the most distal lung airways, where their deposition can be enhanced by controlling their orientation in a way that benefits deposition due to interception. [Martin and Finlay, 2008b] have shown that the angular orientation of a high aspect ratio particle covered with magnetic nanoparticles can be controlled with an external source of magnetic field. The magnetic targeting method is successfully verified in an *in vitro* study [Martin and Finlay, 2008a] where deposition is enhanced by a factor of 1.7 under external magnetic field. Later, [Redman et al., 2011] completed an *in vivo* study confirming that the magnetic targeting approach is able to increase deposition in the middle and basal airways of the lung in rabbits. From these studies, this magnetic targeting technique shows promise, but the question of how deposition enhancement can be affected by various parameters has yet to be examined. In particular, in order to better understand the potential of this method there is a need to study the effect of fiber aspect ratio on the deposition efficiency in distal airways.

Given existing data that find that particle shape may strongly influence the deposition of inhaled fibers, interest in improving deposition models in the respiratory tract to rigorously predict deposition for particles of all shapes remains strong. In addition, asbestos fibers are still of major interest for environmental hygienists around the world. Recent developments

in nanotechnology have resulted in the proposed use of asymmetric fibers deformation to enhance targeting of deposition [Shang et al., 2008] and have also brought new concerns about the possible toxicity of recently created materials such as carbon nanotubes. But despite the obvious importance of fiber geometry in the prediction of deposition patterns in the lungs, except for [Asgharian and Ahmadi, 1998] and [Podgórski and Gradon, 1990], no attempts have been made in the literature to self-consistently address the dynamics of complex particles under flow conditions found in the lung airways either analytically or numerically.

In the following sections we will present work on direct numerical simulations of fiber dynamics taking into account the complexity of shapes appearing with real fibers. Unfortunately, it is not possible to provide numerical solution representative of all flow conditions present in the lungs. This is mainly because the flow there is essentially three-dimensional [Tsuda et al., 2002; Wall and Rabczuk, 2008]. In addition, there is a strong evidence of nonreversible mixing in all lung generations, even in the most distant ones [Tsuda et al., 2002; Sznitman, 2013]. Despite the factors mentioned above, the flow profile in the axial direction is usually reported as being close to Hagen—Poiseuille, skewed parabolic or M-shaped, depending on the Reynolds number [Balásházy et al., 1996; Nowak et al., 2003; Cebral and Summers, 2004; Zhang and Kleinstreuer, 2004; Wall and Rabczuk, 2008].

Computational efforts in the airways are especially complicated because of the significant differences in the length scales involved in any mathematical model for particle dynamics. Airway diameters range from 1.81 cm in the trachea to 240 μm in the terminal alveoli [Finlay et al., 2000]. At the same time, diameters of the most interesting particles, which have a better chance to penetrate into the distal airways are about 1 μm ($\sim 10^{-4}$ cm) and smaller. In order to accurately resolve particle motion, the size of the computational grid used in simulations should be determined from the smallest dimension of the fiber. For spherical particles, for example, the mesh is required to allow at least ten elements along a sphere diameter to produce sedimentation results close to experimental results [Veeramani et al., 2007]. On the other hand, such fine grids are not practical for simulations of the flow within airways. From our experience, low Reynolds number flow in the ducts can be adequately resolved on meshes with element sizes ten or even twenty times larger than required for particle simulations [Dechaume et al., 2010; Martinez et al., 2013]. We will address the issue of different length scales involved in our simulations with the Rotating Grid Procedure described in Section 3.2.

Using the Rotating Grid Procedure, we first show that even neglecting secondary flows and assuming an ideal parabolic flow profile in the airways, particle deposition may further

be enhanced by a nontrivial particle geometry. And in this simplified case, on top of the linear translation in the axial direction, actual high aspect ratio asbestos-like fibers in the human lungs are expected to have at least two components of rotation: in-plane rotation (tumbling in the plane containing a duct axis and the particles' center of mass, *i.e.*, in a plane with the unit normal parallel to the local vorticity) due to simple shear in a parabolic-like flow profile, and transverse rotation(secondary rotation orthogonal to the first one) due to irregular particle shape causing the fluid forces to be distributed nonuniformly over the particle surface; see Figure 3.1, Section 3.3.

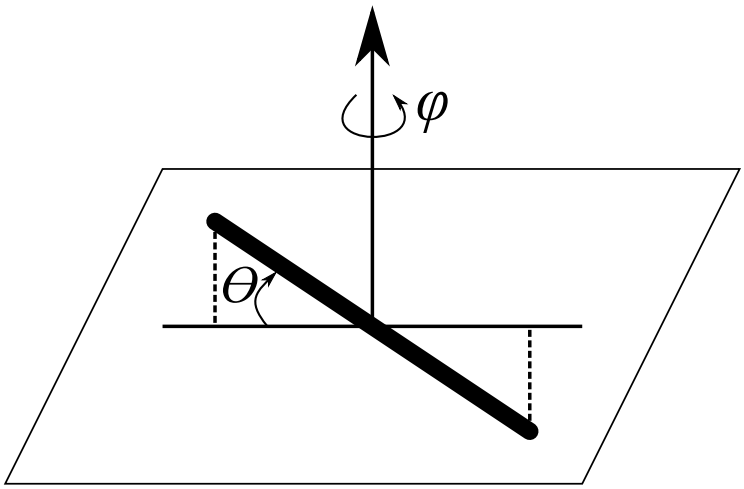

Figure 3.1: Two types of rotation: in-plane rotation angle φ and transverse rotation angle θ.

Second, we will study trajectories of long fibers in a small (distal) airway bifurcation model with fixed angular position of the particle. The deposition efficiency with and without magnetic field alignment will be presented and the effect of particle aspect ratio on the deposition enhancement will be quantified; see Section 3.4.

3.2 Numerical Method

3.2.1 Governing Equations

To examine the coupled motion of a rigid body fiber in a fluid, we directly solve the governing equations of motion for the fiber and surrounding fluid. Newton's second law supplies the equations for the velocity and angular velocity of the particle of an arbitrary shape, while the surrounding fluid motion is obtained by solving the Navier–Stokes equations.

The particle and fluid motions are coupled via surface forces and a no-slip boundary condition applied at the particle surface. The resulting set of nonlinear equations is solved numerically.

The equations of motion of the fluid are

$$\begin{aligned} \frac{\partial \boldsymbol{v}}{\partial t} + \boldsymbol{v}\cdot\boldsymbol{\nabla}\boldsymbol{v} &= -\boldsymbol{\nabla}p + \frac{1}{Re}\boldsymbol{\nabla}^2\boldsymbol{v} \qquad \text{in } \Omega_f, \\ \boldsymbol{\nabla}\cdot\boldsymbol{v} &= 0 \end{aligned} \tag{3.1}$$

with no-slip boundary condition $\boldsymbol{v} = \boldsymbol{U} + \boldsymbol{\omega}\times(\boldsymbol{x} - \boldsymbol{X})$ on the particle surface $\partial\Omega_p$ and Ω_f being the fluid domain, Figure 2.1. Here, $\boldsymbol{v}$ is the fluid velocity field, p is the fluid pressure, $Re = UL/\nu$ is the Reynolds number defined via the fluid kinematic viscosity ν, the characteristic length L, and the characteristic velocity U, and $\boldsymbol{x}$ is a point on the particle boundary; $\boldsymbol{U}$, $\boldsymbol{\omega}$, and $\boldsymbol{X}$ are respectively the particle centroid velocity, angular velocity, and center of mass position.

The particle motion is governed by the following equations:

$$\begin{aligned} \frac{d\boldsymbol{U}}{dt} &= \frac{\rho_r - 1}{\rho_r}\frac{1}{Fr}\boldsymbol{e}_g + \frac{1}{\rho_r V_p}\boldsymbol{F} \\ \frac{d(\mathbb{I}_p\boldsymbol{\omega})}{dt} &= \boldsymbol{T}, \qquad \frac{d\boldsymbol{\vartheta}}{dt} = \boldsymbol{\omega}, \qquad \frac{d\boldsymbol{X}}{dt} = \boldsymbol{U} \end{aligned} \tag{3.2}$$

where $\rho_r = \rho_{fiber}/\rho_{fluid}$ is the particle relative density, $Fr = U^2/gL$ is the Froude number with g being the gravity acceleration, $\boldsymbol{e}_g$ is the unit vector in the direction of gravity, V_p is the particle volume, $\mathbb{I}_p$ is the inertia tensor, $\boldsymbol{\vartheta}$ is the rotation vector (vector pointing along the rotation axis with modulus equal to the rotation angle), $\boldsymbol{F}$ is the total hydrodynamic force, and $\boldsymbol{T}$ is the torque acting on the particle surface.

3.2.2 Fictitious Domain Formulation

For our numerical method, we adopted the finite element formulation of the fictitious domain method, developed by [Diaz-Goano et al., 2003] and further extended by [Veeramani et al., 2007], in order to replace the use of Lagrange multipliers, when imposing the rigid boundary constraint, with the solution of an integral equation. See Chapter 2 for more detail.

The fictitious domain method reformulates the systems (3.1)–(3.2) by extending the

Navier—Stokes equations to the entire domain $\Omega = \Omega_f \cup \Omega_p$, Figure 2.1:

$$\begin{aligned} &\frac{D\boldsymbol{v}}{Dt} = -\boldsymbol{\nabla} p + \frac{1}{Re}\boldsymbol{\nabla}^2\boldsymbol{v} + (\rho_r - 1)(\boldsymbol{g} - \boldsymbol{\mathcal{F}}) \qquad \text{in } \Omega, \\ &\boldsymbol{\nabla}\cdot\boldsymbol{v} = 0 \qquad \text{in } \Omega, \end{aligned} \tag{3.3}$$

$$\begin{aligned} &\boldsymbol{v} = \boldsymbol{U} + \boldsymbol{\omega}\times(\boldsymbol{x} - \boldsymbol{X}) \qquad \text{in } \Omega_p, \\ &\frac{d\boldsymbol{\vartheta}}{dt} = \boldsymbol{\omega}, \qquad \frac{d\boldsymbol{X}}{dt} = \boldsymbol{U} \\ &\frac{d\boldsymbol{U}}{dt} = \frac{1}{V_p}\int\limits_{\Omega_p} \boldsymbol{\mathcal{F}}\, d\Omega, \quad \frac{d(\mathbb{I}_p\boldsymbol{\omega})}{dt} = \frac{1}{\rho_r}\int\limits_{\Omega_p} (\boldsymbol{x} - \boldsymbol{X})\times\frac{D\boldsymbol{v}}{Dt}\, d\Omega, \end{aligned} \tag{3.4}$$

where

$$\boldsymbol{g} = \begin{cases} \frac{1}{Fr}\boldsymbol{e}_g, & \text{in } \Omega_p, \\ 0, & \text{in } \Omega_f, \end{cases}$$

represents the gravity acting on the particle and

$$\boldsymbol{\mathcal{F}} = \begin{cases} \dfrac{1}{Fr}\boldsymbol{e}_g + \dfrac{1}{\rho_r - 1}\left(-\dfrac{D\boldsymbol{v}}{Dt} + \dfrac{1}{Re}\boldsymbol{\nabla}^2\boldsymbol{v} - \boldsymbol{\nabla} p\right), & \text{in } \Omega_p, \\ 0, & \text{in } \Omega_f, \end{cases} \tag{3.5}$$

represents the interaction force between the two phases.

3.2.3 Rotating Grid Procedure

In Chapter 2.6 we described a multi-scale approach for FDM simulations of the micro-particles in the large domains. The approach introduces two grids $\mathcal{G}_H$ and $\mathcal{G}_h$ with the grid sizes H and h respectively, such that $h \ll H$. The grid spacing on each grid is chosen to be appropriate for the accurate spatial resolution of the corresponding scale.

The notable feature of the method is that the micro-grid $\mathcal{G}_h$ is attached to the solid centre of mass $\boldsymbol{X}$ and follows particle in its motion. The particle is left free to rotate within the grid $\mathcal{G}_h$ around $\boldsymbol{X}$.

Such setup requires very fine meshing in the micro-grid everywhere where the particle may possibly appear during the simulations. And in the case of fibers experiencing intensive rotation, we, therefore, have to solve on a relatively large, significantly refined mesh. At the same time, for each angular position of the fiber, fine meshing is required only in some vicinity of the particle surface, while the rest of the grid, though being refined, does not

contribute much to the overall accuracy of the simulations.

For the Rotating Grid Procedure we propose to extend the two-grid approach in Chapter 2.6 by fixing the micro-grid $\mathcal{G}_h$ with respect to the particle in its spatial motion. This allows us to refine the computational mesh in the immediate vicinity of the particle, while leaving the rest of the grid $\mathcal{G}_h$ as fine as it is required for the accurate resolution of the local flow features. Additionally, fixing particle within the mesh allows exact fitting of the complex particle surface geometry with the elements in the computational mesh, which eliminates sub-meshing of intersected elements required for the accurate integration in (3.4), see Figure 3.2.

Since now the computational grid $\mathcal{G}_h$ is experiencing complex spatial rigid-body motion, we apply the ALE method, thus transforming the problem on the moving grid $\mathcal{G}_h(t)$ to the problem defined on a fixed grid $\mathcal{G}_h^0 = \mathcal{G}_h(0)$.

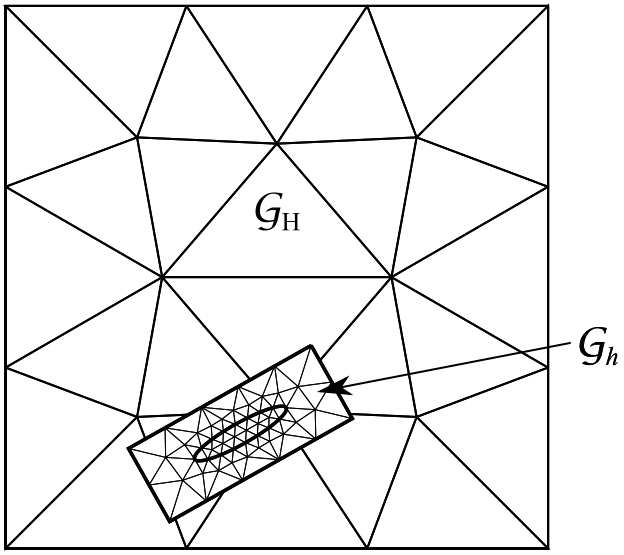

Figure 3.2: Schematic depiction of the Macro-grid $\mathcal{G}_H$ and the Micro-grid $\mathcal{G}_h$ for the Rotating Grid Procedure. Particle boundary in $\mathcal{G}_h$ can be seen fit by the discretization elements edges.

Arbitrary Lagrangian–Eulerian Transformation

Grid $\mathcal{G}_h$ is fixed around the particle and is advected and rotated together with it. The grid position and orientation at time t we denote $\mathcal{G}_h(t)$; similarly, the domain covered by $\mathcal{G}_h(t)$ we call $\Omega(t)$. We introduce two sub-domains of $\Omega(t) = \Omega_f \cup \Omega_p$, such that Ω_f is the fluid and Ω_p is the particle volumes. Relative positions of the sub-domains are fixed within $\Omega(t)$,

but they are moving through space according to the $\mathcal{G}_h(t)$ motion.

Location of a point $\boldsymbol{x}(t) \in \mathcal{G}_h(t)$ can be found from its initial position $\boldsymbol{x}(0)$ in the reference grid $\mathcal{G}_h^0 = \mathcal{G}_h(0)$ through $\boldsymbol{x}(t) = \boldsymbol{X}(t) + \mathbb{R}(t)(\boldsymbol{x}(0) - \boldsymbol{X}(0))$ where $\mathbb{R}(t)$ is a rotation matrix computed with the Rodriguez formula from the orientation vector $\boldsymbol{\vartheta}(t)$:

$$\mathbb{R} = cos(\vartheta)\mathbb{I} + sin(\vartheta)[\boldsymbol{\vartheta}^0]_\times + (1 - cos(\vartheta))\boldsymbol{\vartheta}^0 \otimes \boldsymbol{\vartheta}^0.$$

$$\boldsymbol{\vartheta}^0 \otimes \boldsymbol{\vartheta}^0 = \begin{bmatrix} \vartheta_x^{0\,2} & \vartheta_x^0\vartheta_y^0 & \vartheta_x^0\vartheta_z^0 \\ \vartheta_x^0\vartheta_y^0 & \vartheta_y^{0\,2} & \vartheta_y^0\vartheta_z^0 \\ \vartheta_x^0\vartheta_z^0 & \vartheta_y^0\vartheta_z^0 & \vartheta_z^{0\,2} \end{bmatrix} \quad [\boldsymbol{\vartheta}^0]_\times = \begin{bmatrix} 0 & -\vartheta_z^0 & \vartheta_y^0 \\ \vartheta_z^0 & 0 & -\vartheta_x^0 \\ -\vartheta_y^0 & \vartheta_x^0 & 0 \end{bmatrix}$$

Fixed reference grid $\mathcal{G}_h^0$ is a discretization of the fixed continuous domain Ω_r which we will refer to as the reference domain.

For simplicity, we assume that $\boldsymbol{X}(0) = 0$, therefore:

$$\hat{\boldsymbol{T}}(\boldsymbol{x}_r, t) = \boldsymbol{x}(\boldsymbol{x}_r, t) = \boldsymbol{X}(t) + \mathbb{R}(t)\boldsymbol{x}_r \tag{3.6}$$

is a linear transformation $\hat{\boldsymbol{T}} : \Omega_r \times \Im \rightarrow \Omega(t)$ with $\boldsymbol{x}_r \in \Omega_r$ being a point in the reference domain and $t \in \Im$ the time coordinate.

Now, for any scalar, $h(\boldsymbol{x}, t)$, or a vector, $\boldsymbol{h}(\boldsymbol{x}, t)$, function defined on $\Omega(t)$ we can define its counterpart $\hat{h}(\boldsymbol{x}_r, t) = h(\hat{\boldsymbol{T}}(\boldsymbol{x}_r, t), t)$ and $\hat{\boldsymbol{h}}(\boldsymbol{x}_r, t) = \boldsymbol{h}(\hat{\boldsymbol{T}}(\boldsymbol{x}_r, t), t)$ on the reference domain Ω_r. This way, the gradient of a function defined on the reference domain Ω_r can be found from the gradient of the corresponding function defined on $\Omega(t)$ as

$$\boldsymbol{\nabla}_r \hat{h} = \boldsymbol{\nabla} h \mathbb{F} \qquad \boldsymbol{\nabla}_r \hat{\boldsymbol{h}} = \boldsymbol{\nabla} \boldsymbol{h} \mathbb{F} \tag{3.7}$$

with

$$\mathbb{F} = \boldsymbol{\nabla}_r \hat{\boldsymbol{T}}(\boldsymbol{x}_r, t) = \mathbb{R}(t) \tag{3.8}$$

and the gradient defined as $(\boldsymbol{\nabla}\boldsymbol{h})_{ij} = \partial_j h_i$. From the properties of the rotational matrix and because the motion of $\mathcal{G}_h(t)$ is purely solid, it follows that $det\ \mathbb{F} = 1$. Here we use the following definitions:

$$(\boldsymbol{\nabla}\cdot\mathbb{A})_i = \sum_j \partial_j A_{ij} \qquad \boldsymbol{\nabla}\cdot\boldsymbol{h} = \sum_i \partial_i h_i \tag{3.9}$$

and

$$\boldsymbol{v}(\boldsymbol{x}, t) = d_t \boldsymbol{x}(\boldsymbol{x}_r, t) = \partial_t \boldsymbol{x} + \boldsymbol{\nabla}_r \boldsymbol{x}\ d_t \boldsymbol{x}_r = \partial_t \boldsymbol{x} \tag{3.10}$$

Note that, since the reference grid is fixed in time, $d_t \boldsymbol{x}_r = 0$. Partial derivatives in time and material derivatives are correspondingly given by

$$\partial_t h = \partial_t \hat{h} - (\mathbb{F}^{-1}\partial_t \hat{T}\cdot\boldsymbol{\nabla}_r)\hat{h} \qquad d_t h = \partial_t \hat{h} + (\mathbb{F}^{-1}(\hat{\boldsymbol{v}} - \partial_t \hat{T})\cdot\boldsymbol{\nabla}_r)\hat{h} \tag{3.11}$$

$$\partial_t \boldsymbol{h} = \partial_t \hat{\boldsymbol{h}} - (\mathbb{F}^{-1}\partial_t \hat{T}\cdot\boldsymbol{\nabla}_r)\hat{\boldsymbol{h}} \qquad d_t \boldsymbol{h} = \partial_t \hat{\boldsymbol{h}} + (\mathbb{F}^{-1}(\hat{\boldsymbol{v}} - \partial_t \hat{T})\cdot\boldsymbol{\nabla}_r)\hat{\boldsymbol{h}} \tag{3.12}$$

The Piola transform of a vector $\boldsymbol{h}$ is denoted by $\mathbb{F}^{-1}\hat{\boldsymbol{h}}$, and therefore its divergence is given by $\boldsymbol{\nabla}\cdot\boldsymbol{h} = \boldsymbol{\nabla}_r\cdot(\mathbb{F}^{-1}\hat{\boldsymbol{h}})$. Similarly, for a tensor $\boldsymbol{\sigma}$ the Piola transform reads $\hat{\boldsymbol{\sigma}}\mathbb{F}^{-T}$, and its divergence is $\boldsymbol{\nabla}\cdot\boldsymbol{\sigma} = \boldsymbol{\nabla}_r\cdot(\hat{\boldsymbol{\sigma}}\mathbb{F}^{-T})$.

Having in mind these relations, we can now reformulate the Navier–Stokes equations (3.3) in an Arbitrary Lagrangian-Eulerian framework:

$$\begin{aligned}
&\frac{\partial \hat{\boldsymbol{v}}}{\partial t} + (\mathbb{F}^{-1}(\hat{\boldsymbol{v}} - \hat{\boldsymbol{w}})\cdot\boldsymbol{\nabla}_r)\hat{\boldsymbol{v}} - \boldsymbol{\nabla}_r\cdot(\hat{\boldsymbol{\sigma}}\mathbb{F}^{-T}) = (\rho_r - 1)(\hat{\boldsymbol{g}} - \hat{\boldsymbol{\mathcal{F}}}) && \text{in } \Omega_r,\\
&\boldsymbol{\nabla}_r\cdot(\mathbb{F}^{-1}\hat{\boldsymbol{v}}) = 0 && \text{in } \Omega_r,\\
&\hat{\boldsymbol{\sigma}} = -\hat{p}\mathbb{I} + \frac{1}{Re}\boldsymbol{\nabla}_r\hat{\boldsymbol{v}}\mathbb{F}^{-1},
\end{aligned}$$

or

$$\begin{aligned}
&\frac{\partial \hat{\boldsymbol{v}}}{\partial t} + (\mathbb{F}^{-1}(\hat{\boldsymbol{v}} - \hat{\boldsymbol{w}})\cdot\boldsymbol{\nabla}_r)\hat{\boldsymbol{v}} = \\
&\qquad = -\mathbb{F}^{-T}\boldsymbol{\nabla}_r\hat{p} + \frac{1}{Re}\boldsymbol{\nabla}_r\cdot(\boldsymbol{\nabla}_r\hat{\boldsymbol{v}}\mathbb{F}^{-1}\mathbb{F}^{-T}) + (\rho_r - 1)(\hat{\boldsymbol{g}} - \hat{\boldsymbol{\mathcal{F}}}) \qquad \text{in } \Omega_r,\\
&\boldsymbol{\nabla}_r\cdot(\mathbb{F}^{-1}\hat{\boldsymbol{v}}) = 0 \quad \text{in } \Omega_r,
\end{aligned} \tag{3.13}$$

discretized on $\mathcal{G}_h^0$, and where

$$\hat{\boldsymbol{w}}(\boldsymbol{x}_r, t) = \partial_t \hat{\boldsymbol{T}}(\boldsymbol{x}_r, t) = \boldsymbol{U} + \boldsymbol{\omega}\times(\mathbb{R}\boldsymbol{x}_r) \tag{3.14}$$

is the velocity of points in $\mathcal{G}_h(t)$ as it moves together with the particle. Observe that $\mathbb{R}\boldsymbol{x}_r = \boldsymbol{x} - \boldsymbol{X}$.

In general, any numerical scheme implementing the ALE approach requires updating of the matrices before each time step. This is because the inverse of the deformation gradient tensor $\mathbb{F}^{-1}$ appears inside the convective derivative and divergence operators in equation (3.13). Such an update is very expensive from computational point of view and in 3–D imposes significant limitations on the attainable spatial resolution of the method.

Nevertheless, in the case of a very special grid deformation, like in our case of pure rigid-

body motion, updating the matrices can be completely avoided. First of all, the rotation matrix is an orthogonal matrix, so that:

$$\mathbb{R}^T = \mathbb{R}^{-1}. \tag{3.15}$$

We also use the following properties of the differential operators:

$$\boldsymbol{\nabla}(\mathbb{A}(t)\boldsymbol{h}(\boldsymbol{x},t)) = \mathbb{A}(t)\boldsymbol{\nabla}(\boldsymbol{h}(\boldsymbol{x},t)) \tag{3.16}$$

$$\boldsymbol{\nabla}\cdot(\mathbb{A}(t)\mathbb{B}(\boldsymbol{x},t)) = \mathbb{A}(t)\boldsymbol{\nabla}\cdot(\mathbb{B}(\boldsymbol{x},t)). \tag{3.17}$$

And finally, any vector can be rotated to have the same orientation with respect to the points in the reference grid as is its orientation with respect to the points in $\mathcal{G}_h(t)$:

$$\begin{aligned} \boldsymbol{v} = \hat{\boldsymbol{v}} = \mathbb{R}(t)\boldsymbol{v}_r \qquad & \boldsymbol{w} = \hat{\boldsymbol{w}} = \mathbb{R}(t)\boldsymbol{w}_r \\ \boldsymbol{g} = \hat{\boldsymbol{g}} = \mathbb{R}(t)\boldsymbol{g}_r \qquad & \boldsymbol{f} = \hat{\boldsymbol{f}} = \mathbb{R}(t)\boldsymbol{f}_r. \end{aligned} \tag{3.18}$$

Now, replacing $\mathbb{F}$ according to (3.8), and using identities (3.15)-(3.18), equations (3.13) are simplified to:

$$\begin{aligned} &\frac{\partial \hat{\boldsymbol{v}}}{\partial t} + ((\boldsymbol{v}_r - \boldsymbol{w}_r)\cdot\boldsymbol{\nabla}_r)\hat{\boldsymbol{v}} = \\ &\qquad = -\mathbb{R}\boldsymbol{\nabla}_r\hat{p} + \frac{1}{Re}\mathbb{R}\boldsymbol{\nabla}_r\cdot(\boldsymbol{\nabla}_r\boldsymbol{v}_r) + (\rho_r - 1)\mathbb{R}(\boldsymbol{g}_r - \boldsymbol{f}_r) \qquad \text{in } \Omega_r, \\ &\boldsymbol{\nabla}_r\cdot\boldsymbol{v}_r = 0 \quad \text{in } \Omega_r, \end{aligned} \tag{3.19}$$

Since solid dynamics is unsteady, the rotation matrix can not be simply factored out of the material derivative on the left hand side of (3.19).

Now, we can perform time-splitting of the convective terms from the generalized Stokes problem as explained in [Minev and Ross Ethier, 1998]. In this approach, the material derivative on the left hand side of (3.19) is approximated with second order splitting as

$$\frac{\partial \hat{\boldsymbol{v}}^{n+1}}{\partial t} + ((\boldsymbol{v}_r^{n+1} - \boldsymbol{w}_r^{n+1})\cdot\boldsymbol{\nabla}_r)\hat{\boldsymbol{v}}^{n+1} \approx \frac{3\hat{\boldsymbol{v}}^{n+1} - 4\tilde{\hat{\boldsymbol{v}}}^{n} + \tilde{\hat{\boldsymbol{v}}}^{n-1}}{2\Delta t}. \tag{3.20}$$

Here,

$$\tilde{\hat{\boldsymbol{v}}}^{n}(\boldsymbol{x}_r) = \hat{\boldsymbol{v}}(\boldsymbol{Z}(t^n;\boldsymbol{x}_r),t^n) \qquad \tilde{\hat{\boldsymbol{v}}}^{n-1}(\boldsymbol{x}_r) = \hat{\boldsymbol{v}}(\boldsymbol{Z}(t^{n-1};\boldsymbol{x}_r),t^{n-1}) \tag{3.21}$$

are the velocities from time levels n and $n-1$, which have been advected alongside of an approximation to the characteristics, with $\boldsymbol{Z}(t^n;\boldsymbol{x}_r)$ and $\boldsymbol{Z}(t^{n-1};\boldsymbol{x}_r)$ being the solution to

the following terminal-value problem for pure advection equation between t^{n-1} and t^{n+1}:

$$\begin{cases} \dfrac{d\boldsymbol{Z}(s)}{ds} = \boldsymbol{v}_r(\boldsymbol{Z}(s), s) - \boldsymbol{w}_r(\boldsymbol{Z}(s), s), \\ \boldsymbol{Z}(t^{n+1}) = \boldsymbol{x}_r, \quad \boldsymbol{x}_r \in \mathcal{G}_h^0, \quad s \in [t^{n-1}, t^{n+1}]. \end{cases} \tag{3.22}$$

It should be noted here that even though the advected velocities $\tilde{\hat{\boldsymbol{v}}}^n(\boldsymbol{x}_r)$ and $\tilde{\hat{\boldsymbol{v}}}^{n-1}(\boldsymbol{x}_r)$ are defined in the laboratory frame of reference, they are advected on the reference grid $\mathcal{G}_h^0$ alongside characteristics defined through velocities rotated according to transformation (3.18).

Using (3.20) and transformations $\tilde{\hat{\boldsymbol{v}}}^n = \mathbb{R}(t^{n+1})\tilde{\boldsymbol{v}}_r^n$, $\tilde{\hat{\boldsymbol{v}}}^{n-1} = \mathbb{R}(t^{n+1})\tilde{\boldsymbol{v}}_r^{n-1}$, equation (3.19) becomes

$$\begin{aligned} \mathbb{R}^{n+1}\frac{3\boldsymbol{v}_r^{n+1} - 4\tilde{\boldsymbol{v}}_r^n + \tilde{\boldsymbol{v}}_r^{n-1}}{2\Delta t} = \\ = -\mathbb{R}^{n+1}\boldsymbol{\nabla}_r\hat{p}^{n+1} + \frac{1}{Re}\mathbb{R}^{n+1}\boldsymbol{\nabla}_r{\cdot}(\boldsymbol{\nabla}_r\boldsymbol{v}_r^{n+1}) + \\ + (\rho_r - 1)\mathbb{R}^{n+1}(\boldsymbol{g}_r^{n+1} - \boldsymbol{f}_r^{n+1}) \qquad \text{in } \Omega_r, \\ \boldsymbol{\nabla}_r{\cdot}\boldsymbol{v}_r^{n+1} = 0 \quad \text{in } \Omega_r, \end{aligned} \tag{3.23}$$

Since $\mathbb{R}$ is nonsingular, equation (3.3) in an Arbitrary Lagrangian-Eulerian framework with fixed reference domain Ω_r and mapping $\hat{\boldsymbol{T}}(\boldsymbol{x}_r, t)$ finally takes the form of the generalized Stokes problem

$$\begin{aligned} \frac{3\boldsymbol{v}_r^{n+1} - 4\tilde{\boldsymbol{v}}_r^n + \tilde{\boldsymbol{v}}_r^{n-1}}{2\Delta t} = \\ = -\boldsymbol{\nabla}_r\hat{p}^{n+1} + \frac{1}{Re}\boldsymbol{\nabla}_r^2\boldsymbol{v}_r^{n+1} + (\rho_r - 1)(\boldsymbol{g}_r^{n+1} - \boldsymbol{f}_r^{n+1}) \qquad \text{in } \Omega_r, \\ \boldsymbol{\nabla}_r{\cdot}\boldsymbol{v}_r^{n+1} = 0 \quad \text{in } \Omega_r. \end{aligned} \tag{3.24}$$

Using finite elements for spatial discretization on $\mathcal{G}_h^0$, the above formulation produces matrices independent of time and can be precomputed at the beginning of time-stepping. Here, the pressure $\hat{p}$ serves as a Lagrange multiplier which enforces the incompressibility constraints $\boldsymbol{\nabla}_r{\cdot}\boldsymbol{v}_r^{n+1} = 0$ as well as $\boldsymbol{\nabla}{\cdot}\hat{\boldsymbol{v}}^{n+1} = 0$ in equation (3.13).

Algorithm Description

The detailed description of our procedure can be divided into the following sub-steps:

1. Find solution on macro-grid

Resolve the Navier-Stokes equations

$$\frac{\partial \boldsymbol{v}_H}{\partial t} + \boldsymbol{v}_H \cdot \boldsymbol{\nabla} \boldsymbol{v}_H = -\boldsymbol{\nabla} p_H + \frac{1}{Re_H} \boldsymbol{\nabla}^2 \boldsymbol{v}_H, \quad \boldsymbol{\nabla} \cdot \boldsymbol{v}_H = 0, \tag{3.25}$$

in the entire computational domain discretized with the macro-grid $\mathcal{G}_H$, where $p_H,\ \boldsymbol{v}_H$ being the fluid pressure and velocity and $Re_H = U_H L_H/\nu$ is the Reynolds number defined using the characteristic length and characteristic velocity appropriate for the macro-scale flow. Since the length scale of the solid is assumed to be much smaller than the length scale on $\mathcal{G}_H$, flow on the macro-grid does not "feel" the presence of the particle.

2. Predict particle position and orientation

The position and orientation of the particle at time step t^{n+1} are predicted explicitly by

$$\boldsymbol{X}^p = \boldsymbol{X}^{n-1} + 2\Delta t \boldsymbol{U}^n \qquad \boldsymbol{\vartheta}^p = \boldsymbol{\vartheta}^{n-1} + 2\Delta t \boldsymbol{\omega}^n \tag{3.26}$$

where Δt is the time step. This also defines the predicted transformation $\hat{\boldsymbol{T}}^p$ from the reference grid $\mathcal{G}_h^0$ to the predicted micro-grid position $\mathcal{G}_h^p$.

3. Transfer macro-grid velocity as a boundary condition on micro-grid

Use the resulting velocity field on $\mathcal{G}_H$ to interpolate Dirichlet boundary conditions at $\partial\mathcal{G}_h^p$ boundary of $\mathcal{G}_h^p$. The interpolation can be performed with regular $\mathbb{P}_2$ basis functions. Zero velocity is prescribed on boundary nodes when they appear outside of the computational grid $\mathcal{G}_H$ as a result of particle motion.

4. Impose zero flux through micro–grid surface

In general, the interpolated velocity $\hat{\boldsymbol{v}}_H$ on $\partial\mathcal{G}_h^p$ produces non-zero flux through the surface. Therefore, we correct its normal component solving the simple Lagrange multiplier problem

$$\begin{aligned} \boldsymbol{v}_{\partial\Omega} \cdot \boldsymbol{n} &= \hat{\boldsymbol{v}}_H \cdot \boldsymbol{n} + \hat{\boldsymbol{\lambda}} \qquad on\ \partial\Omega^p \\ \int_{\partial\Omega^p} \boldsymbol{v}_{\partial\Omega} \cdot \boldsymbol{n}\, dS &= 0, \end{aligned} \tag{3.27}$$

discretized on the micro-grid boundary $\partial\mathcal{G}_h^p$ the discrete version of the continuous boundary $\partial\Omega^p$.

5. Advection-Diffusion sub-step

Solve for $\boldsymbol{v}_r^*(\boldsymbol{x}_r)$ from

$$\begin{aligned} &\tau_0 \boldsymbol{v}_r^* - \frac{1}{Re}\boldsymbol{\nabla}_r^2 \boldsymbol{v}_r^* = -\tau_1 \tilde{\boldsymbol{v}}_r^n - \tau_2 \tilde{\boldsymbol{v}}_r^{n-1} - \boldsymbol{\nabla}_r \hat{p}^n + (\rho_r - 1)\boldsymbol{g}_r^p \qquad \text{in } \Omega_r, \\ &\mathbb{R}^p \boldsymbol{v}_r^* = \hat{\boldsymbol{v}}_{\partial\Omega} \qquad \textit{on } \partial\Omega_r \end{aligned} \tag{3.28}$$

discretized on $\mathcal{G}_h^0$, where $\tau_0 = 3/(2\Delta t)$, $\tau_1 = -2/\Delta t$ and $\tau_2 = 1/(2\Delta t)$.

6. Projection sub-step

Project the approximation $\boldsymbol{v}_r^*(\boldsymbol{x}_r)$ onto solenoidal subspace in order to impose incompressibility:

$$\tau_0(\boldsymbol{v}_r^{**} - \boldsymbol{v}_r^*) = -\boldsymbol{\nabla}_r(\hat{p}^{n+1} - \hat{p}^n) \qquad \text{in } \Omega_r \tag{3.29}$$

$$\boldsymbol{\nabla}_r \cdot \boldsymbol{v}_r^{**} = 0 \qquad \text{in } \Omega_r \tag{3.30}$$

$$(\boldsymbol{v}_r^{**} - \boldsymbol{v}_r^*) \cdot \boldsymbol{n} = 0 \qquad \textit{on } \partial\Omega_r \tag{3.31}$$

where $\boldsymbol{n}$ is the outward normal to $\partial\Omega_r$.

7. Rigid Body Constraint

The rigid body velocity is first predicted by integrating rotated fluid acceleration

$$\mathbb{R}^{-1}\left(\frac{D\boldsymbol{v}}{Dt}\right)^{n+1} = \tau_0 \boldsymbol{v}_r^{**} + \tau_1 \tilde{\boldsymbol{v}}_r^n + \tau_2 \tilde{\boldsymbol{v}}_r^{n-1} \tag{3.32}$$

within the particle volume on the reference grid:

$$\tau_0 \boldsymbol{U}_r^p + \mathbb{R}^{-1}(\tau_1 \boldsymbol{U}^n + \tau_2 \boldsymbol{U}^{n-1}) = \frac{1}{V_p}\int_{\Omega_p^r} \mathbb{R}^{-1}\left(\frac{D\boldsymbol{v}}{Dt}\right)^{n+1} d\Omega. \tag{3.33}$$

Then, we rotate all vector fields back using (3.18) and eliminate the Lagrange multiplier $\boldsymbol{\mathcal{F}}$ from the set of equations, which yields the end-of-step centroidal and angular velocities:

$$\boldsymbol{U}^{n+1} = \frac{1}{\rho_r V_p}\int_{\Omega_p^p} \boldsymbol{v}^{**}\, d\Omega + \frac{\rho_r - 1}{\rho_r}\boldsymbol{U}^p, \tag{3.34}$$

$$\boldsymbol{\omega}^{n+1} = \frac{(\mathbb{I}_p^p)^{-1}}{\tau_0}\left(\frac{1}{\rho_r}\int\limits_{\Omega_p^p}(\boldsymbol{x}^{n+1}-\boldsymbol{X}^p)\times\left(\frac{D\boldsymbol{v}}{Dt}\right)^{n+1} d\Omega - \right. \\ \left. - \tau_1(\mathbb{I}_p\boldsymbol{\omega})^n - \tau_2(\mathbb{I}_p\boldsymbol{\omega})^{n-1}\right), \tag{3.35}$$

where $\mathbb{I}_p^p$ is the predicted inertia tensor. Finally, we have the end-of-step solution for the fluid velocity:

$$\boldsymbol{v}^{n+1}(\boldsymbol{x}) = \begin{cases} \boldsymbol{v}^{**}(\boldsymbol{x}), & if\ (\hat{\boldsymbol{T}}^p)^{-1}(\boldsymbol{x},t) \in \Omega_r^f, \\ \boldsymbol{U}^{n+1} + \boldsymbol{\omega}^{n+1}\times(\boldsymbol{x}-\boldsymbol{X}^p), & if\ (\hat{\boldsymbol{T}}^p)^{-1}(\boldsymbol{x},t) \in \Omega_r^p, \end{cases} \tag{3.36}$$

which could be imposed pointwise or in the L^2 sense. The position and orientation of the particle are corrected using

$$\boldsymbol{X}^{n+1} = \boldsymbol{X}^n + \frac{\Delta t}{2}(\boldsymbol{U}^{n+1}+\boldsymbol{U}^n), \qquad \boldsymbol{\vartheta}^{n+1} = \boldsymbol{\vartheta}^n + \frac{\Delta t}{2}(\boldsymbol{\omega}^{n+1}+\boldsymbol{\omega}^n) \tag{3.37}$$

8. Next iteration

Go to step 1, in order to perform another time-step iteration.

The spatial discretizations $\mathcal{G}_H$ and $\mathcal{G}_h$ employ $\mathbb{P}_2 - \mathbb{P}_1$ tetrahedral finite elements generated with Gmsh software [Geuzaine and Remacle, 2009] and the resulting linear systems are solved using a conjugate gradient solver.

3.3 Fibers in a Linear Shear Flow

3.3.1 Problem Formulation

Motivation for Linear Flow Profile

Owing to large differences in scales between aerosol particles and airway flow, it is useful to neglect the local curvature of the parabolic-like flow profile in the vicinity of the particle, thus reducing the local flow to a simple two-dimensional linear shear flow.

We can investigate the difference between a local linear velocity profile and a parabolic velocity profile of the Hagen-Poiseuille flow in the vicinity of an aerosol particle.

Let the velocity with respect to the particle centroid be given as $V = V_{max}(1 - r^2/R^2) - V_C$, where V_{max} is the maximum velocity, r is the radial position, R is the pipe radius, and V_C is the particle centroid velocity. The slope of the linear approximation at each particle centroid position r_C is given by

$$\gamma = \left.\frac{\partial V}{\partial r}\right|_{r=r_C} = -V_{max}\frac{2r_C}{R^2}.$$

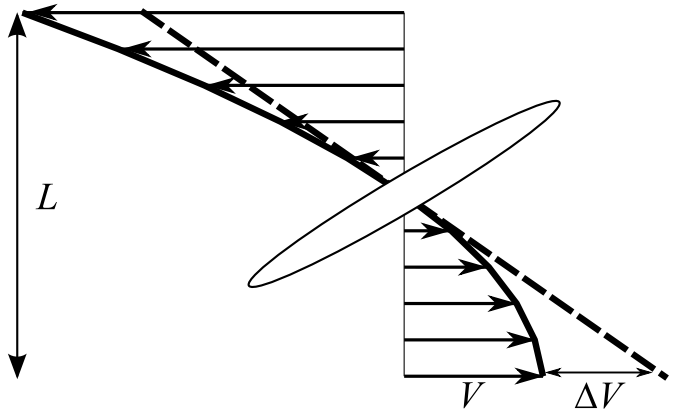

Figure 3.3: Sketch of the local velocity flow field with respect to the particle centroid in parabolic flow. Parabolic profile (solid line) and idealized linear profile (dashed line).

Let L be the particle length. We can evaluate the difference between the two profiles by calculating the maximum relative difference of the two velocities, $\Delta V/V$, at the distance $L/2$ from the particle centroid Figure 3.3. We plotted this error versus the relative radial location r_C/R for the fifth, tenth, and fifteenth lung generations' flow parameters and particle lengths, L, 20 and 40 μm Figure 3.4. It is seen that a local linear shear flow is a good approximation for the flow in the particle vicinity over many regions in the airways.

We should note though, that such an approximation of a local linear shear flow in the lungs is only valid starting distal to the first few lung generations where initially turbulent flow entering from the extra–thoracic airways and the trachea has relaminized.

Particle Shapes

A number of simulations are performed with particles of different densities, geometries, and aspect ratios immersed in a linear shear flow with velocity oriented in the Y direction and

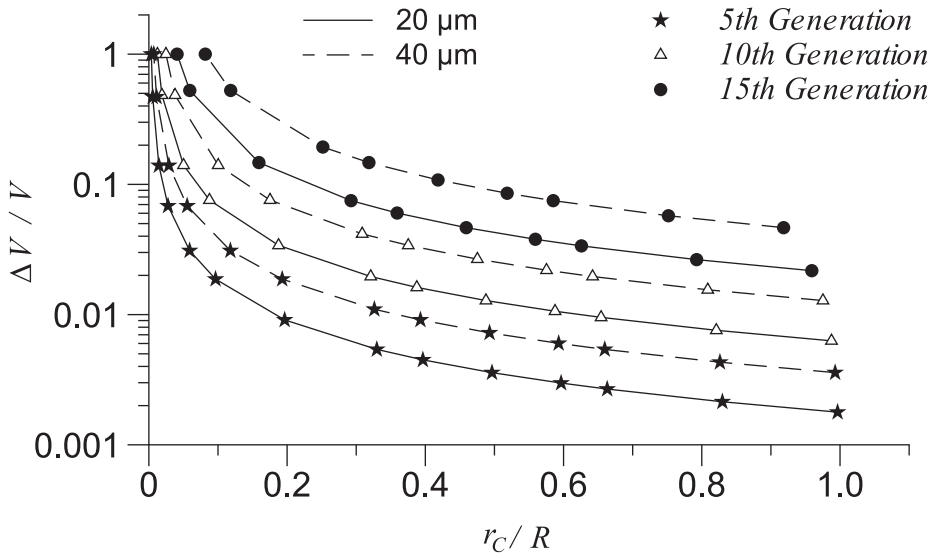

Figure 3.4: Maximum relative error (logarithmic scale) in velocity between parabolic flow and linear approximation based on the [Finlay et al., 2000] lung model with an inhalation flow rate of 18 $litres/min$.

velocity magnitude γX, where (X, Y, Z) is the inertial (laboratory) frame of reference and γ is a dimensional rate of shear. Fibers are defined by their diameter (which is kept constant for all simulations at $d_f = 2$ μm), aspect ratio a_r (the ratio of the particles' length to the particles' smallest diameter, which for most simulations is $a_r = 10$), shape, and relative density ρ_r (which is either 1 for neutrally buoyant particles or 1000 for heavy fibers). The following particle shapes are used in our simulations defined in a local coordinate system (x, y, z) fixed with the particle such that the fiber length is along x:

- **a.** Prolate ellipsoids with axes $(a_r d_f, d_f, d_f)$, with $a_r = 5$ and $a_r = 10$ are used for algorithm testing and verification;
- **b.** Cylinder of length $a_r d_f$, $a_r = 10$ with a circular cross section of diameter d_f (Figure 3.5);
- **c.** Cylinder of length $a_r d_f$, $a_r = 10$ with an elliptical cross section with axes $d_f \times 1.3 d_f$;
- **d.** Ring torus segment with the length to diameter ratio $a_r = 10$ and torus radius $R_T = \frac{180 a_r d_f}{40\pi}$ (Figure 3.6);
- **e.** Twisted cylinder with an elliptical cross section having ends parallel but rotated to each other by 45°. Particle length $a_r d_f$, $a_r = 10$, cross section axes $d_f \times 1.3 d_f$ (Figure 3.7);
- **f.** Particle from case (**e.**) bent from both ends by 10° (Figure 3.8);

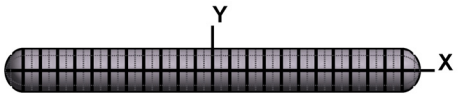

Figure 3.5: Particle (b).

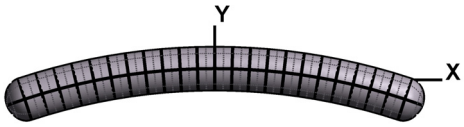

Figure 3.6: Particle (d).

Figure 3.7: Particle (e).

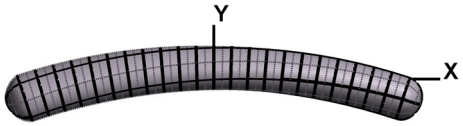

Figure 3.8: Particle (f).

g. Helical (spring) shape with a circular cross section of diameter d_f, the total length in the x direction is $a_r d_f$, and the centerline equation is $x = Vt,\ y = a\cos(t),\ z = b\sin(t)$, with parameters: $a_r = 15,\ a = b = d_f/2,\ V = a_r d_f/2\pi$, and $t \in [0,\ 2\pi]$ (Figure 3.9);

h. Helical (spring) shape with a circular cross section of diameter d_f, the total length in the x direction is $a_r d_f$, and the centerline equation is $x = Vt,\ y = a\cos(t),\ z = b\sin(t)$, with parameters: $a_r = 20,\ a = b = 2.15d_f,\ V = 2a_r d_f/5\pi$, and $t \in [0,\ 2\pi + \pi/2]$ (Figure 3.10), and

i. Conical spring with an elliptical cross section. The major axis of the cross section has a length of $1.3d_f$ and is aligned with the normal direction to the centerline; the minor axis has a length of d_f and is aligned with the binormal direction to the centerline. The total particle length is $a_r d_f$ and the centerline equation is $x = Vt,\ y = a(\frac{t}{2.5\pi})\cos(t + \frac{\pi}{4}),\ z = b(\frac{t}{2.5\pi})\sin(t + \frac{\pi}{4}))$, where $a_r = 20,\ a = b = 2.15d_f$, $V = 2a_r d_f/5\pi$, and $t \in [0, 2\pi + \pi/2]$ (Figure 3.11).

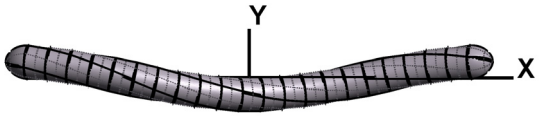

Figure 3.9: Particle (g).

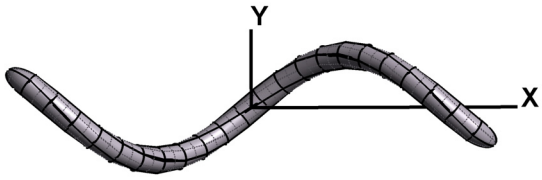

Figure 3.10: Particle (h).

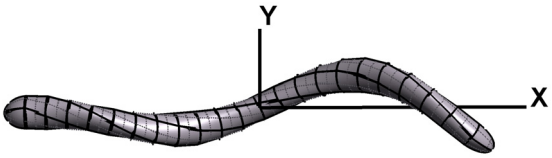

Figure 3.11: Particle (i).

In Table 3.1 we present inertia tensors for particles used in our simulations. Tensors are given with respect to the local coordinate system $(x,\ y,\ z)$ fixed with the particle. If the fiber centroid by construction happens to be away from the origin, we would bring the origin to the centroid position before calculating an inertia tensor.

$\mathbb{I}_{(a)} = m(d_f)(\frac{d_f}{2})^2 \begin{pmatrix} 0.4 & 0 & 0 \\ & 20.2 & 0 \\ & & 20.2 \end{pmatrix}$	$\mathbb{I}_{(b)} = m(d_f)(\frac{d_f}{2})^2 \begin{pmatrix} 0.49365 & -2{\cdot}10^{-7} & 4{\cdot}10^{-8} \\ & 31.5679 & 10^{-8} \\ & & 31.5679 \end{pmatrix}$
$\mathrm{Vol}_{(a)} = \frac{4}{3}\pi a_r(\frac{d_f}{2})^3$	$\mathrm{Vol}_{(b)} = 60.86(\frac{d_f}{2})^3$
$\mathbb{I}_{(c)} = m(d_f)(\frac{d_f}{2})^2 \begin{pmatrix} 0.664 & -3{\cdot}10^{-5} & -6{\cdot}10^{-5} \\ & 31.734 & -5{\cdot}10^{-7} \\ & & 31.5637 \end{pmatrix}$	$\mathbb{I}_{(d)} = m(d_f)(\frac{d_f}{2})^2 \begin{pmatrix} 0.72 & 2.5{\cdot}10^{-7} & 1.5{\cdot}10^{-5} \\ & 30.802 & -3{\cdot}10^{-6} \\ & & 31.0286 \end{pmatrix}$
$\mathrm{Vol}_{(c)} = 79.11(\frac{d_f}{2})^3$	$\mathrm{Vol}_{(d)} = 60.7667(\frac{d_f}{2})^3$
$\mathbb{I}_{(e)} = m(d_f)(\frac{d_f}{2})^2 \begin{pmatrix} 0.664 & -4{\cdot}10^{-5} & 5{\cdot}10^{-5} \\ & 31.7 & 0.05606 \\ & & 31.5991 \end{pmatrix}$	$\mathbb{I}_{(f)} = m(d_f)(\frac{d_f}{2})^2 \begin{pmatrix} 0.8888 & 0.0099 & -0.00944 \\ & 30.9478 & 0.05512 \\ & & 31.0686 \end{pmatrix}$
$\mathrm{Vol}_{(e)} = 79.1(\frac{d_f}{2})^3$	$\mathrm{Vol}_{(f)} = 79.0(\frac{d_f}{2})^3$
$\mathbb{I}_{(g)} = m(d_f)(\frac{d_f}{2})^2 \begin{pmatrix} 1.484 & 1.2{\cdot}10^{-5} & 4.91537 \\ & 71.1384 & -8{\cdot}10^{-7} \\ & & 71.1034 \end{pmatrix}$	$\mathbb{I}_{(h)} = m(d_f)(\frac{d_f}{2})^2 \begin{pmatrix} 18.2442 & -13.671 & -3{\cdot}10^{-6} \\ & 135.251 & 3{\cdot}10^{-8} \\ & & 133.411 \end{pmatrix}$
$\mathrm{Vol}_{(g)} = 92.05(\frac{d_f}{2})^3$	$\mathrm{Vol}_{(h)} = 156.115(\frac{d_f}{2})^3$
$\mathbb{I}_{(i)} = m(d_f)(\frac{d_f}{2})^2 \begin{pmatrix} 6.8 & -6.4743 & -11.241 \\ & 130.21 & 0.101 \\ & & 128.897 \end{pmatrix}$	$\mathrm{Vol}_{(i)} = 171.438(\frac{d_f}{2})^3$

Table 3.1: Inertia tensors and particle volumes as functions of fiber diameter d_f and particle mass m.

At $t = 0$, the particles are aligned with the X-axis (*i.e.*, perpendicular to the flow direction), which in terms of the Euler angles defined in Figure 3.12 implies the initial orientations $\alpha_0 = \pi/2$ and $\varphi_0 = \pi/2$, the centers of mass are placed at the center of rotation, and the initial angular velocities are set to $\frac{d\varphi}{dt}\big|_{t=0} = 0.9$, which is close to the expected angular velocity at this angular position based on [Jeffery, 1922]. The fluid motion in the micro-scale domain is characterized by the shear Reynolds number $Re_s = \gamma d_e^2/\nu$, where γ is a dimensional shear rate, $d_e = \sqrt[3]{10}d_f$ is an equivalent volume diameter for an ellipsoid with $a_r = 10$, and ν is the kinematic viscosity.

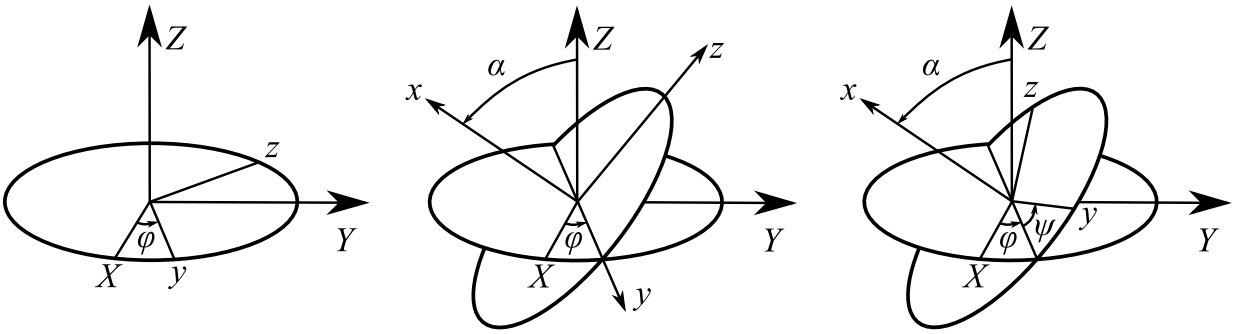

Figure 3.12: Euler angles defined through three rotations of (x, y, z) coordinate system.

All simulations are performed for a nondimensional shear rate equal to one; the shear plane is coincident with the $X - Y$ plane, the center of rotation is placed at the origin, and the flow velocity is parallel to the Y-axis. The macro-grid is a cube with edges long enough to encompass the micro-grid. Linear shear flow velocity profile on the macro-grid is prescribed analytically at each node. Since our main interest is in the rotational behavior associated with shear in the respiratory system, we neglect gravitational and diffusional effects on the fibers.

3.3.2 Results

Validation

The known analytical solution for a neutrally buoyant prolate ellipsoid [Jeffery, 1922] is used to test the ability of the numerical scheme to resolve complex particle rotation in a linear shear flow. A simulation for an ellipsoid with $a_r = 10$ is performed for $Re_s = 10^{-15}$ and we use the following initial conditions in terms of the Euler angles defined in Figure 3.12:

$$\alpha_0 = \frac{\pi}{4},\ \varphi_0 = 0,\ \text{and}\ \left.\frac{d\alpha}{dt}\right|_{t=0} = \left.\frac{d\varphi}{dt}\right|_{t=0} = 0. \tag{3.38}$$

Computational results for the time–dependent behavior of the Euler angles $\alpha(t)$ and $\varphi(t)$ for times up to $t = 100$ (here and subsequently t is a nondimensional time scaled with γ, *i.e.*,

$$t = t'\gamma \tag{3.39}$$

where $\gamma = Re_s(\nu/d_e^2)$ and t' is a dimensional time) are visually indistinguishable from the analytical solution, as seen in Figure 3.13.

For heavy particles, we compared our numerical solution with the results of [Asgharian

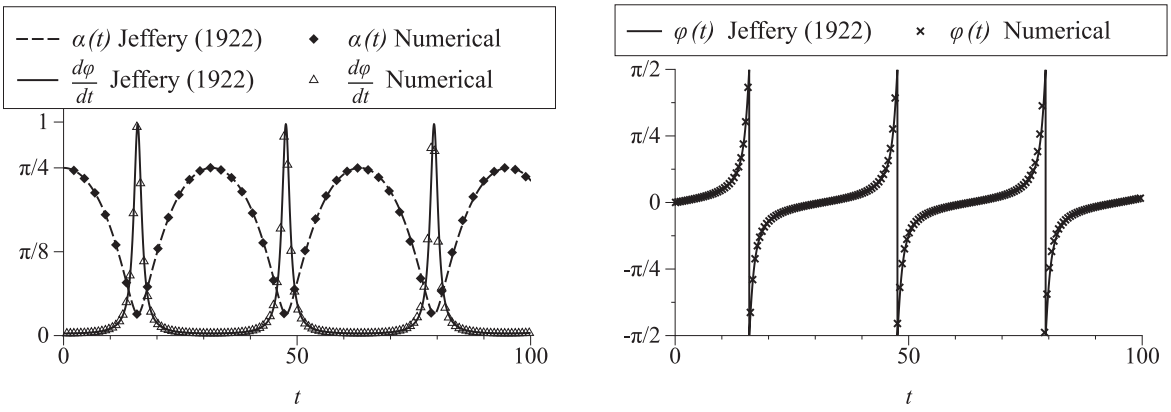

Figure 3.13: Analytical and numerical solutions for Euler angles $\alpha(t)$ (left) and $\varphi(t)$ (right) and angular velocity $\frac{d\varphi}{dt}$ (left) for a neutrally buoyant ellipsoid with $a_r = 10$.

and Anjilvel, 1995]. We found that our computed periods of tumbling (angle $\varphi(t)$; Figure 3.12) for prolate ellipsoids rotating in the shear plane are in close agreement for small Re_s. [Asgharian and Anjilvel, 1995] found that the heavy ellipsoid behavior in a linear shear flow depends on the particle aspect ratio and nondimensional parameter

$$\Re = \frac{\rho_{fiber}\gamma d_f^2}{\mu},$$

which is related to our shear Reynolds number through the relation

$$\Re = \frac{\rho_r Re_s}{\sqrt[3]{100}}.$$

We performed a series of simulations for ellipsoids with $a_r = 10$ and $a_r = 5$ in the shear plane, keeping $\Re$ constant but varying the relative density and the shear Reynolds number. The results of these simulations are presented in Table 3.2.

$a_r = 5,\ \Re = 0.63$		$a_r = 10,\ \Re = 0.43$	
Fluid parameters	T	Fluid parameters	T
[Jeffery, 1922]	32.67	[Jeffery, 1922]	63.46
[Asgharian and Anjilvel, 1995]	~ 32	[Asgharian and Anjilvel, 1995]	~ 63
$Re_s = 0.002924,\ \rho_r = 1000$	35.2	$Re_s = 0.002,\ \rho_r = 1000$	67.8
$Re_s = 0.1,\ \rho_r = 29.24$	42	$Re_s = 0.1,\ \rho_r = 20$	87.2
$Re_s = 2.924,\ \rho_r = 1$	∞	$Re_s = 2,\ \rho_r = 1$	∞

Table 3.2: Periods of rotation for high aspect ratio ellipsoids under different initial parameters

As Re_s is increased and ρ_r is decreased, we observed an increase in the period of tumbling T up to the point $\rho_r = 1$, where the particle ceases to rotate and becomes aligned with the flow. Such an alignment for neutrally buoyant ellipsoids is actually predicted by [Subramanian and Koch, 2005], in which they derived a critical Reynolds number $Re_c = \frac{15}{4\pi}\frac{\ln a_r}{a_r}$ above which particles would always align with the flow direction. For higher shear Reynolds numbers, discrepancies in the periods of rotation, T, between our simulations and the results of [Jeffery, 1922] and [Asgharian and Anjilvel, 1995] (see Table 3.2) can be a result of hydrodynamic and inertial effects that do not arise for smaller Re_s, which are closer to the assumption of very small Reynolds number used in derivations of analytical expressions by [Jeffery, 1922] and [Asgharian and Anjilvel, 1995]; in addition, [Jeffery, 1922] assumes a neutrally buoyant ellipsoid.

Numerical experiments with complex fiber shapes

Having validated our code as demonstrated above, we performed simulations for fluid-particle parameters representative of fiber behavior in the human respiratory tract. In particular, we set $Re_s = 24{\cdot}10^{-5}$, which approximates the value of shear Reynolds number for the first seventeen lung generations (based on the idealized lung geometry of [Finlay et al., 2000] for an inhalation flow rate of 18 $litres/min$) with $\rho_r = 1000$ (heavy) and $\rho_r = 1$ (neutrally buoyant) solid particles. An important finding in what follows involves the particle inclination angle to the shear plane, *i.e.*, the out of (shear) plane angle, which we denote as

$$\theta = \frac{\pi}{2} - \alpha \tag{3.40}$$

(Figure 3.14) and which is the angle the particle makes with the $X - Y$ plane when it rotates. At $t = 0$, all particles are oriented parallel to the shear plane ($\theta = 0$).With such initial orientation, Jeffery motion has $\theta = 0$ for all time.

We first consider particles derived by bending and twisting cylinders of circular and elliptical cross sections, *i.e.*, particles (**b**)–(**f**). We notice that in all our simulations, heavy and neutrally buoyant particles expressed either nearly identical or at least very similar behavior. Therefore, here we only describe in detail the behavior of particles with $\rho_r = 1000$ and the data on the behavior of particles with $\rho_r = 1$ are provided in Table 3.3. For particles with elliptical cross sections, we use the Euler angle ψ defined in Figures 3.12 and 3.14 in order to describe the rotation of the particle around its own axis at $t = 0$. We specify $\psi = 0$ to be when the major axis of the cross-section ellipse at the positive end of the particle is orthogonal to the shear plane.

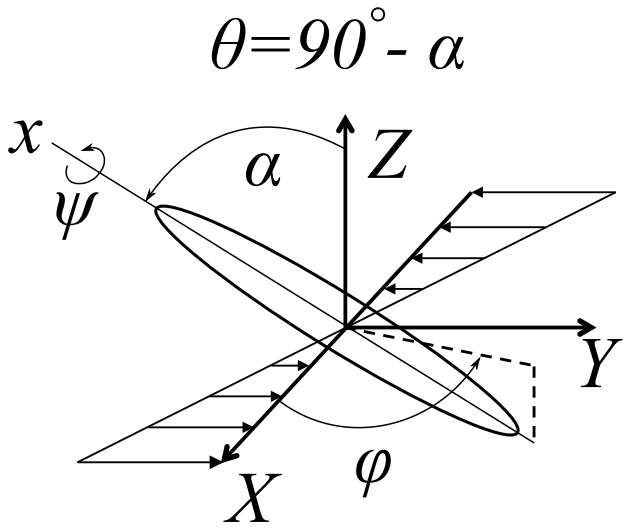

Figure 3.14: Angle θ and the particle.

For particle (**b**) ($a_r = 10$, straight circular cylinder), no out-of-plane rotation is observed. This particle experienced a periodic motion, replicating the behavior of an ellipsoid. In fact, our simulations show that the motion of this particle for both $\rho_r = 1$ and $\rho_r = 1000$ can be approximated by the motion of a prolate neutrally buoyant ellipsoid with $a_r = 11.35$.

The rest of the particles, [shapes (**c**)–(**f**)] show out-of-plane rotations, though for some of them it is dependent on the particle initial orientation ψ. Among the common characteristics of particle behavior, we can note the following: for most of the experiments, all fibers are oriented close to the shear plane, with θ about 5°; for short periods of time, when the particle axis approaches a 90° angle to the flow direction, we observed rapid increases in angle θ with local maxima of up to 41°.

In our simulations, the fiber (**c**) for two initial orientations $\psi = 0$ and $\psi = \pi/2$ (in these cases particle axes of inertia are aligned with the coordinate axes) would not leave the shear plane at all. But the introduction of initial angle $\psi = \pi/4$ resulted in two local maxima for an out–of–plane angle at $t = 36$ with $\theta = 25.8°$ and at $t = 72.7$ with $\theta = 13.75°$, as seen in Figure 3.15.

We now consider particle (**d**), the torus segment. In our experiments, this particle at $t = 0$ is placed in such a way that the torus radius is in the shear plane. In the dimensionless time interval [0, 100], we observe a growth of local maxima for angle θ by a factor of 3.6, starting at $\theta = 0.66°$, every $\Delta t = 26.2$ units of time, as seen in Figure 3.15.

Particle (**e**), because of its complex shape, express different types of behavior, depending

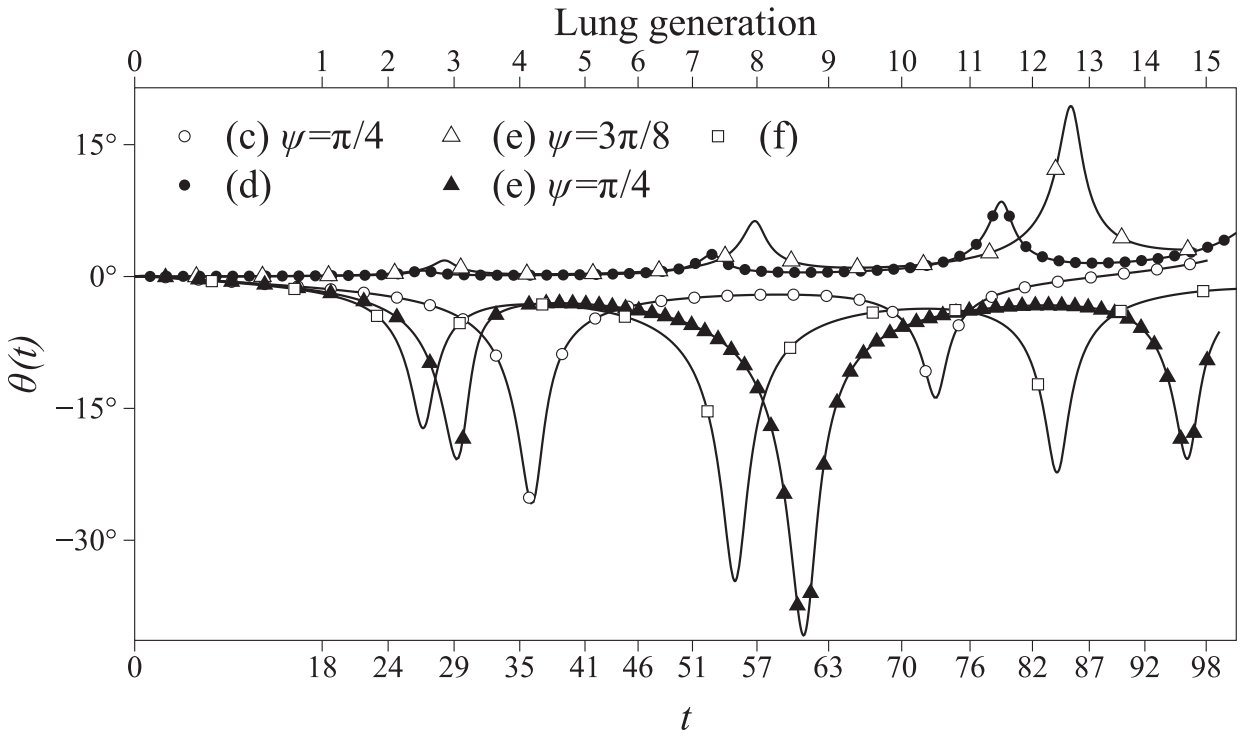

Figure 3.15: Out–of–plane angles for particles (**c**), (**d**), (**e**), and (**f**) with $\rho_r = 1000$ versus the dimensionless time t defined in Equation (3.39). The top horizontal axis labeling shows an approximate position in the lungs based on residence times in a [Finlay et al., 2000] lung model with an inhalation flow rate of 18 $litres/min$ and using a reference time scale $\gamma = 170s^{-1}$.

on how it faces the incoming flow at $t = 0$. With $\psi = -\pi/8$, our simulation show the particle tumbling with a period $T = 75.5$ and no out-of-plane rotation. Turning the particle to the initial angle $\psi = 3\pi/8$ give us a particle behavior similar to what we have seen in the torus segment: local maxima of θ occurred every $\Delta t = 28.1$ units of time increasing each time by a factor of 3.26 from the lowest local maximum $\theta(t = 28.1) = 1.82°$. With initial $\psi = \pi/4$, we observe the largest out-of-plane particle inclination of $\theta = 41°$: first, θ reach 21° at $t = 29.2$, then it increase to $\theta = 41°$ at $t = 60.7$, and finally at $t = 95.5$, it is again $\theta = 21°$.

Fiber (**f**), having been obtained by bending particle (**e**), show close resemblances to particle (**e**) in its rotational dynamics. At $t = 0$, the fiber is placed in such a way that the shear plane contain both the particle centroid and its radius of curvature. This lead to three local maxima at $t = 26.2,\ 54.5,$ and 83.7 with $\theta = 17.2°,\ 34.6°,$ and 22.3°, respectively.

The above results, as well as those obtained for $\rho_r = 1$, and the remaining particle types

		Local maxima $\rho_r = 1000$			Local maxima $\rho_r = 1$		
		I	II	III	I	II	III
(**b**)	θ_{max}	0	0	–	0	0	–
	t	35.93	71.86	–	35.93	71.86	–
(**c**) $\psi = 0$	θ_{max}	~ 0	~ 0	–	~ 0	~ 0	–
	t	37.34	74.68	–	37.34	74.68	–
(**c**) $\psi = \pi/2$	θ_{max}	~ 0	~ 0	~ 0	~ 0	~ 0	~ 0
	t	28.18	56.36	84.54	28.18	56.36	84.54
(**c**) $\psi = \pi/4$	θ_{max}	–25.8	–13.75	–	–26.0	–13.25	–
	t	36.1	72.7	–	35.27	71.9	–
(**d**)	θ_{max}	0.66	2.5	8.52	0.66	2.5	8.52
	t	26.2	52.4	78.6	26.2	52.4	78.6
(**e**) $\psi = -\pi/8$	θ_{max}	~ 0	~ 0	–	~ 0	~ 0	–
	t	37.35	75.5	–	37.35	75.5	–
(**e**) $\psi = 3\pi/8$	θ_{max}	1.82	6.3	19.4	1.8	6.5	19.2
	t	28.1	56.2	85.0	28.0	56.2	85.2
(**e**) $\psi = \pi/4$	θ_{max}	–20.7	–40.7	–20.7	–20.7	–41.4	–21.0
	t	29.25	60.7	95.5	29.2	60.0	94.6
(**f**)	θ_{max}	–17.2	–34.6	–22.3	–17.9	–35.0	–23.0
	t	26.2	54.5	83.7	26.3	55.0	84.4
(**g**)	θ_{max}	–5.2	–24.8	–	–5.1	–24.7	–
	t	32.1	65.65	–	31.9	65.4	–
(**h**)	θ_{max}	0.13 0.2	0.17 0.1	0.19 0.05	0.07 0.07	–0.01 –0.13	–0.19 –0.18
	t	14.5 29.1	43.6 58.2	72.7 87.3	14.4 28.9	43.2 57.8	72.3 86.8
(**i**)	θ_{max}	–21.8	–19.4	3.5	–22.0	–19.7	3.0
	t	24.9	51.1	76.2	25.1	51.7	76.9

Table 3.3: Local maxima for out–of–shear–plane angle θ (in degrees) for heavy and neutrally buoyant particles. Data in this table is gathered at the interval $t \in [0, 100]$, where t is a dimensionless time scaled with γ as given in Equation (3.39)

(**g**)–(**i**) are shown in Table 3.3.

Table 3.3 shows that the particle density has negligible influence on the dynamics of rotation for the fibers examined in our study, provided the aspect ratio and particle shape remain fixed.

Table 3.3 also includes simulations with spring-shaped particles (**g**)–(**i**), with the centerline described by the equation of a helix. Since the shapes of these fibers differ in many ways, the only common characteristic we notice is that the observed time intervals between tumbling for these particles are significantly shorter than we would expect for particles with such length to diameter ratios. We compare the measured periods of rotation for our

particles with the periods of rotation for prolate ellipsoids from [Jeffery, 1922]. We find that an equivalent ellipsoid aspect ratio a_e for the given period T of helical particle tumbling derived from the equation

$$T = \frac{2\pi(a_e^2 + 1)}{\gamma a_e} \tag{3.41}$$

is much closer to the coil aspect ratio a_c, which is the length to width ratio for a parallelepiped around the particle, than to a_r (the actual curved particle aspect ratio).

Particle (**g**) is a spring–like particle wrapped around its own axis. This fiber developed very similar behavior to that observed in simulations for particles (**c**)–(**f**). As shown in Figure 3.16, for this particle, θ rather rapidly grew to 3.2° and stayed there for a long time until, before flipping, the particle axis shifted to the other side of the shear plane with a maximum inclination angle $\theta = -5°$ at $t = 32.1$, afterwards returning to $\theta = 2.5°$ before growing again up to $\theta = -24.8°$ at $t = 65.65$. The approximate period of rotation $T = 65.65$ corresponds to an equivalent ellipsoid aspect ratio $a_e = 10.35$, while the coil aspect ratio is $a_c = 7.5$ and actual aspect ratio $a_r \approx 15$.

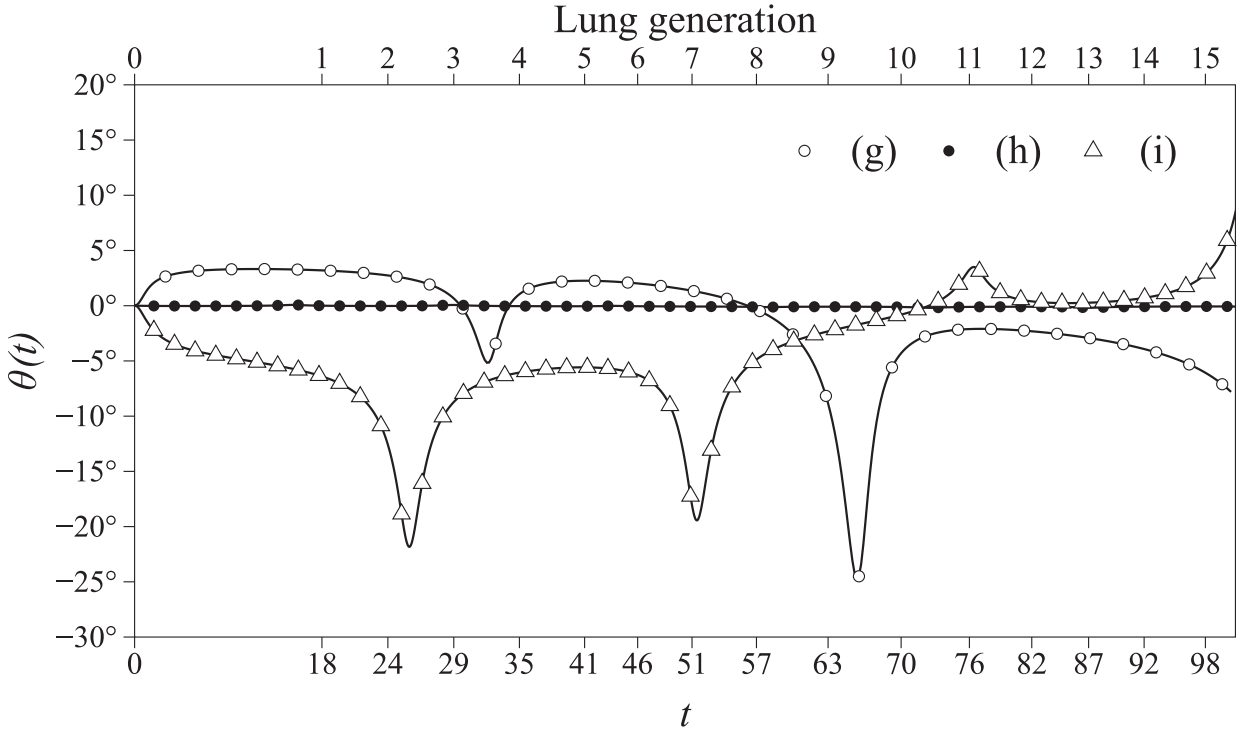

Figure 3.16: Out–of–plane angles for particles (**g**), (**h**), and (**i**) for $\rho_r = 1000$.

Particle (**h**) is derived from the same equations as particle (**g**), but this time the fiber

is made longer and with a relatively larger helical radius. To our surprise, this particle show only small signs of out–of–plane rotation and no rotation ψ around its own axis. The maxima of θ occur with period $T_\theta = 14.55$, which is a half period of particle tumbling, and all are smaller than 0.2°. The period of rotation $T = 29.1$ correspond to an equivalent ellipsoid aspect ratio $a_e = 4.4$, while the coil aspect ratio $a_c = 3.7$ and actual aspect ratio $a_r \approx 26$.

Finally, we combine the cylindrical and helical particles in order to obtain fiber (**i**). Its centerline is a conical helix, with zero helical radius on one side and helical radius $2.15d_f$ on the other side. This time, the particle expresses a more interesting out–of–plane rotation compared with the two other helical fibers. First, two maxima of $\theta = -21.8^\circ$ and $\theta = -19.4^\circ$ occur at $t = 24.9$ and $t = 51.1$ respectively, before a third out–of–plane angle maximum is observed from the other side of the $X - Y$ plane with $\theta = 3.5^\circ$ at $t = 76.2$, as seen in Figure 3.16. For this particle, the period of rotation can be estimated to be $T \approx 51$ allowing us to calculate $a_e = 8$, while $a_c = 4.65$ and $a_r \approx 22$.

3.3.3 Discussion

Results presented in the current work clearly demonstrate the validity of the suggestion [Timbrell, 1970] that fibers with complicated geometries have less tendency to align with the flow, which is based on the observation that curly fibers can deposit significantly more proximally and in greater amounts in comparison to straight thin fibers. Indeed, we have shown that even when a complex particle enters the upper airway stream with angular velocity parallel to the local fluid vorticity, it will most likely develop a rotation perpendicular to the plane of shear. In contrast, if a Jeffery–like fiber is inclined to the shear plane at some point, then the particle would tumble within predicted angles of inclination with a tendency to drift toward the shear plane. The complex–shaped particles that we have examined do not obey such behavior and may develop large inclination angles.

Fibers (**c**)–(**f**) and (**i**) express more variability in their behavior than straight rods of similar aspect ratio. If we consider symmetrical and asymmetrical straight fibers initially aligned with the flow in an airway and neglect all other factors influencing deposition efficiency except fluid shear, the interception diameter for the symmetrical fiber will be equal to the particle diameter, while for the asymmetrical fiber it will be higher due to the development of an out–of–plane rotation, and this difference will increase proportionally to the particle's aspect ratio. We have found that the time needed for a particle to gain enough departure from the shear plane is measured by at least one period of tumbling; this period

is close to the Jeffery result for ellipsoids of the same aspect ratio. Such periods are much longer than fiber residency times in any particular airway. However, as particles travel through the lungs, during the course of several lung generations, they may gain enough out–of–plane motion to significantly enhance interception and thereby support conclusions about different interception diameters for symmetrical versus more complex particles.

One important conclusion can be drawn from our simulations of helical fibers. We observe that the rotation of such fibers is more dependent on the coil aspect ratio (the length to width ratio of the parallelepiped bounding the particle) than on the actual aspect ratio measured as a curvilinear length to diameter ratio. This may suggest more frequent flipping of curly/curved fibers in the lungs, as compared with straight fibers with the same lengths and diameters. This subsequently leads to a substantial increase in the deposition of curly/curved particles due to interception. More frequent flipping may be another mechanism working together with larger interception diameters and weaker tendencies of curly fibers to align with the flow.

In view of these results, we can propose an explanation for the large differences between the masses of amphiboles and chrysotile fibers recovered from rats in the experiments described by [Timbrell, 1970]. It is plausible, and in agreement with the results of [Harris Jr and Timbrell, 1975], that most of the curly chrysotile fibers are deposited in the tracheobronchial airways and are cleared by the mucociliary escalator from the lungs within 24 hours, while straight long fibers penetrate deeply into the alveolar region and are retained there because of the much slower process of clearance by the alveolar macrophages.

3.4 Deposition of Fibers due to Magnetic Field Alignment

3.4.1 Problem Formulation

A three-dimensional model of a bifurcating airway corresponding to generation 14–15 within a typical human lung is developed and deposition of high aspect ratio ellipsoid particles is studied for fixed particle orientations. This model corresponds to the same airway generation that [Martin and Finlay, 2008a] study in vitro, selected because it is found to be an optimal region for deposition enhancement due to magnetic alignment [Martin and Finlay, 2008a]. The model design is based on the morphologically realistic bifurcation described by [Hegedűs et al., 2004]. The bifurcation model is an generalization of the physiologically realistic model proposed by [Heistracher and Hofmann, 1995], which is assumed to produce

a good approximation of the transition zone. The transition region design is important because it strongly influences fluid flow within a bifurcation model, therefore affecting deposition results [Balásházy et al., 1996]. Parameters needed to describe our model as well as the geometry of the bifurcating airway are presented in Figure 3.17

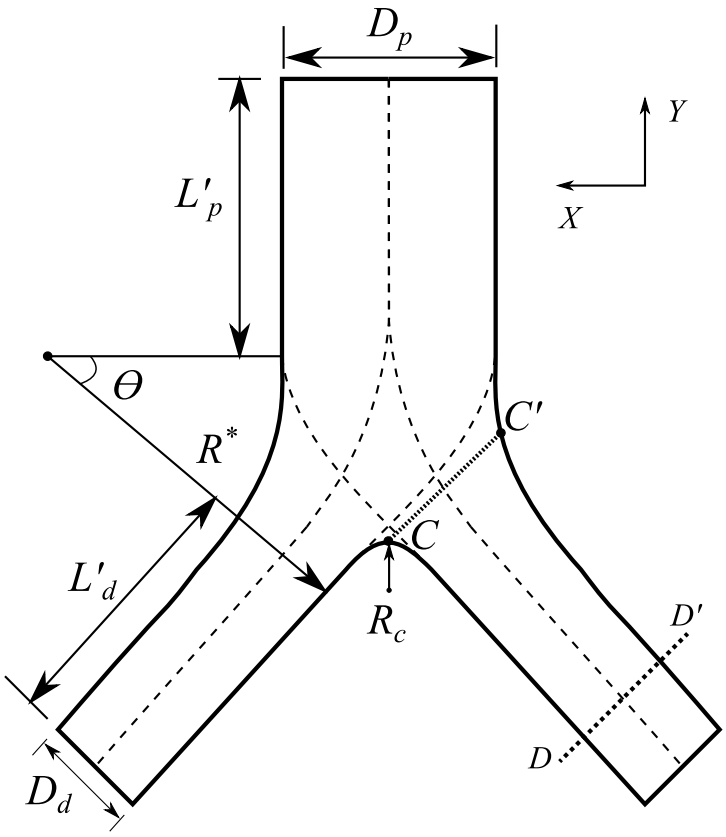

Figure 3.17: Sketch of the symmetric airway bifurcation based on the model described in [Hegedűs et al., 2004].

The bifurcation in Figure 3.17 is made of three subdomains. The first subdomain is the so called parent region, which is a straight cylinder with a diameter D_p and length L'_p. The transition region is comprised of two identical narrowing tubes that branch out from the parent region following a curve with a curvature R^* and a bifurcation angle θ. The daughter branch follows transition region and is modeled as a straight cylindrical tube with length L'_d and diameter D_d. [Hegedűs et al., 2004] propose the following equations for L'_p

and L'_d:

$$L'_p = 0.8L_p \tag{3.42}$$

$$L'_d = 0.2L_p + L_d - \theta R^* \tag{3.43}$$

with L_p and L_d being the lengths of parent and daughter branches, respectively. We have to use equations in the form of (3.42)– (3.43) because in the literature L_p and L_d are usually given such that their sum is equal to the length of three regions making our model, *i.e.*,

$$L_p + L_d = L'_p + L'_d + \theta R^*.$$

For the present study we use lengths based on the [Finlay et al., 2000] lung model, except that their lengths are calculated as the total length of each generation. Therefore, Equations (3.42)– (3.43) are applied for three consecutive bifurcations spanning generations 13 to 15 ensuring that the sum of L_p and L_d for generation 14 is equal to the total length given by [Finlay et al., 2000]. The [Finlay et al., 2000] lung model also supplies us with the diameters D_p and D_d for parent and daughter regions. The radius R_c describing the carina and radius of curvature in transition region R^* are found from the following relations for a normal human bronchial tree [Horsfield et al., 1971]:

$$1 < \frac{R^*}{D_p} < 0.1 \text{ for } D_p < 1.5 \text{ mm} \tag{3.44}$$

$$\frac{R_c}{D_p} < 0.1 \text{ for an average } R_c. \tag{3.45}$$

Equation (3.45) is verified by [Hammersley and Olson, 1992] in casts for small human airways with diameters less than 0.1 mm. The mean angle $\theta = 50^\circ$ in the transition region for branches with diameters less than 1 mm is reported by both [Horsfield et al., 1971] and [Hammersley and Olson, 1992]. Parameters used to design the three–dimensional symmetrical bifurcating geometry of an airway are presented in table 3.4.

D_p(mm)	D_d(mm)	L'_p(mm)	L'_d(mm)	R^*(mm)	R_c(mm)	θ°
0.61	0.49	0.62	0.92	0.98	0.049	50

Table 3.4: Parameters for 3-D airway bifurcation geometry.

The bifurcation geometry is designed following the steps proposed by [Hegedűs et al.,

2004] for the morphologically realistic bifurcation model using a computer–aided design software; for our simulations, Pro/ENGINEER software is used. The geometry is then imported into the GMSH finite element grid generator [Geuzaine and Remacle, 2009]. A Delaunay-type algorithm is chosen in order to generate an unstructured tetrahedral grid.

Steady Flow in Airway Bifurcation

The conditions simulated in this study are for inhalation through airway generation 14 of the [Finlay et al., 2000] lung model, with a breathing flow rate of 18 litres/min, which is typical for normal tidal breathing. For symmetrically branching airways, this gives an average inlet velocity of $V_{avg} = 63$ mm/sec. Gravity is oriented in the direction normal to the inlet of the considered bifurcation. Characteristic length $L = 0.73$ mm, velocity $U = 174.99$ mm/sec, and kinematic viscosity $\nu = 15.08$ mm^2/sec are used to scale the Navier-Stokes equations in the form of (3.1), resulting in $Re = 8.47$ and $Fr = 4.28$ for the particle motion equations (3.2). Since the Reynolds number is within the laminar region, a Poiseuille parabolic velocity profile is prescribed at the inlet:

$$V_Y = -2V_{avg}(1 - \frac{4r^2}{D_p^2}) \qquad on\ \partial\Sigma_{inlet} \tag{3.46}$$

$$V_X = V_Z = 0 \qquad on\ \partial\Sigma_{inlet} \tag{3.47}$$

The outlet boundary condition with zero pressure and vanishing normal component of the velocity gradient is prescribed at both daughter outlets. The initial condition for the fluid velocity everywhere except the inlet is set to zero. A dimensionless time step $\Delta t = 10^{-4}$ is used to ensure stability of the time integration. The fluid flow simulations through the airway bifurcation are considered convergent to a steady state once the velocity residuals in maximum norm reached values less than 10^{-7}. The steady-state velocity is interpolated at every time step along the particle trajectory as a boundary condition for the micro-grid simulations; see algorithm description in Section 3.2.3.

The Grid Convergence Method [Celik et al., 2008] is used to estimate the grid convergence of our numerical method on the macro-grid. Five successively refined meshes are used to study the convergence. It is estimated between pairs of grids, each pair consisting of a coarse grid and a fine grid that has two times more elements than the coarse grid. The grid convergence index (GCI) is computed for each pair as

$$GCI = F_s \frac{\varepsilon_{rms}}{r^p - 1},$$

where the root-mean-square error ε_{rms} is calculated based on the relative error in velocity at 1000 points randomly chosen inside the domain, the formal order of the method $p = 2$, the refinement factor r is the ratio between the number of nodes in the refined and coarse meshes, and the factor of safety $F_s = 3$ which accounts for r being smaller than two because doubling the number of elements does not correspond to the same rate of increase in the number of grid nodes.

Eventually, the fluid flow within the bifurcation domain is resolved on a macro-grid with approximately 1635000 tetrahedral elements. The GCI computed between the final macro-grid and a coarser grid with 894000 elements is found to be 1.39%, which is lower than 5% reported by [Longest and Xi, 2007] to be adequate for the accurate deposition results when compared with experiments.

Particle Simulations

The shapes of the high aspect ratio particles in our simulations are approximated by prolate ellipsoids with fixed diameter $d_e = 0.5$ μm and lengths dependent on the particle aspect ratio $l_e = d_e a_r$. Particle aspect ratios of 6 and 20 are considered. The specific choice of particle diameter $d_e = 0.5$ μm and aspect ratio $a_r = 6$ is motivated by the volume median diameter and by the volume median length for particles in previous in–vitro study [Martin and Finlay, 2008a]. The particle-fluid density ratio is set equal to $\rho_r = 1000$.

The geometry of the micro-grid Ω_r (Section 3.2.3) is built using the FEM meshing software GMSH [Geuzaine and Remacle, 2009]. The micro-grid has a shape of a rectangular box with height 12 times the diameter of the particle d_e and length 3 times greater than the length of the particle l_e. [Dechaume et al., 2010] report that increasing the micro-grid size from five to ten and then to twenty times the length of the particle has a negligible effect on the particle transport in the airway bifurcation similar to the one studied here. Additionally, we observe that doubling the size of the micro-grid, results in a final deposition position 0.05 mm farther downstream. For a particle with an aspect ratio of 6 to deposit 0.05 mm farther downstream means that the inlet normalized position in X direction would have to be increased by at most 0.0007.

The number of elements inside the micro-grid is kept 49212 and 95795 for particles with aspect ratios of 6 and 20, respectively. The computational grid is designed such that the most number of tetrahedra are located within particle volume. The number of elements found inside the particle is 28592 for $a_r = 6$ and 65361 for $a_r = 20$. Increasing the number of elements inside the micro-grid by a factor of two resulted in a final position 0.019 mm farther downstream for particles with $a_r = 6$ and less than 0.001 mm for particles with

$a_r = 20$.

Starting from $\Delta t = 10^{-3}$, decreasing the dimensionless time step has a negligible effect on the trajectory of the particle with constrained angular orientation. Therefore, a time step $\Delta t = 10^{-3}$ is used in order to ensure an accurate trajectory resolution and a Courant number in the micro-grid Ω_r less than one.

For each numerical experiment, the initial particle position, orientation and velocity has to be prescribed. The initial location of the particle $\boldsymbol{X}_p$ is always chosen so that the micro–grid Ω_r lies entirely inside the fluid domain Σ. The initial particle centroid velocity $\boldsymbol{U}_0$ is chosen to be equal to the Poiseuille velocity at particle centroid. The particle angular orientation $\boldsymbol{\vartheta}_0$ and velocity $\boldsymbol{\omega}_0$ depended on the setup being studied. At each time step, velocities on the micro-grid Dirichlet boundary are interpolated from the results of the fluid-only simulations.

Computations are performed on a Dell PowerEdge 2900 server with two Intel E5430 quad-core processors and 16 Gb of memory. A single particle simulation on four cores with OpenMP shared memory parallelization (each spatial direction is solved on a separate thread, and large tasks such as integration are shared between all four available threads) resulted in a computational time per time-step between 5 and 30 seconds.

Deposition

A particle is considered deposited when it touches the airway wall before traveling past a designated cutoff plane in the daughter tube. The cutoff plane (D–D' on Figure 3.17) is positioned 0.45 mm downstream from the bifurcation carina and is set parallel to the outlet. We use this approach in order to reduce computational time and as a measure to avoid undesirable effects close to the outlet boundary. Deposition efficiency is defined as the ratio between the volumetric flow rate within a deposition boundary (Figure 3.18) at the parent inlet and the total flow rate. The deposition boundary in some sense is similar to the limiting trajectory boundary previously implemented for calculation of deposition efficiency in [Cai and Yu, 1988; Asgharian and Yu, 1989]. Particles with centroid position located within the deposition boundary are considered deposited, while particles outside the boundary do not deposit.

For different positions along the Z axis (Figure 3.18), particle simulations are performed to find an X coordinate such that the particle released from this position deposited near the cutoff plane, thus defining one deposition limiting point at the inlet. The deposition boundary is composed of linear segments linking deposition limiting points. The deposition boundary between the last limiting point and the inlet wall is found by extrapolation. The

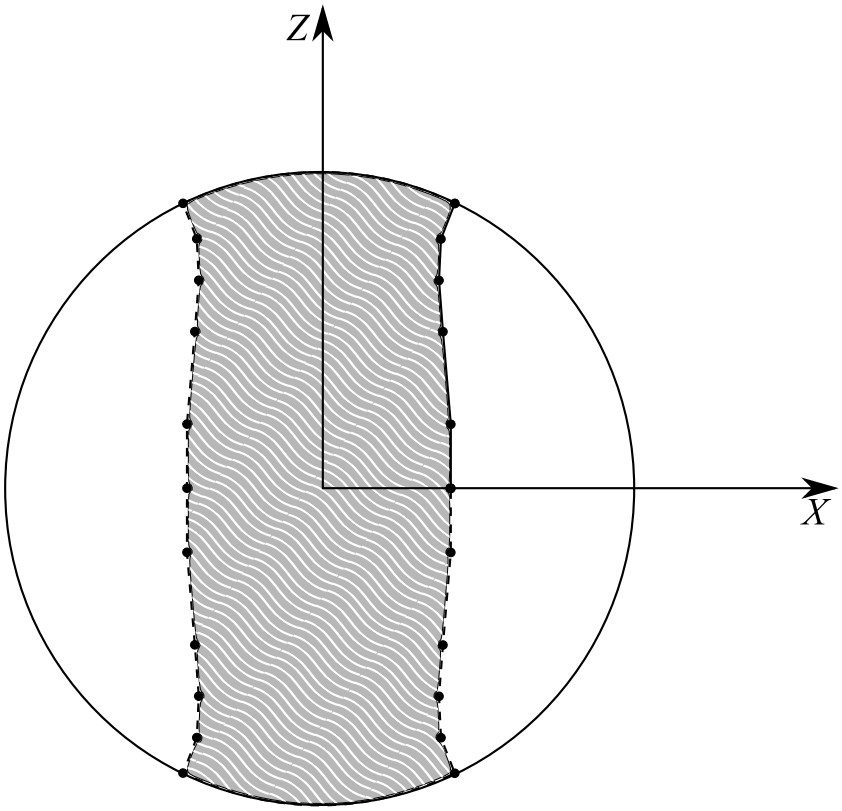

Figure 3.18: Sketch of the deposition boundary at the airway inlet. The black dots are the starting positions of particles that deposited near the cutoff plane. The bold solid line is the deposition boundary consisting of linear segments connecting deposited points. The dotted line is obtained by reflecting deposition boundary in X–Z plane with respect to Z axis and then reflecting obtained image in the upper half–plane with respect to the X axis. The particles entering domain within the striped region are considered deposited.

slope of the linear equation near the wall is calculated from the assumption that the ratio between the slopes of the extrapolated equation and the last measured segment is the same as the ratio between slopes of the last two measured segments. The deposition boundary is assumed to be continuous and symmetric with respect to the Z and X axes. We should note that the definition of deposition efficiency which we use for our study is restricted to monodisperse aerosols with a constant particle concentration density at the inlet.

For each deposition limiting point, we perform another simulation with fiber initial position at the same Z coordinate but further away in X direction, such that the particle does not deposit, producing a non-deposited boundary similarly to the deposition boundary. The area between the non–deposited boundary and the deposition boundary represents a region of uncertainty, where we can not say whether the particle leaves the daughter airway

or deposit in it. To measure this uncertainty, we compute a deposition boundary error as the difference between the deposition efficiency given by the deposited and non–deposited boundaries. The deposition efficiency and deposition boundary error are calculated for the following two cases:

Case 1 : Particle along its trajectory is aligned with local fluid streamlines direction. At $t = 0$ fiber major axis is set parallel to Y axis, and once the particle enter the daughter airway, its major axis is realigned parallel to the daughter streamlines. This setup simulates deposition without the presence of magnetic field.

Case 2 : The particle's angular orientation $\boldsymbol{\vartheta}$ is set constant along the particle's trajectory to model deposition of a magnetically susceptible particle in the presence of a strong magnetic field. The initial angular orientation of the particle is set so that the major axis of ellipsoid is parallel to the X axis as shown in Figure 3.18.

We also take into consideration the deposition region along the airway bifurcation wall ($X^2 + Z^2 = D_p^2/4$), which is not outlined in the deposition boundary presented in Figure 3.18. For case **2**, any particles that are closer than half a particle length in the X direction have to deposit on the bifurcation wall, therefore the outer interception deposition boundary is located half a particle length from the bifurcation wall. For case **1**, interception deposition at the airway bifurcation wall is ignored as it would be negligible compared to case **2**. Due to limited computational resources, we did not study particles free to rotate without constraints on angular motion. However, we have shown before that the present particles tend to remain aligned with the flow streamlines for periods much greater than the transition time through the airway, see Table 3.3, Figures 3.15 and 3.16. For the set of parameters used in our study, the estimated period of rotation [Jeffery, 1922; Gans, 1928] is about 7 times greater for particles with $a_r = 6$, and 17 times greater for particles with $a_r = 20$ than the estimated particle residence time in the airway. The rotational Peclet number, which is the ratio of the hydrodynamic shear rate and the Brownian diffusion coefficient, is much greater than 1 for both particle dimensions [Asgharian and Yu, 1989]. Therefore, setup **1** can be considered as a reasonable approximation to the case with unconstrained angular motion.

3.4.2 Results

The Hagen-Poiseuille flow profile in the parent airway holds its shape until the transition region, where the flow splits symmetrically into the two daughter tubes. Once entering the

daughter airway, the axial flow pattern regains a parabolic-like shape. Figure 3.19 shows the axial velocity profile across the airway diameter C—C′ outlined in Figure 3.17. The point of maximum fluid velocity across the diameter C—C′ does not occur exactly in the middle of the C—C′ line, but instead is observed slightly skewed to the outer side of the bifurcation. Once flow is through the transition region and in the daughter airway, the flow pattern regains a Poiseuille profile. We compare velocity profile at 0.146 mm downstream of the transition region for two values of $L'_d = 0.461$ mm and $L'_d = 1.846$ mm. The change in L'_d cause the three-dimensional velocity profile to change by less than 0.01%, indicating that the outlet boundary placement is such that it does not affect the flow.

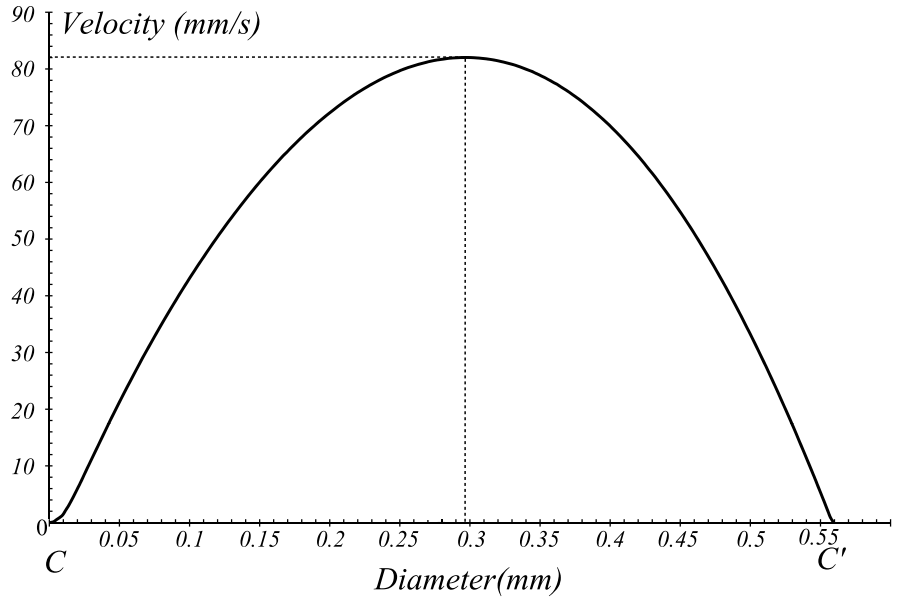

Figure 3.19: Axial velocity along the daughter tube diameter C–C′.

Figures 3.20 and 3.21 present the deposition boundary at the inlet surface of the parent airway. For $a_r = 6$ case **1** and case **2** deposition boundaries near the inlet center (Z=0) are approximately the same. At $Z_{scaled} = 10$, the deposition regions for case **1** and case **2** become narrower, with the case **1** limiting point being to the left of the limiting point for setup **2**, Figure 3.20. Observed deposition efficiencies for both cases **1** and **2** start to significantly increase approximately at the distance of 65 particles lengths along the Z axis ($Z_{scaled} = 65$). The observed increase is more significant for case **1**, such that at $Z_{scaled} = 74$ the corresponding deposition boundary has larger X coordinate than that of case **2**. Starting from this point, case **1** has larger local deposition efficiency than case **2** until at $Z_{scaled} = 90$ case **2** deposition boundary surpasses case **1** and has greater X

coordinate up to the airway wall at $Z_{scaled} = 101.6$; see Figure 3.20.

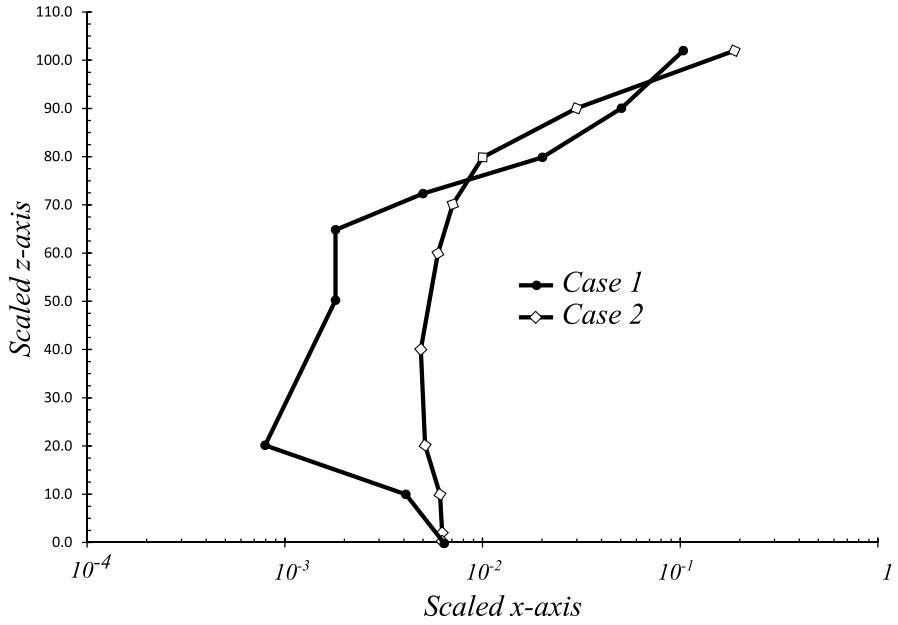

Figure 3.20: Case **1** and case **2** deposition regions for particle with $a_r = 6$. Boundary lines represent the limits where the particles entering to the left deposit and those to the right do not deposit. The X and Z axes are the same as seen in Figure 3.18. The X and Z axes are scaled with the length of a particle with $a_r = 6$, on top of that log-transformation of the X axis is performed. The bifurcation inlet wall is located at $Z_{scaled} = 101.6$.

For particles with $a_r = 20$, the deposition boundary curves for cases **1** and **2** start with a relatively constant slightly positive slope near the center of the inlet; see Figure 3.21. Local deposition efficiencies increase nearing the outside bifurcation boundary but contrary to what we observe in Figure 3.20 for particles with $a_r = 6$, the case **2** boundary is always to the right of the case **1** boundary.

Table 3.5 summarizes calculated deposition efficiencies and the deposition boundary errors for particles with aspect ratios $a_r = 6$ and $a_r = 20$ for simulations where particles are aligned with the flow streamlines (case **1**) and for particles with alignment due to magnetic field (case **2**). The deposition boundary error was defined in Section 3.4.1 as the deposition through the uncertainty region between measured deposition boundary and the boundary of the no-deposition region. The smallest and the largest deposition boundary errors recorded are $\Delta_2^{20} = 0.00057\%$ and $\Delta_1^6 = 0.00118\%$; see Table 3.5. The deposition boundary error in our simulations is kept below 14% of the deposition efficiency. However, the estimate for the final deposition error is higher than the actual error, because in our simulations some of the non-deposited particles are observed greatly past the cutoff plane.

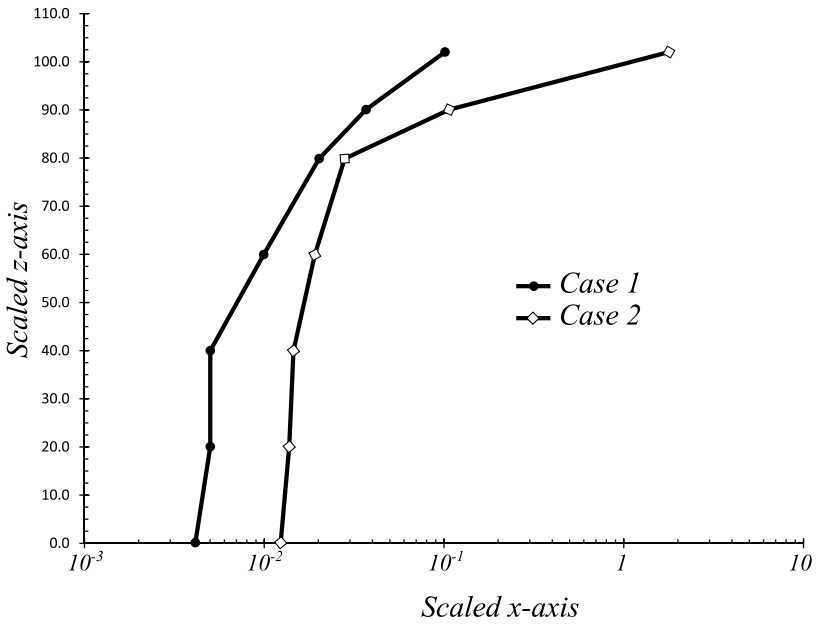

Figure 3.21: Case **1** and case **2** deposition regions for particle with $a_r = 20$. Boundary lines represent the limits where the particles entering to the left deposit and those to the right do not deposit. The X and Z axes are the same as seen in Figure 3.18. The X and Z axes are scaled with the length of a particle with $a_r = 6$, on top of that log-transformation of the X axis is performed. The bifurcation inlet wall is located at $Z_{scaled} = 101.6$.

Due to limited computational resources we do not perform a more detailed study of this parameter since it is still pretty small as it is. The outside wall interception region that only

	Case **1**		Case **2**	
Aspect ratio a_r	Deposition efficiency $d_1(\%)$	Deposition boundary error $\Delta_1(\%)$	Deposition efficiency $d_2(\%)$	Deposition boundary error $\Delta_2(\%)$
6	0.0092	0.00118	0.0131	0.00059
20	0.0149	0.00111	0.0515	0.00057

Table 3.5: Deposition efficiencies and Deposition boundary errors in airway bifurcation for ellipsoid particles with $a_r = 6$ and $a_r = 20$ calculated using Deposition boundaries presented at Figures 3.20 and 3.21. Deposition boundary error is defined in Section 3.4.1.

applies to case **2** as discussed in Section 3.4.1 yielded a deposition efficiency of $d_w^6 = 0.0048\%$ and $d_w^{20} = 0.0540\%$ for fibers with aspect ratio 6 and 20, respectively.

Values for deposition enhancements $e = d_2/d_1$ for the two particles considered in our studies are presented in Table 3.6. As particle aspect ratio a_r increases from 6 to 20 (by

a factor of 3.3), we observe increase in deposition enhancement by a factor of 2.4. The deposition boundary enhancement range calculated as

$$\left[\frac{d_2}{d_1+\Delta_1};\ \frac{d_2+\Delta_2}{d_1}\right] \tag{3.48}$$

represents the smallest and the largest possible values for the enhancement e. If we include into consideration deposition efficiencies d_w^6 and d_w^{20} due to interception on the outside walls (away from the carina), the observed enhancement increases to 1.95 for particle with $a_r = 6$ and to 7.08 for particle with $a_r = 20$, Table 3.6, with deposition boundary enhancement range defined as

$$\left[\frac{d_2+d_w}{d_1+\Delta_1};\ \frac{d_2+\Delta_2+d_w}{d_1}\right]. \tag{3.49}$$

	$a_r = 6$		$a_r = 20$	
	Deposition enhancement e_6	Deposition enhancement interval	Deposition enhancement e_{20}	Deposition enhancement interval
Deposition boundary only	1.42	1.26–1.49	3.46	3.22–3.49
Deposition boundary with Outer wall	1.95	1.72–2.01	7.08	6.59–7.12

Table 3.6: Deposition enhancement for ellipsoid particles with $a_r = 6$ and $a_r = 20$ between cases **1** and **2**.

3.4.3 Discussion

The shapes of the deposition boundaries observed in Figures 3.20 and 3.21 can be justified in view of the different deposition processes influencing particle motion. For both aspect ratios, small differences in deposition boundaries between case **1** and **2** recorded close to the airway center (X=Z=0) are expected because of the prescribed inlet velocity and airway geometry. In this region the velocity is the largest and its profile is almost flat which locally makes it similar to plug-like flow. Fibers are carried away with the flow into daughter airways and only a small fraction of them deposit close to the bifurcation

carina due to bifurcation symmetry. Under such conditions, particle orientation does not significantly affect deposition. In contrast, higher velocity gradient and significant variation in the airway geometry close to the parent airway wall cause significant curvature of the deposition boundary. The velocity profile, its small magnitude, and bifurcation geometry would encourage deposition due to interception and sedimentation. This explains why, for both aspect ratios studied, the Z location at which the deposition begins to extend out into the X direction is similar. For higher aspect ratio, increased particle mass and length account for higher deposition due to sedimentation and impaction. This explains what we observe for an aspect ratio of 20 – the deposition boundary begins to curve at a lower Z_{scaled} position than for the aspect ratio 6 fibers. For fibers with aspect ratio 6 we observe that at $Z_{scaled} = 74$, the deposition boundary for streamline aligned fibers (case **1**) starts to extend past the boundary for magnetically aligned fibers (case **2**). In this region, interception for the shorter particle has become less dominant than sedimentation. An $a_r = 6$ particle is not long enough to overcome the relative importance of sedimentation until much closer to the wall. The bifurcation geometry close to the outside wall within the transition region would facilitate deposition by interception. Therefore, we observe that the case **2** deposition boundary grows at a much higher rate close to the wall and eventually surpasses the boundary of streamline aligned fibers.

A simple estimate of deposition of high aspect ratio particles in a lung bifurcation can be made using analytical approaches. We calculate estimates for deposition efficiencies due to sedimentation ([Heyder and Gebhart, 1977] with shape factors for ellipsoidal particles [Oseen, 1927]) and probabilities for impaction and interception using [Cai and Yu, 1988] approach. However, these analytical values are found to be 7 to 20 times higher than the values we observe in our simulations. This difference is similar to that which [Cai and Yu, 1988] observed between their analytical deposition results and experiments by [Myojo, 1987], who study fibers with diameters of 1.2–2.3 μm and aspect ratios between 8.3–16.7. Compared with the experiments of [Martin and Finlay, 2008a] where particles and bifurcation dimensions are similar to the values used in our simulations, we find deposition enhancement of 1.42 for a particle with $a_r = 6$ (Table 3.6) is similar to their value of 1.7, especially considering our value of 1.95 that occurs when deposition on the outside bifurcation wall is included. However, it should be noted that we do not consider the effect of Brownian motion on particle trajectory in our simulations. It is evident that deposition due to Brownian diffusion contribute to the results found by [Martin and Finlay, 2008a]. The importance of Brownian diffusion in the [Martin and Finlay, 2008a] study is due to the combination of particle diameters being much less than 0.5 μm and the use of parent

and daughter airways that are over four times longer than what is anatomically correct. The much longer daughter length used in [Martin and Finlay, 2008a] would result in much higher sedimentational deposition. These reasons may explain the discrepancy in absolute deposition efficiency between our computational results and the *in–vitro* results in [Martin and Finlay, 2008a].

An increase in aspect ratio from 6 to 20 is accompanied by increased deposition efficiency by a factor of 1.62 for case **1** and by a factor of 3.93 for case **2**. This type of enhancement in deposition has been reported before in other studies [Sturm and Hofmann, 2006] that assume particles aligned with the streamlines. Therefore, increasing particle aspect ratio gives better results when fiber angular position is controlled. An additional advantage of increasing aspect ratio from 6 to 20 is that change in particle length keeping the same diameter increases local mass deposition by 3.33 times. Such mass deposition enhancement is especially useful when increase in the therapeutic effect of aerosol drugs is desired.

However, increase in deposition enhancement due to larger fiber aspect ratio is not equal to the coefficient of fiber length increase. Instead, the enhancement factor increased by a factor of 2.44 when aspect ratio increases by a factor of 3.33 (based on first row in Table 3.6). Nevertheless, this number suggests that local deposition enhancement due to magnetic field alignment can be over two times more effective with higher aspect ratio particles than those used previously in the *in–vitro* study by Martin and Finlay [2008a].

Chapter 4

Fluid-structure interaction (FSI)

4.1 Problem formulation

In the following we describe a FSI numerical approach for direct numerical simulations of the dynamical interaction between a Newtonian liquid and an incompressible solid having equal densities and viscosities. For many applications of the FSI algorithms the assumption of a nonzero viscosity in the solid constitutive law has a negligible effect on the model accuracy due to small velocity gradients in the solid phase. At the same time, the viscous part of the solid stress significantly improves stability of numerical simulations that is important for 3-D applications where severe time-step restrictions otherwise arise. Additionally, many biological flows involve coupled dynamics of a liquid interacting with a solid that is saturated with the liquid itself. As such, the constitutive model for the solid is viscoelastic. Following the algorithm description, we briefly discuss how the assumptions of equal densities and viscosities can be lifted with a consistent perturbation to the original governing equations with nonconstant coefficients without imposing major changes to the presented algorithm.

The fluid-solid computational domain Ω is a union of the fluid Ω_f and solid Ω_s subdomains, $\Omega = \Omega_f \cup \Omega_s$ (see Figure 4.1). The fluid-structure interface is denoted by Γ_i and has a unit normal $\boldsymbol{n}$ pointing outside of the solid. The computational domain boundary $\partial\Omega$ may in some places coincide with a part of the solid boundary which is not a fluid-solid interface. In the present description we assume $\Gamma_i = \partial\Omega_s$, but the formulation can be easily generalized to the case when a part of the solid boundary is a Dirichlet boundary, adding one extra surface integral to the combined weak formulation of the momentum equations for fluid and solid.

For an incompressible fluid and solid the nondimensional governing equations in an

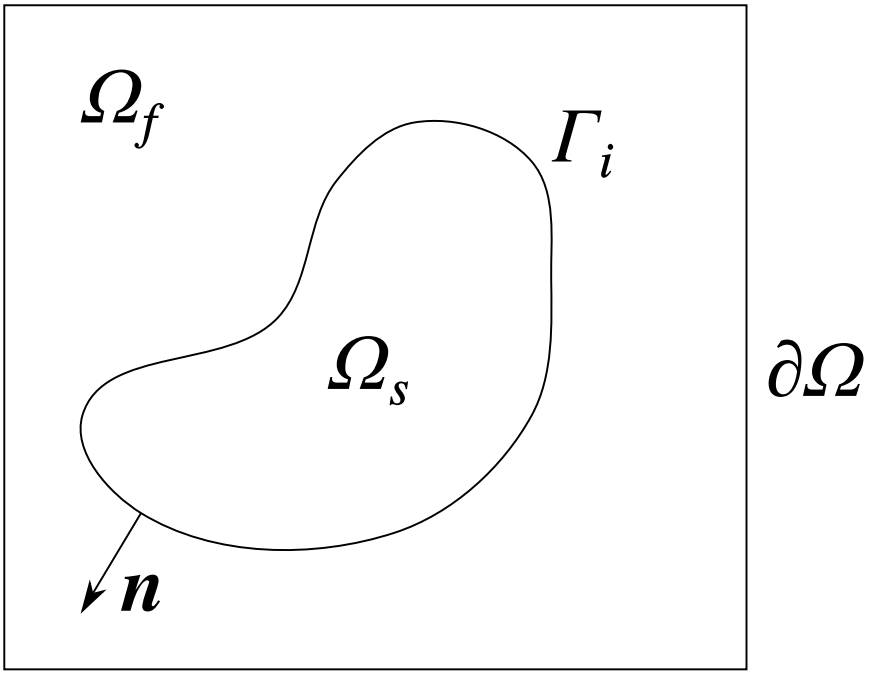

Figure 4.1: Abstract domain setting for a FSI problem. Illustrated: fluid domain Ω_f, deformable solid domain Ω_s, fluid-structure interface Γ_i, and computational domain boundary $\partial\Omega$.

Eulerian framework can be generalized to

$$\frac{D\boldsymbol{v}_f}{Dt} = \boldsymbol{\nabla}\cdot\boldsymbol{\sigma}_f, \qquad \boldsymbol{\nabla}\cdot\boldsymbol{v}_f = 0 \qquad \text{in } \Omega_f, \tag{4.1}$$

$$\frac{D\boldsymbol{v}_s}{Dt} = \boldsymbol{\nabla}\cdot\boldsymbol{\sigma}_s, \qquad \boldsymbol{\nabla}\cdot\boldsymbol{v}_s = 0 \qquad \text{in } \Omega_s, \tag{4.2}$$

nondimensionalized with the density, and the corresponding velocity and length scales. Here, $\boldsymbol{v}_s$ and $\boldsymbol{v}_f$ are the solid and fluid velocities, and the fluid and solid stress tensors are correspondingly $\boldsymbol{\sigma}_f$ and $\boldsymbol{\sigma}_s$. On the computational domain boundary simple Dirichlet boundary conditions

$$\boldsymbol{v}_f = \boldsymbol{v}_{\partial\Omega}(t)$$

for the velocity are prescribed. The interaction between the fluid and solid phases is established on the fluid-structure interface Γ_i through the kinematic no-slip boundary condition

$$\boldsymbol{v}_f = \boldsymbol{v}_s \qquad \text{on } \Gamma_i, \tag{4.3}$$

and the dynamic force balance condition, neglecting surface tension, gives

$$\boldsymbol{\sigma}_f \cdot \boldsymbol{n} = \boldsymbol{\sigma}_s \cdot \boldsymbol{n} \qquad \text{on} \quad \Gamma_i. \tag{4.4}$$

The viscous Newtonian stress is defined as

$$\boldsymbol{\sigma}_f = -p_f \mathbb{I} + 2\nu_f \mathbb{D}[\boldsymbol{v}_f], \tag{4.5}$$

where p_f and ν_f are the fluid pressure and nondimensional kinematic viscosity respectively, and $\mathbb{D}[\boldsymbol{v}]$ is the velocity rate of strain $\mathbb{D}[\cdot] = \frac{1}{2}[\boldsymbol{\nabla}(\cdot) + \boldsymbol{\nabla}^T(\cdot)]$.

We assume the solid stress to have the following structure:

$$\boldsymbol{\sigma}_s = -p_s \mathbb{I} + \boldsymbol{\sigma}_\nu(\boldsymbol{v}_s) + \boldsymbol{\sigma}_\tau(\mathbb{F}). \tag{4.6}$$

Here, p_s is the solid pressure, $\boldsymbol{\sigma}_\nu = 2\nu_s \mathbb{D}[\boldsymbol{v}_s]$ is the viscous part of the stress, ν_s is the corresponding viscosity in the solid, assumed for now equal to ν_f, and $\boldsymbol{\sigma}_\tau(\mathbb{F})$ is the elastic part of the stress.

The elastic part $\boldsymbol{\sigma}_\tau(\mathbb{F})$ is defined as a function of the deformation gradient tensor $[\mathbb{F}]_{ij} = F_{ij}$ via the strain energy density function W, [Bower, 2009]:

$$[\boldsymbol{\sigma}_\tau(\mathbb{F})]_{ij} = \frac{1}{J} F_{ik} \frac{\partial W}{\partial F_{kj}}. \tag{4.7}$$

The deformation gradient tensor $\mathbb{F}$ is a characteristic of the local material deformation that connects the reference material configuration with the current material deformation through the expression $d\boldsymbol{x} = \mathbb{F} d\boldsymbol{X} = \frac{\partial \boldsymbol{x}}{\partial \boldsymbol{X}} d\boldsymbol{X}$, which implies

$$\mathbb{F} = \frac{\partial \boldsymbol{x}}{\partial \boldsymbol{X}}. \tag{4.8}$$

The present formulation does not restrict the choice for the constitutive relation for $\boldsymbol{\sigma}_\tau$. In our simulations presented later, we use the simplest Neo-Hookean hyperelastic solid stress in the form

$$\boldsymbol{\sigma}_\tau = G(\mathbb{F}\mathbb{F}^T - \mathbb{I}), \tag{4.9}$$

where G is called the modulus of transverse elasticity. For incompressible deformations the

following relation holds at all times

$$J = det(\mathbb{F}) = 1, \tag{4.10}$$

which, being defined through displacements, is the most often used incompressibility constraint in the case of solids, in place of $\boldsymbol{\nabla \cdot v}_s = 0$.

4.2 Numerical scheme

4.2.1 Derivation

In order to derive a combined weak formulation on Ω, we introduce a common continuous velocity field $\boldsymbol{v}$ for the fluid and solid, that is defined in the whole computational domain. Additionally, we introduce the characteristic function of the fluid domain

$$\chi_f(\boldsymbol{x}, t) = \begin{cases} 1 & \boldsymbol{x} \in \Omega_f(t), \\ 0 & \boldsymbol{x} \in \Omega_s(t), \end{cases} \tag{4.11}$$

and the characteristic function of the solid domain $\chi_s(\boldsymbol{x}, t) = 1 - \chi_f(\boldsymbol{x}, t)$. With the characteristic functions defined this way, the Cauchy stress tensor in the entire domain Ω can be written as

$$\boldsymbol{\sigma} = \chi_f \boldsymbol{\sigma}_f + \chi_s \boldsymbol{\sigma}_s. \tag{4.12}$$

Such notation allows us to reformulate problem (4.1)–(4.6) as follows:

$$\frac{D\boldsymbol{v}}{Dt} = \boldsymbol{\nabla \cdot \sigma} \qquad \text{in } \Omega, \tag{4.13}$$

$$\boldsymbol{\nabla \cdot v} = 0 \qquad \text{in } \Omega, \tag{4.14}$$

$$\boldsymbol{\sigma}_f \boldsymbol{\cdot n} = \boldsymbol{\sigma}_s \boldsymbol{\cdot n} \qquad \text{on } \Gamma_i. \tag{4.15}$$

Requiring a common continuous velocity field in Ω, we strongly enforce the kinematic boundary condition (4.3) on Γ_i.

Now, we define a combined trial velocity space and the corresponding test space:

$$\boldsymbol{V} = \{\boldsymbol{v} |\ \boldsymbol{v} \in [\boldsymbol{H}^1(\Omega)]^d;\ \boldsymbol{v} = \boldsymbol{v}_{\partial\Omega} \text{ on } \partial\Omega\}$$

and

$$\boldsymbol{V}_0 = \{\boldsymbol{\varphi} |\ \boldsymbol{\varphi} \in [\boldsymbol{H}^1(\Omega)]^d;\ \boldsymbol{\varphi} = 0 \text{ on } \partial\Omega\}.$$

together with the usual $\boldsymbol{L}^2(\Omega)$ inner products

$$(\boldsymbol{g}, \boldsymbol{h})_\Omega = \int_\Omega \boldsymbol{g}\cdot\boldsymbol{h}\ d\Omega \quad \text{and} \quad (\mathbb{A}, \mathbb{B})_\Omega = \int_\Omega \mathbb{A} : \mathbb{B}\ d\Omega, \tag{4.16}$$

for vectors $\boldsymbol{g}$ and $\boldsymbol{h}$, as well as for tensors $\mathbb{A}$ and $\mathbb{B}$.

The variational formulation of the combined momentum equation is obtained by multiplying (4.13) with a test function from the test space $\boldsymbol{V}_0$, and integrating by parts over Ω:

$$\left(\frac{D\boldsymbol{v}}{Dt}, \boldsymbol{\varphi}\right)_\Omega = \int_{\Gamma_i} \boldsymbol{\varphi}\cdot(\boldsymbol{\sigma}_s - \boldsymbol{\sigma}_f)\cdot\boldsymbol{n}\ \partial S - (\boldsymbol{\sigma}, \boldsymbol{\nabla}\boldsymbol{\varphi})_\Omega\,, \text{ for all } \boldsymbol{\varphi} \in \boldsymbol{V}_0; \tag{4.17}$$

together with the weak formulation for the incompressibility constraint (4.14),

$$(q, \boldsymbol{\nabla}\cdot\boldsymbol{v})_\Omega = 0, \text{ for all } q \in \boldsymbol{L}^2(\Omega). \tag{4.18}$$

These two equations represent a weak formulation for the combined system (4.13)–(4.14).

The stress jump in the normal direction across Γ_i is still present in the equation (4.17) in the form of the surface integral

$$\int_{\Gamma_i} \boldsymbol{\varphi}\cdot(\boldsymbol{\sigma}_s - \boldsymbol{\sigma}_f)\cdot\boldsymbol{n}\ \partial S. \tag{4.19}$$

Eliminating this integral term in (4.17) causes the dynamic boundary condition, (4.15), that prescribes normal stress continuity, implicit in the combined weak formulation of the FSI problem (4.1)–(4.6):

$$\begin{aligned} \left(\frac{D\boldsymbol{v}}{Dt}, \boldsymbol{\varphi}\right)_\Omega &= -(\boldsymbol{\sigma}, \boldsymbol{\nabla}\boldsymbol{\varphi})_\Omega\,, \text{ for all } \boldsymbol{\varphi} \in \boldsymbol{V}_0 \\ (q, \boldsymbol{\nabla}\cdot\boldsymbol{v})_\Omega &= 0, \text{ for all } q \in L^2(\Omega). \end{aligned} \tag{4.20}$$

Recalling the definitions of the stress tensors $\boldsymbol{\sigma}_f$ and $\boldsymbol{\sigma}_s$, equation (4.20) can be rewritten

as:

$$\left(\frac{D\boldsymbol{v}}{Dt}, \boldsymbol{\varphi}\right)_{\Omega} = (p, \boldsymbol{\nabla}\cdot\boldsymbol{\varphi})_{\Omega} - 2\nu\,(\mathbb{D}[\boldsymbol{v}], \boldsymbol{\nabla}\boldsymbol{\varphi})_{\Omega} - (\chi_s\boldsymbol{\sigma}_{\tau}, \boldsymbol{\nabla}\boldsymbol{\varphi})_{\Omega}\,, \tag{4.21}$$

where p can be regarded as a Lagrange multiplier enforcing the incompressibility constraint $(q, \boldsymbol{\nabla}\cdot\boldsymbol{v})_{\Omega} = 0$ in Ω.

Structure model

One of the advantages of an Eulerian framework is that it naturally allows for the spatial discretization of the fluid governing equations on fixed grids. When modeling fluid flows, we are interested in finding the fluid velocity and pressure distribution within the computational domain. Therefore, using grids such that the velocity and pressure are defined on fixed nodes is convenient.

In contrast, the dynamics of solids is more convenient to describe in a Lagrangian framework. At each time step, a Lagrangian mesh provides information about current solid deformation with respect to the reference configuration as well as the solid stresses; these two quantities are the main goals of solid simulations.

In our formulation we combine the advantages of both approaches using a fixed Eulerian mesh $\mathcal{G}$ on Ω for resolving combined velocity and pressure fields, and using a Lagrangian mesh $\mathcal{G}_s(t)$ for tracking the solid deformation of $\Omega_s(t)$ and for computing the elastic part of the solid stress $\boldsymbol{\sigma}_{\tau}(\mathbb{F})$.

The position of a point $\boldsymbol{x}(\boldsymbol{X}, t) \in \mathcal{G}_s(t)$ is given by a solution to equation

$$\frac{\partial \boldsymbol{x}(\boldsymbol{X}, t)}{\partial t} = \boldsymbol{v}(\boldsymbol{x}(\boldsymbol{X}, t), t), \tag{4.22}$$

where $\boldsymbol{v}(\boldsymbol{x}, t)$ is a local velocity at point $\boldsymbol{x}$, and $\boldsymbol{X}$ is the Lagrangian coordinate of $\boldsymbol{x}$ in the reference configuration. The displacement in the Lagrangian description is therefore defined as $\boldsymbol{u}(\boldsymbol{X}, t) = \boldsymbol{x}(\boldsymbol{X}, t) - \boldsymbol{X}$. On a discrete level, $\boldsymbol{v}(\boldsymbol{x}, t)$ on $\mathcal{G}_s$ is found by interpolating solution from the nodes on the Eulerian grid $\mathcal{G}$ at point $\boldsymbol{x}$.

The elastic component of the solid stress $\boldsymbol{\sigma}_{\tau}(\mathbb{F})$ is computed on $\mathcal{G}_s$ with isoparametric finite element interpolation. In order to compute the deformation gradient tensor $\mathbb{F}$ we consider the following: on a point $\boldsymbol{x}(\boldsymbol{X}, t) \in \mathcal{G}_s$ the deformation gradient tensor with

respect to the reference configuration $\hat{\mathcal{G}}_s = \mathcal{G}_s(0)$ is given as

$$\mathbb{F}(\boldsymbol{x}(\boldsymbol{X},t)) = \frac{\partial \boldsymbol{x}}{\partial \boldsymbol{X}} = \frac{\partial \boldsymbol{x}}{\partial \hat{\boldsymbol{x}}}\frac{\partial \hat{\boldsymbol{x}}}{\partial \boldsymbol{X}} = \frac{\partial \boldsymbol{x}}{\partial \hat{\boldsymbol{x}}}\left(\frac{\partial \boldsymbol{X}}{\partial \hat{\boldsymbol{x}}}\right)^{-1},$$

where $\boldsymbol{X} \in \hat{\mathcal{G}}_s$, and $\hat{\boldsymbol{x}}$ is the coordinate vector in a reference element for the triangulation $\mathcal{G}_s$ (*e.g.* in a reference triangle or in a reference tetrahedron). In other words, the deformation gradient tensor is a product of the Jacobian matrix at $\boldsymbol{x}(\boldsymbol{X},t)$ computed on an element in $\mathcal{G}_s(t)$ and the inverse of the Jacobian matrix at $\boldsymbol{X}$ computed on the same element in $\hat{\mathcal{G}}_s$. For our simulations we use $\mathbb{P}_2$ finite elements.

The moving solid mesh $\mathcal{G}_s$ overlaps with the grid $\mathcal{G}$ making intersection of elements in the two grids very complex (see Figure 4.2).

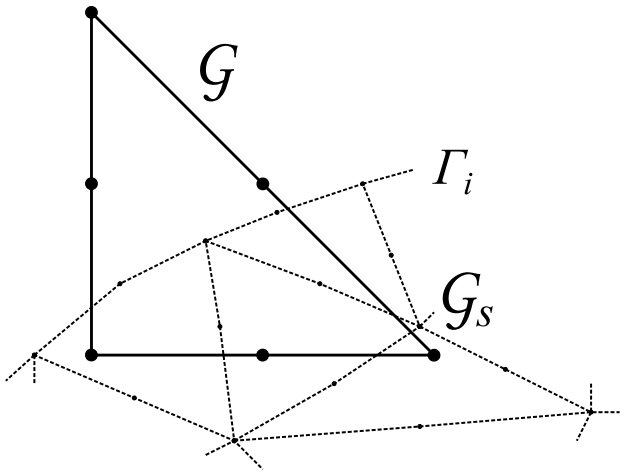

Figure 4.2: Computational domain grid $\mathcal{G}$(solid lines) is overlapped by the Lagrangian grid $\mathcal{G}_s$ (dashed lines). Fluid-structure interface Γ_i is approximated by the Lagrangian grid.

In the standard isoparametric approximation, $\mathbb{F}$, as any other spatial derivative, is discontinuous across element boundaries. This causes significant inconvenience, because the integral

$$(\chi_s \boldsymbol{\sigma}_\tau(\mathbb{F}), \boldsymbol{\nabla}\boldsymbol{\varphi})_\Omega\,, \tag{4.23}$$

where $\boldsymbol{\nabla}\boldsymbol{\varphi}$ and $\boldsymbol{\sigma}_s(\mathbb{F})$ are discontinuous on the Eulerian and Lagrangian grids respectively, essentially becomes a product of two distributions. Numerical approximation of such integrals is a daunting task even in two dimensions, and is prohibitive in three dimensions with two unstructured meshes involved.

We can simplify evaluation of the integral (4.23) by rebuilding a continuous field $\boldsymbol{\sigma}^*_\tau$ on $\mathcal{G}_s$ using a Zienkiewicz-Zhu (ZZ-patch) recovery procedure [Zienkiewicz and Zhu, 1992;

Zienkiewicz et al., 2013]. The idea of the method is to recover nodal values $\tilde{\boldsymbol{\sigma}}_\tau^*$ from the original finite element stress $\boldsymbol{\sigma}_\tau$ sampled within the elements of the finite element discretization $\mathcal{G}_s$, where this stress is well defined. In this way, the integral in (4.23) can be evaluated on the Eulerian mesh $\mathcal{G}$ with element-wise continuous $\boldsymbol{\nabla\varphi}$ and with solid stress $\boldsymbol{\sigma}_\tau^*$, which is interpolated on the Gauss points in $\mathcal{G}$ from the recovered nodal values $\tilde{\boldsymbol{\sigma}}_\tau^*$ on $\mathcal{G}_s$ using

$$\boldsymbol{\sigma}_\tau^*(\boldsymbol{x}_G) = \boldsymbol{N}(\boldsymbol{x}_G)\tilde{\boldsymbol{\sigma}}_\tau^*, \tag{4.24}$$

where $\boldsymbol{x}_G$ is the spatial coordinate of a Gauss point, and $\boldsymbol{N}(\boldsymbol{x}_G)\tilde{\boldsymbol{\sigma}}_\tau^*$ is the standard finite element interpolation within the element in $\mathcal{G}_s$ containing $\boldsymbol{x}_G$. The recovered nodal values $\tilde{\boldsymbol{\sigma}}_\tau^*$ are convenient to define as a matrix with each row storing components of the stress tensor recovered at the corresponding node in the element.

ZZ-patch stress recovery

The recovery procedure involves smoothing of the sampled values of $\boldsymbol{\sigma}_\tau$ by a polynomial of degree equal to the degree of the shape functions in the finite element discretization, with the polynomial being defined within a patch of elements surrounding a single vertex, (see Figure 4.3).

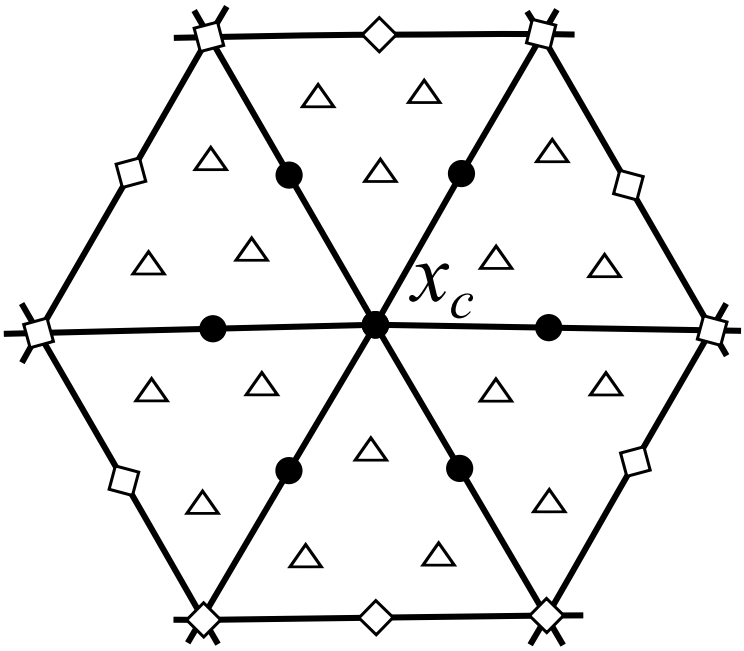

Figure 4.3: Element patch in the ZZ-patch recovery procedure. Illustrated: patch assembly point $\boldsymbol{x}_c$, sampling points ($\triangle$), and nodal values recovered in this patch ($\bullet$).

Thus, for each component $\sigma_\tau^j = [\boldsymbol{\sigma}_\tau]_j$, where the stress tensor is represented as a vector of its components, we write the recovered solution in a patch as

$$[\bar{\boldsymbol{\sigma}}_\tau^*(\boldsymbol{x})]_j = \boldsymbol{p}(\boldsymbol{x})\cdot\boldsymbol{a}_j, \tag{4.25}$$

where $\boldsymbol{p}(\boldsymbol{x}) = [1, \bar{x}, \bar{y}, \bar{x}\bar{y}, \bar{x}^2, \bar{y}^2]$ and $\boldsymbol{a}_j = [a_1, \ldots, a_6]^T$, with $\bar{\boldsymbol{x}} = \boldsymbol{x} - \boldsymbol{x}_c$, and $\boldsymbol{x}_c$ being the patch assembly point.

For each element patch (Figure 4.3), for each component of the stress tensor, a least squares functional with n sampling points is minimized:

$$\mathit{\Pi}_j = \frac{1}{2}\sum_{k=1}^{n}\left[\sigma_\tau^j(\boldsymbol{x}_k) - \boldsymbol{p}_k\cdot\boldsymbol{a}_j\right]^2, \tag{4.26}$$

where $\boldsymbol{p}_k = \boldsymbol{p}(\boldsymbol{x}_k)$.

The vector of polynomial coefficients $\boldsymbol{a}_j$ for each component of the stress tensor is found as a solution to the linear system

$$\mathbb{A}\boldsymbol{a}_j = \boldsymbol{b}_j, \tag{4.27}$$

where

$$\mathbb{A} = \sum_{k=1}^{n}\boldsymbol{p}_k^T\boldsymbol{p}_k \tag{4.28}$$

is the Vandermonde matrix, and

$$\boldsymbol{b}_j = \sum_{k=1}^{n}\boldsymbol{p}_k^T\sigma_\tau^j(\boldsymbol{x}_k). \tag{4.29}$$

The computed $\boldsymbol{a}_j$ are used to recover each component of $\tilde{\boldsymbol{\sigma}}_\tau^*$ at all inner nodes $\bullet$ within the patch, (see Figure 4.3). For example, for some node $\boldsymbol{x}_e$ we recover stress tensor values at this node as

$$[\tilde{\boldsymbol{\sigma}}_\tau^*(\boldsymbol{x}_e)]_j = [\bar{\boldsymbol{\sigma}}_\tau^*(\boldsymbol{x}_e)]_j = \boldsymbol{p}(\boldsymbol{x}_e)\cdot\boldsymbol{a}_j. \tag{4.30}$$

As some nodes (mid-edge nodes) in the $\mathbb{P}_2$ finite element discretization belong to more than one patch, we perform averaging of the multiple nodal values of $\tilde{\boldsymbol{\sigma}}_\tau^*$ computed on different patches.

In two dimensions, for stress sampling we use second order Gaussian quadrature nodes

defined on the reference triangle using barycentric coordinates as

$$(1/6, 1/6, 2/3),$$
$$(2/3, 1/6, 1/6),$$
$$(1/6, 2/3, 1/6).$$

Extension of the ZZ-patch method to three spatial dimensions is straightforward. The interpolation polynomial $\boldsymbol{p}(\boldsymbol{x})$ in this case is defined as a function of $\boldsymbol{x} = (x, y, z)$, and is given by $\boldsymbol{p}(\boldsymbol{x}) = [1, x, y, z, xy, xz, yz, x^2, y^2, z^2]$. The sampling over a tetrahedron is performed using nodes of the symmetric, third order, five-point Gaussian quadrature.

Transfer of the elastic stress forces

The evaluation of (4.23), requires a consistent and accurate transfer of the elastic stress forces onto the Eulerian discretization space. We achieve this using the force-projection method [Zhao et al., 2008], proposed for the case when the elastic stress is transferred from the Lagrangian grid onto a uniform Cartesian mesh. It can be modified and applied to the present case as well. We propose to use a distributed force $\boldsymbol{\mathcal{F}}$ discretized with the velocity trial space on $\mathcal{G}$, such that

$$(\boldsymbol{\mathcal{F}}, \boldsymbol{\varphi})_{\Omega} = -(\chi_s \boldsymbol{\sigma}_{\tau}, \boldsymbol{\nabla}\boldsymbol{\varphi})_{\Omega}, \tag{4.31}$$

which is a standard Galerkin projection of the solid stress contribution on a global space defined in the entire domain Ω.

Numerical experiments show that $\boldsymbol{\mathcal{F}}$ can be found by inverting the mass matrix on $(\boldsymbol{\sigma}_{\tau}, \boldsymbol{\nabla}\boldsymbol{\varphi})_{\Omega_s}$, while intersected elements integration is performed with high-order Gauss quadratures [Zhang et al., 2009a] in 2-D; or with a regular 5^{th}-order Gauss quadrature for tetrahedra in 3-D.

Now the combined formulation is defined on the entire domain Ω and is given by: find $\boldsymbol{v} \in \boldsymbol{V}$, $p \in \boldsymbol{L}^2(\Omega)$ and $\boldsymbol{\mathcal{F}} \in [\boldsymbol{L}^2(\Omega)]^d$ such that

$$\begin{aligned}
\left(\frac{D\boldsymbol{v}}{Dt}, \boldsymbol{\varphi}\right)_{\Omega} &= (p, \boldsymbol{\nabla}\cdot\boldsymbol{\varphi})_{\Omega} - 2\nu\,(\mathbb{D}[\boldsymbol{v}], \boldsymbol{\nabla}\boldsymbol{\varphi})_{\Omega} + (\boldsymbol{\mathcal{F}}, \boldsymbol{\varphi})_{\Omega}, \\
(\boldsymbol{\mathcal{F}}, \boldsymbol{\varphi})_{\Omega} &= -(\chi_s \boldsymbol{\sigma}_{\tau}, \boldsymbol{\nabla}\boldsymbol{\varphi})_{\Omega}, \\
(q, \boldsymbol{\nabla}\cdot\boldsymbol{v})_{\Omega} &= 0,
\end{aligned} \tag{4.32}$$

for all $q \in \boldsymbol{L}^2(\Omega)$ and $\boldsymbol{\varphi} \in \boldsymbol{V}_0$.

Operator splitting

Convective terms on the left hand side of equation (4.32) are split from the generalized Stokes problem as explained in [Minev and Ross Ethier, 1998] and illustrated in Chapter 2.5.2. The total material derivative can be approximated with the second order backward difference as

$$\left(\frac{D}{Dt}\boldsymbol{v}^{n+1}, \boldsymbol{\varphi}\right)_\Omega \approx \left(\tau_0 \boldsymbol{v}^{n+1} + \tau_1 \tilde{\boldsymbol{v}}^n + \tau_2 \tilde{\boldsymbol{v}}^{n-1}, \boldsymbol{\varphi}\right)_\Omega, \tag{4.33}$$

where $\tau_0 = 3/(2\Delta t)$, $\tau_1 = -2/\Delta t$ and $\tau_2 = 1/(2\Delta t)$. A pointwise characteristic integration of the convective terms is performed, such that $\tilde{\boldsymbol{v}}^n(\boldsymbol{x}) = \boldsymbol{v}(\boldsymbol{Z}(t^n;\boldsymbol{x}), t^n)$ and $\tilde{\boldsymbol{v}}^{n-1}(\boldsymbol{x}) = \boldsymbol{v}(\boldsymbol{Z}(t^{n-1};\boldsymbol{x}), t^{n-1})$ are the velocities from the time levels n and $n-1$, which have been advected alongside an approximation to the characteristics. In this formulation, $\boldsymbol{Z}(t^n;\boldsymbol{x})$ and $\boldsymbol{Z}(t^{n-1};\boldsymbol{x})$ are the solutions to the following terminal-value problem for pure advection equation between t^{n-1} and t^{n+1}:

$$\begin{cases} \dfrac{d\boldsymbol{Z}(s)}{ds} = \boldsymbol{v}(\boldsymbol{Z}(s), s), \\ \boldsymbol{Z}(t^{n+1}) = \boldsymbol{x}, \quad \boldsymbol{x} \in \mathcal{G}, \quad s \in [t^{n-1},\ t^{n+1}]. \end{cases} \tag{4.34}$$

Velocity and pressure are decoupled at each time step with the second order rotational incremental pressure-correction scheme [Guermond et al., 2006]. Thus, the time-discretized scheme (4.32) takes the form

$$\left(\boldsymbol{\mathcal{F}}^{n+1}, \boldsymbol{\varphi}\right)_\Omega = -\left(\chi_s^{n+1}\boldsymbol{\sigma}_\tau^{n+1}, \boldsymbol{\nabla}\boldsymbol{\varphi}\right)_\Omega, \tag{4.35}$$

$$\left(\tau_0 \boldsymbol{v}^*, \boldsymbol{\varphi}\right)_\Omega + 2\nu\left(\mathbb{D}[\boldsymbol{v}^*], \boldsymbol{\nabla}\boldsymbol{\varphi}\right)_\Omega = \left(p^n, \boldsymbol{\nabla}\cdot\boldsymbol{\varphi}\right)_\Omega + \left(\boldsymbol{\mathcal{F}}^{n+1}, \boldsymbol{\varphi}\right)_\Omega - \left(\tau_1\tilde{\boldsymbol{v}}^n + \tau_2\tilde{\boldsymbol{v}}^{n-1}, \boldsymbol{\varphi}\right)_\Omega, \tag{4.36}$$

$$\left(\boldsymbol{\nabla} q, \boldsymbol{\nabla}\phi^{n+1}\right)_\Omega = -\tau_0\left(\boldsymbol{\nabla}\cdot\boldsymbol{v}^*, q\right)_\Omega, \tag{4.37}$$

$$\left(p^{n+1}, q\right)_\Omega = \left(\phi^{n+1} + p^n - \nu\boldsymbol{\nabla}\cdot\boldsymbol{v}^*, q\right)_\Omega, \tag{4.38}$$

$$\tau_0\left(\boldsymbol{v}^{n+1} - \boldsymbol{v}^*, \boldsymbol{\varphi}\right)_\Omega = -\left(\boldsymbol{\nabla}\phi^{n+1}, \boldsymbol{\varphi}\right)_\Omega, \tag{4.39}$$

for all $q \in \boldsymbol{L}^2(\Omega)$ and $\boldsymbol{\varphi} \in \boldsymbol{V}_0$.

With $\boldsymbol{\mathcal{F}}$ taken at t^{n+1}, scheme (4.35)-(4.39) is implicit in velocity due to the coupling between $\boldsymbol{\mathcal{F}}$ and $\boldsymbol{v}$ through equation (4.22). For maximum accuracy and stability, at each time step t^{n+1} the solution of the discrete system (4.35)-(4.39) should be performed iter-

atively, solving for $\boldsymbol{v}^{n+1,k}$ using $\boldsymbol{\mathcal{F}}^{n+1,k-1}$ until reaching the desired convergence, with the initial approximation $\boldsymbol{\mathcal{F}}^{n+1,0} = \boldsymbol{\mathcal{F}}^{n}$.

Treatment of the mixed derivatives

The mixed derivatives term $\left(\boldsymbol{\nabla}^T\boldsymbol{v}, \boldsymbol{\nabla}\boldsymbol{\varphi}\right)_\Omega$ on the left hand side of (4.36) usually is not present in the weak formulation for the Navier-Stokes equations. This term comes from $\boldsymbol{\nabla}^T\boldsymbol{v}$ part of the fluid stress tensor and is commonly omitted since $\boldsymbol{\nabla}\cdot\boldsymbol{\nabla}^T\boldsymbol{v} = \boldsymbol{\nabla}(\boldsymbol{\nabla}\cdot\boldsymbol{v}) = 0$ due to the incompressibility constraint $\boldsymbol{\nabla}\cdot\boldsymbol{v} = 0$. In our formulation we keep this term because it is instrumental for the correct representation of the boundary forces on Γ_i. On the other hand, mixed derivatives introduced by this term couple the different components of the velocity, which makes numerical solution of the problem unnecessarily complicated.

We can avoid coupling of the different components of velocity by using the penalty scheme proposed in [Guermond and Minev, 2013]. First, we present the idea in two space dimensions and then we rewrite equation (4.36) in three dimensions with the second order implementation of the scheme.

Starting from the unsteady Navier-Stokes system:

$$\frac{D\boldsymbol{v}}{Dt} - \nu\boldsymbol{\nabla}\cdot(\boldsymbol{\nabla}\boldsymbol{v} + \boldsymbol{\nabla}^T\boldsymbol{v}) + \boldsymbol{\nabla}p = 0 \qquad \boldsymbol{\nabla}\cdot\boldsymbol{v} = 0. \tag{4.40}$$

Time discretization with the method of characteristics yields

$$\tau_0 v_x^{n+1} + \tau_1\tilde{v}_x^n + \tau_2\tilde{v}_x^{n-1} - \nu\boldsymbol{\nabla}^2 v_x^{n+1} - \nu\partial_{xx}v_x^{n+1} - \nu\partial_{xy}v_y^{n+1} + \partial_x p = 0, \tag{4.41}$$

$$\tau_0 v_y^{n+1} + \tau_1\tilde{v}_y^n + \tau_2\tilde{v}_y^{n-1} - \nu\boldsymbol{\nabla}^2 v_y^{n+1} - \nu\partial_{yy}v_y^{n+1} - \nu\partial_{xy}v_x^{n+1} + \partial_y p = 0. \tag{4.42}$$

The second order version of the scheme is as follows:

$$\tau_0 v_x^{n+1} + \tau_1\tilde{v}_x^n + \tau_2\tilde{v}_x^{n-1} - \nu\boldsymbol{\nabla}^2 v_x^{n+1} - \nu\partial_{xx}v_x^{n+1} - \nu\partial_{xx}(v_x^{n+1} - v_x^e) + \partial_x p = \nu\partial_{xy}v_y^e, \tag{4.43}$$

$$\tau_0 v_y^{n+1} + \tau_1\tilde{v}_y^n + \tau_2\tilde{v}_y^{n-1} - \nu\boldsymbol{\nabla}^2 v_y^{n+1} - \nu\partial_{yy}v_y^{n+1} - \nu\partial_{yy}(v_y^{n+1} - v_y^e) + \partial_y p = \nu\partial_{xy}v_x^e, \tag{4.44}$$

where $\boldsymbol{v}^e = 2\boldsymbol{v}^n - \boldsymbol{v}^{n-1}$ is a second order extrapolation of velocity $\boldsymbol{v}^{n+1}$.

Implementing this idea in the weak formulation (4.35)-(4.39) we obtain:

$$\left(\boldsymbol{\mathcal{F}}^{n+1},\boldsymbol{\varphi}\right)_\Omega = -\left(\chi_s^{n+1}\boldsymbol{\sigma}_\tau^{n+1},\boldsymbol{\nabla}\boldsymbol{\varphi}\right)_\Omega, \tag{4.45}$$

$$\begin{aligned}(\tau_0\boldsymbol{v}^*,\boldsymbol{\varphi})_\Omega + \nu\left(\boldsymbol{\nabla}\boldsymbol{v}^*,\boldsymbol{\nabla}\boldsymbol{\varphi}\right)_\Omega + 2\nu\sum_{i=1}^{3}\left(\partial_i v_i^{n+1},\partial_i\varphi_i\right)_\Omega = \\ = (p^n,\boldsymbol{\nabla}\cdot\boldsymbol{\varphi})_\Omega + \left(\boldsymbol{\mathcal{F}}^{n+1},\boldsymbol{\varphi}\right)_\Omega - \left(\tau_1\tilde{\boldsymbol{v}}^n + \tau_2\tilde{\boldsymbol{v}}^{n-1},\boldsymbol{\varphi}\right)_\Omega + \\ + \nu\left(\partial_x v_x^e - \partial_y v_y^e - \partial_z v_z^e,\partial_x\varphi_x\right)_\Omega + \\ + \nu\left(\partial_y v_y^e - \partial_x v_x^e - \partial_z v_z^e,\partial_y\varphi_y\right)_\Omega + \\ + \nu\left(\partial_z v_z^e - \partial_x v_x^e - \partial_y v_y^e,\partial_z\varphi_z\right)_\Omega,\end{aligned} \tag{4.46}$$

$$\left(\boldsymbol{\nabla}q,\boldsymbol{\nabla}\phi^{n+1}\right)_\Omega = -\tau_0\left(\boldsymbol{\nabla}\cdot\boldsymbol{v}^*,q\right)_\Omega, \tag{4.47}$$

$$\left(p^{n+1},q\right)_\Omega = \left(\phi^{n+1} + p^n - \nu\boldsymbol{\nabla}\cdot\boldsymbol{v}^*,q\right)_\Omega, \tag{4.48}$$

$$\tau_0\left(\boldsymbol{v}^{n+1} - \boldsymbol{v}^*,\boldsymbol{\varphi}\right)_\Omega = -\left(\boldsymbol{\nabla}\phi^{n+1},\boldsymbol{\varphi}\right)_\Omega, \tag{4.49}$$

for all $q \in \boldsymbol{L}^2(\Omega)$ and $\boldsymbol{\varphi} \in \boldsymbol{V}_0$.

Scheme (4.45)-(4.49), when discretized in space with finite elements, produces sparse linear systems with symmetric positive definite matrices independent of time, that can be computed once at the beginning of time-stepping. The preconditioned conjugate gradient method is used for solving the linear systems, along with incomplete Cholesky decomposition algorithm used for preconditioning. In our simulations, a standard $\mathbb{P}_2 - \mathbb{P}_1$ spatial finite element approximation is adopted on the grid $\mathcal{G}$.

4.2.2 Extension to variable density and viscosity

In order to include fluids and solids having different densities and viscosities, we first introduce the following notation:

$$\rho(\boldsymbol{x},t) = \chi_f(\boldsymbol{x},t)\rho_f + \chi_s(\boldsymbol{x},t)\rho_s \quad \text{and} \quad \mu(\boldsymbol{x},t) = \chi_f(\boldsymbol{x},t)\mu_f + \chi_s(\boldsymbol{x},t)\mu_s \tag{4.50}$$

and

$$\hat{\boldsymbol{\mathcal{F}}}(\boldsymbol{x},t) = \boldsymbol{\nabla}\cdot(\chi_s(\boldsymbol{x},t)\boldsymbol{\sigma}_\tau(\boldsymbol{x},t)). \tag{4.51}$$

Since the advection terms in the Navier-Stokes equations can be discretized in a straightforward way explicitly, it is sufficient to restrict ourselves to the governing equations in the

form of the generalized Stokes problem. Using the notation above,

$$\rho\frac{\partial \boldsymbol{v}}{\partial t} = -\boldsymbol{\nabla} p + \boldsymbol{\nabla}\cdot(2\mu\mathbb{D}[\boldsymbol{v}]) + \hat{\boldsymbol{\mathcal{F}}}, \quad \boldsymbol{\nabla}\cdot\boldsymbol{v} = 0 \quad \text{in } \Omega. \tag{4.52}$$

Denoting the divided differences as $\delta_t a^n = (a^n - a^{n-1})/\Delta t$ we can state the following first order approximation to the system (4.52):

$$\gamma\delta_t \boldsymbol{v}^{n+1} - 2\sigma\boldsymbol{\nabla}\cdot\mathbb{D}[\boldsymbol{v}^{n+1}] = (\gamma - \rho^n)\delta_t\boldsymbol{v}^n + \boldsymbol{\nabla}\cdot(2(\mu^{n+1} - \sigma)\mathbb{D}[\boldsymbol{v}^n]) - \boldsymbol{\nabla} p^n + \hat{\boldsymbol{\mathcal{F}}}^{n+1}, \tag{4.53}$$

$$\boldsymbol{\nabla}^2\phi^{n+1} = \frac{\check{\rho}}{\Delta t}\boldsymbol{\nabla}\cdot\boldsymbol{v}^{n+1} \qquad \left.\frac{\partial\phi^{n+1}}{\partial \boldsymbol{n}}\right|_{\partial\Omega} = 0, \tag{4.54}$$

where γ, $\check{\rho}$, and σ are the positive constants, such that for all $(\boldsymbol{x}, t) \in \Omega\times[0, T]$ holds $\check{\rho} \le \rho(\boldsymbol{x}, t) \le \gamma$ and $0.5\mu(\boldsymbol{x}, t) \le \sigma$. Unconditional stability and optimal convergence of the scheme can be shown for the unsteady Stokes equations, *i.e.* without the hyperelastic part of the stress, [Guermond and Salgado, 2009; Guermond and Minev, 2013].

4.3 Numerical experiments

4.3.1 Deformation of an elastic wall driven by a time-dependent flow

In this numerical experiment we simulate deformation of an elastic wall by a time-dependent fluid flow prescribed at one of the boundaries in a periodic domain. The computational domain is 1 by 1 square with the lower half of the domain occupied by solid and the upper half filled with the fluid; see Figure 4.4 for the schematics of the setup geometry.

At $y = 0$, zero velocity is prescribed. At the top boundary, $y = 1$, the periodic in time Dirichlet velocity is prescribed as

$$v_x = 0, \quad v_y = -(1 - \cos(2\pi t))\sin(2\pi x). \tag{4.55}$$

Periodic boundary conditions are prescribed at $x = 0$ and $x = 1$. The fluid and solid viscosities are given by $\nu = \nu_f = \nu_s = 10^{-2}$, and the coefficient G in front of the elastic part of the solid stress tensor $\boldsymbol{\sigma}_\tau = G(\mathbb{F}\mathbb{F}^T - \mathbb{I})$ is set to $G = 0.25$.

In Figure 4.5 we present the fluid velocity and solid deformation at $t = 1$. The results compare well with the simulations reported in [Zhao et al., 2008].

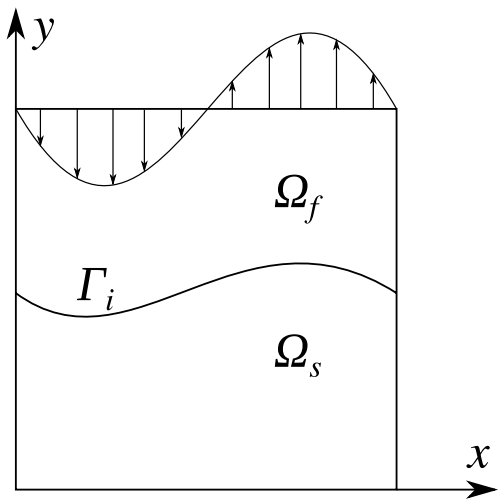

Figure 4.4: Schematics of the elastic wall driven by a time-dependent flow.

4.3.2 Solid motion in a lid driven cavity

Another well validated result we would like to try is the dynamics of a soft solid deforming in a lid driven cavity. In order to compare our results, we use the same parameters and geometry as has been reported previously by [Zhao et al., 2008; Sugiyama et al., 2011]. The cavity is a 1×1 square filled with a fluid at rest. A neutrally buoyant disc with a radius 0.2 is placed at (0.6,0.5), (see Figure 4.6a). The no-slip boundary conditions are prescribed at the domain boundary $x = 0$, $x = 1$, and $y = 0$. At $t = 0$ the lid ($y = 1$) starts to move at a constant speed $v_x = 1$ in the positive x direction. The material properties are set as follows: fluid and solid viscosities $\nu = \nu_f = \nu_s = 10^{-2}$, and the modulus of transverse elasticity $G = 0.1$.

The simulation results demonstrating particle deformation and instantaneous streamlines in the fluid at different time steps on the interval $t \in [0, 8.20]$ are presented in Figure 4.6. For times $t = 4.69$ and $t = 8.20$ we compare our solid deformation to the results reported elsewhere; see Figure 4.6e and 4.6h, and note the bold gray line outlining the solid boundary as reported by [Zhao et al., 2008].

4.3.3 Three-dimensional fluid flow induced by a rhythmically expanding pulmonary alveolus

As an illustration of the ability of the method to resolve complex flow patterns in the respiratory system, we present a proof of concept simulation of a three dimensional alveolated

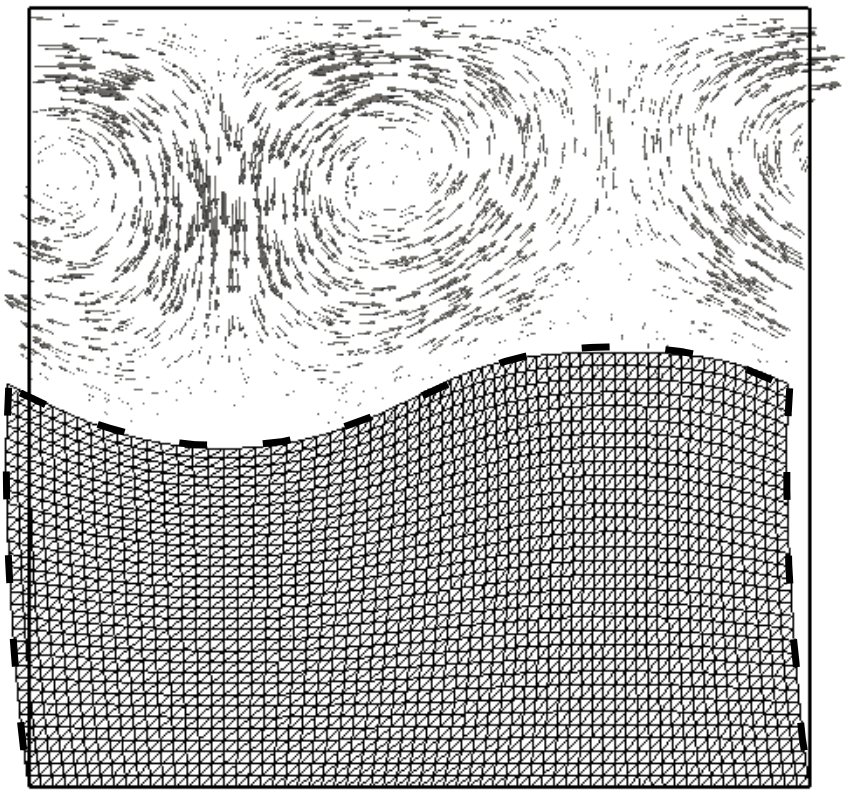

Figure 4.5: Visualization of the fluid velocity field and solid deformation at $t = 1$. Dashed bold line is the solid boundary as reported in [Zhao et al., 2008].

duct with a rhythmically expanding alveolus. Previous simulations by [Henry et al., 2012] and [Sznitman, 2013] have been performed based on the assumption of geometrically self-similar expansion of the lungs. Therefore, geometrical models used in these studies were designed in such a way, that the entire geometry – the duct and the attached alveolus – were expanding and contracting according to a prescribed sinusoidal law remaining self-similar at all times.

It is also known that the resulting alveolar flow patterns depend on Q_a/Q_d, where Q_a is the flow rate of air entering the alveolus, and Q_d is the ductal flow rate measured at the inlet [Sznitman et al., 2007]. The flow rate ratio is dependent on the alveolar generation number z' (see Table 1.1), which also determines the airway dimensions and parameters of the fluid flow.

Acinar micro-flows exhibit two major flow patterns: a recirculation flow due to viscous shear transferred from the ductal region, and a radial flow due to alveolar wall expansion, (see Figure 4.10). Further down the airway tree, the relative importance of the radial flow

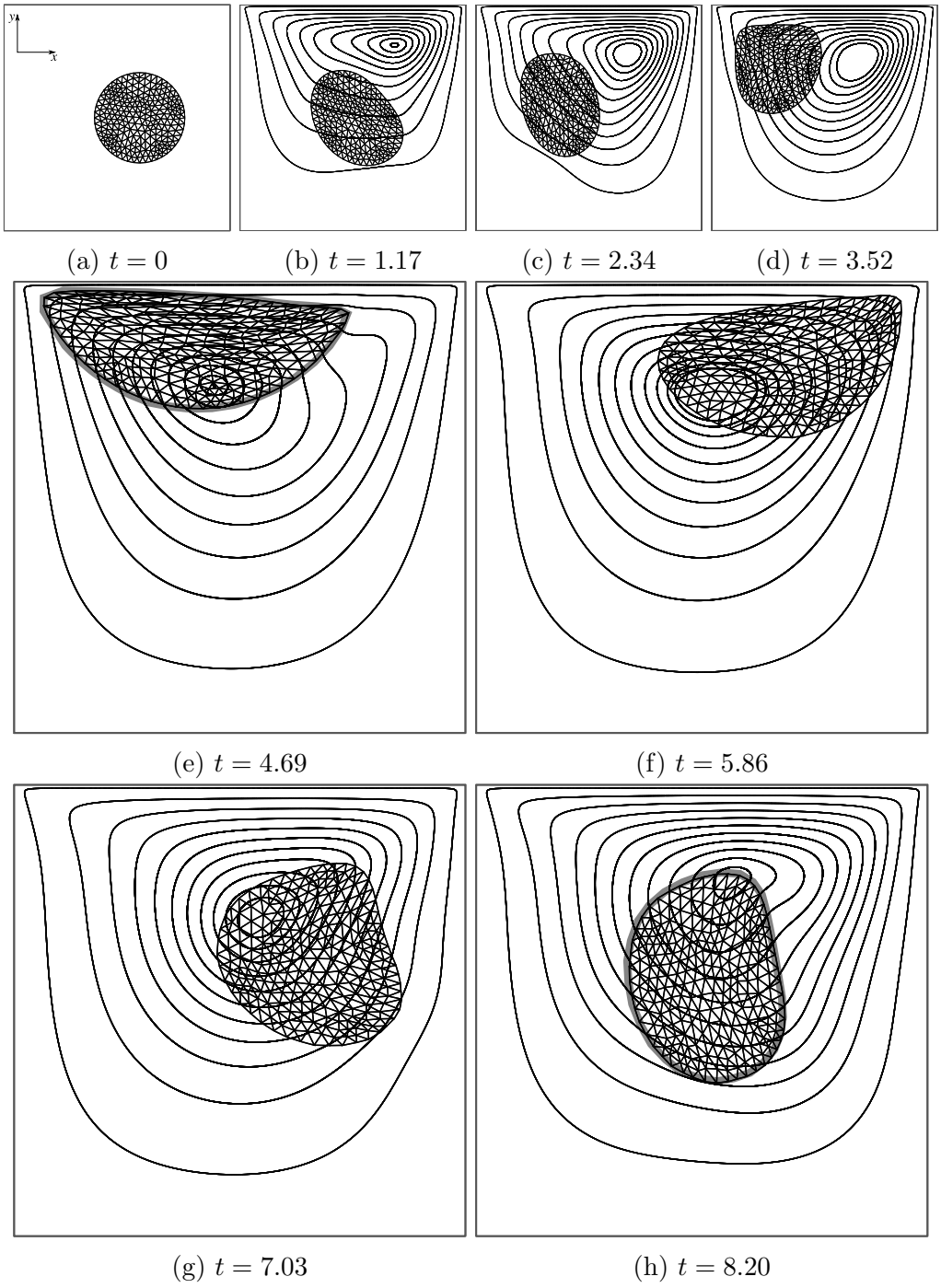

(a) $t = 0$ (b) $t = 1.17$ (c) $t = 2.34$ (d) $t = 3.52$

(e) $t = 4.69$ (f) $t = 5.86$

(g) $t = 7.03$ (h) $t = 8.20$

Figure 4.6: Streamlines and solid deformation in a lid driven cavity. For two time instances $t = 4.69$ and $t = 8.20$ we include solid boundary reported in [Zhao et al., 2008], the boundary is outlined using a thick gray line.

increases as the ratio Q_a/Q_d grows with each acinar generation z', until the recirculation flow is completely dominated by the alveolar wall movement starting at generation $z' = 6$ as reported in [Sznitman et al., 2007].

Our geometrical model consists of a rigid cylindrical duct and elastic alveolus attached to it, see (Figure 4.7). The geometrical parameters follow the geometrical description of the pulmonary acinus from [Sznitman et al., 2007] for comparative purposes, and are presented in Table 4.1.

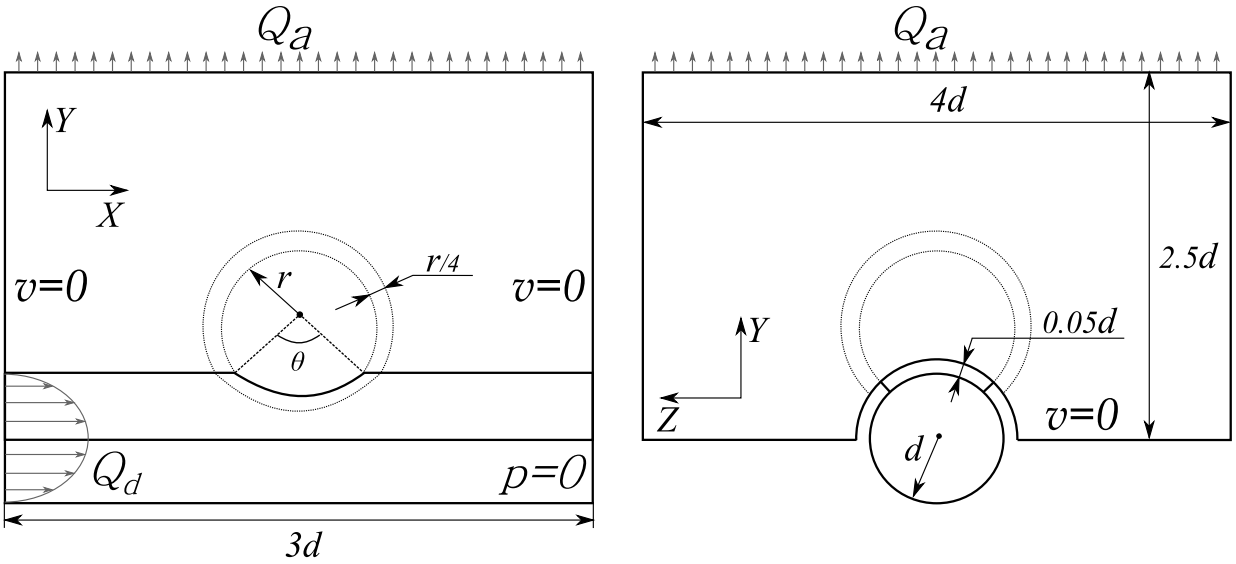

Figure 4.7: Geometry of the idealized alveolar duct. Refer to Table 4.1 for the specific values of the two configurations studied.

	d(mm)	r(mm)	θ	$V'(m/s)$	$T(s)$	Q_a/Q_d	$1/\nu$	G	Δt
$z' = 6$	0.27	0.19	120°	$6.6{\cdot}10^{-3}$	3	0.02142	0.1075	50	10^{-2}
$z' = 8$	0.23	0.217	120°	$1.2{\cdot}10^{-3}$	3	0.2425	0.01662	50	10^{-3}

Table 4.1: Geometrical and numerical parameters for the idealized alveolar duct simulations.

Since the numerical method is designed for simulations on fixed grids, special considerations have to be given for the computational mesh $\mathcal{G}$. For present simulations it is designed to consist of a cylindrical duct having rigid side walls with an opening for the alveolar mouth, and a box attached at the alveolar opening with Dirichlet surface $\partial\Omega_{top}$ at the top and rigid walls on the sides and at the bottom, (see Figure 4.7 and 4.8). The alveolus wall grid $\mathcal{G}_s$ is a sphere segment cut to fit the outside of the duct wall boundary, (see Figure 4.9).

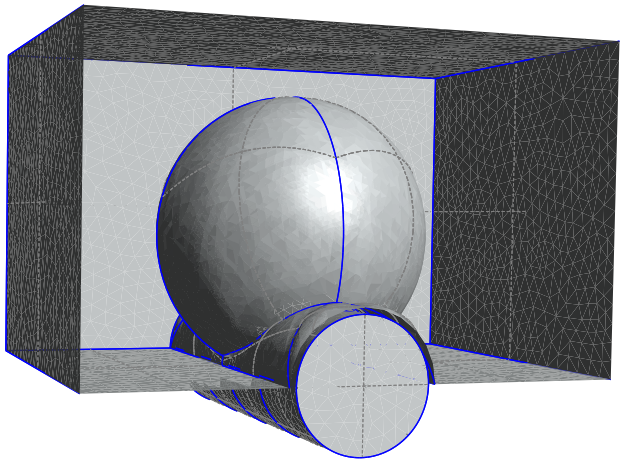

Figure 4.8: Boundary of the computational grid $\mathcal{G}$ for FSI simulations with the frontal surface of the top box removed. Alveolus is placed for illustration only, separate Lagrangian grid $\mathcal{G}_s$ is used for the solid domain, (see Figure 4.9).

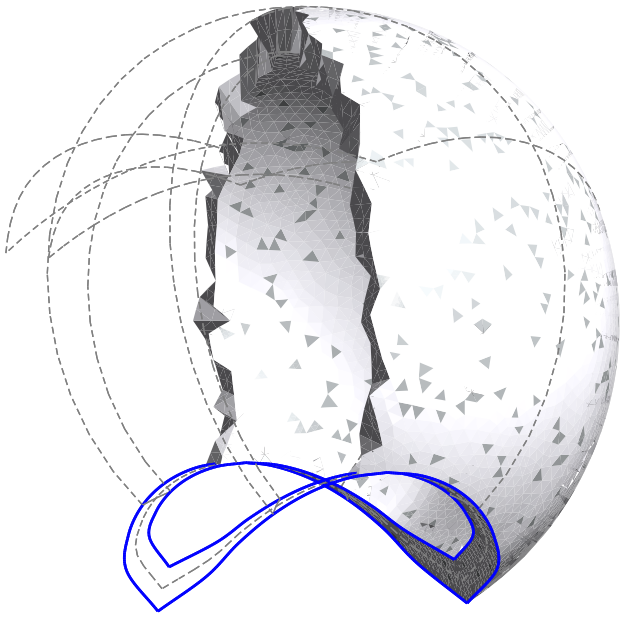

Figure 4.9: Solid grid $\mathcal{G}_s$ representing alveolar wall.

A time dependent parabolic velocity profile is prescribed at the inlet boundary. The magnitude of the prescribed velocity is given by $v_{max}(t) = V' \sin(\frac{2\pi}{T}t)$. A standard outlet boundary condition with constant pressure $p = 0$ is set at the other end of the cylindrical duct. The Dirichlet surface $\partial\Omega_{top}$ is used to prescribe a proper time-dependent volumetric flow rate through the alveolar opening in order to keep the Q_a/Q_d ratio constant during

the simulations. A uniform time-dependent velocity profile is prescribed at $\partial\Omega_{top}$, with the magnitude computed according to the formula $v_{top} = Q_d(Q_a/Q_d)/A_{top}$, where Q_d is the ductal volumetric flow rate, and A_{top} is the $\partial\Omega_{top}$ area.

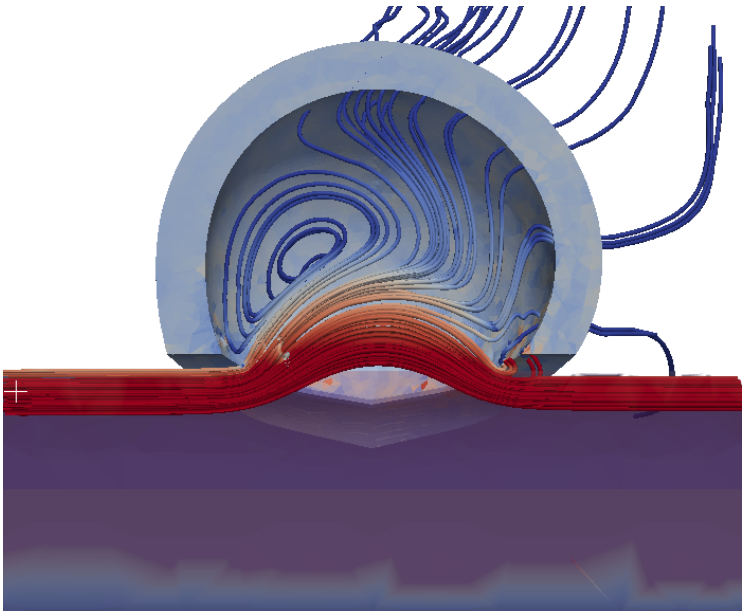

Figure 4.10: Instantaneous alveolar streamlines at maximum inspiration. Geometry and the fluid flow parameters correspond to the acinar generation $z' = 6$ in [Sznitman et al., 2007]. The recirculation region is seen on the left side of the alveolus, the radial flow due to alveolar expansion is on the right.

The simulations were performed for two alveolar generations $z' = 6$ and $z' = 8$. The instantaneous streamlines in the fluid at the maximum inspiration for both generations are presented at Figures 4.10 and 4.11. Qualitatively, these results match the simulations performed by [Sznitman et al., 2007; Henry et al., 2012], with some differences, probably, due to completely different approaches for resolving fluid-structure interaction. Similarly to what has already been reported, our results show that at $z' = 8$ the alveolus flow has no recirculation region and is completely dominated by the alveolar wall motion, (see Figure 4.11). For $z' = 6$ we can still see two distinct flow regions in the alveolus, the recirculation region and the region with streamlines following the wall, (see Figure 4.10). This is different from what is observed in [Sznitman et al., 2007], who report that starting from $z' = 6$ they do not observe the recirculation region anymore.

The apparent difference is caused by the nonuniform dynamics of the alveolar wall, which we do not control in our simulations. Due to hydrodynamic pressure, the distal (further downstream) portion of the alveolar wall moves and expands more readily than

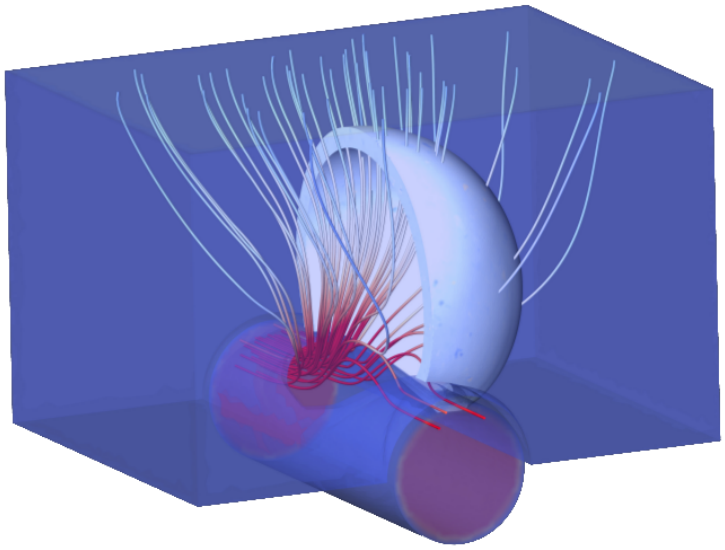

Figure 4.11: Instantaneous alveolar streamlines at maximum inspiration. Geometry and the fluid flow parameters correspond to the acinar generation $z' = 8$ in [Sznitman et al., 2007]. The flow in the alveolus is completely dominated by the alveolar wall expansion.

the proximal side of the wall. In our view, this slower wall motion allows formation of the recirculation region, which would not happen if the expansion was prescribed and uniform as in [Sznitman et al., 2007; Henry et al., 2012].

Chapter 5

Conclusion

The work described in this thesis presents new numerical approaches for solving problems involving fluid-solid and fluid-elastic body interactions in biological systems with the focus on aspects of fibrous particle deposition in the distal airways of the human lung.

In order to perform efficient and accurate resolution of the fluid flow around an elongated solid of complex shape and to address the issue of different spatial scales associated with the problem of micro-particle transport in the lungs, we introduce a new Rotating Grid Procedure (RGP) which is based on two grids accommodating different scales, and on the Fictitious Domain Method (FDM) for particulate flows. This technique employs a macro-grid $\mathcal{G}_H$ with the mesh size H for resolving the macro-scale flow, and a micro-scale grid $\mathcal{G}_h$ with the grid size $h \ll H$ for accurate resolution of the flow around the micro-particle. The efficiency of the RGP is achieved by fixing the micro-grid with the fiber in its spatial motion. Then, the original problem on a moving grid is reformulated using the ALE method, yielding a problem formulation on the fixed reference micro-grid. As such, the problem is discretized on the reference micro-grid using finite elements, resulting in matrices independent of time, which can be precomputed before the first time step. The solid motion of the particle is resolved with the FDM on the micro-grid, which can be designed to fit a complex particle shape, thus improving the accuracy of the micro-grid integration within the particle volume.

The RGP is used to study local deposition enhancement due to magnetic field alignment for ellipsoid particles in a small airway bifurcation. Our results suggest that magnetic alignment of high-aspect ratio particles (length to diameter ratio 20 or more) could help in the development of new targeted drug delivery approaches to aerosol medicine.

In another study, we used RGP to find that the micro-fibers aligned with the shear plane (plane perpendicular to the local fluid vorticity) in a linear shear flow may gain a

significant inclination to the shear plane in a relatively short time. Additionally, our results show that particles with complex geometries exhibit rotational behavior in shear flows, which is different from that occurring for straight ellipsoids or cylinders. Such behavior may be a reason for higher respiratory tract deposition for fibers with complex shapes than that seen with simple fiber shapes, due to enhanced interception caused by a combination of transverse motion and more frequent flipping.

A finite element method utilizing mixed Eulerian and Lagrangian approach is developed for direct numerical simulations of dynamical interaction between a Newtonian fluid and a hyper-elastic solid. A combined velocity field for fluid and solid is introduced over the entire computational domain, and a weak formulation for the combined fluid-solid system is derived in an Eulerian framework. The problem for the combined velocity field is then solved using the finite element method with operator splitting that allows time independent matrices for the velocity and pressure operators.

The solid deformation is tracked on a Lagrangian grid, where the solid stresses are computed using finite element interpolation. The solid stresses are smoothed on the Lagrangian grid with the ZZ-patch recovery method and are transferred on the Eulerian grid as a distributed force using the force-projection method.

Numerical experiments in two spatial dimensions show good qualitative agreement with the numerical results reported in the literature. In three dimensions, a computational model of an alveolated duct with a single expandable alveolus is simulated. The computed flow patterns suggest that the developed numerical method is capable of resolving fluid-structure interaction in complex 3-D configurations with the results in good agreement with those obtained with different numerical methods and computational models.

5.1 Summary

Recapitulating, this thesis has resulted in the following contributions.

- A brief overview of the idealized respiratory system morphologies and review of the different modeling and experimental approaches to study particle deposition in the lungs.
- A review of the Fictitious Domain Method.
- The rotating micro-grid procedure for the accurate resolution of micro-particle dynamics in the respiratory airways. We extend the [Dechaume et al., 2010] micro-grid

idea by fixing the micro-grid with the particle in its spatial translation and rotation. We perform an Arbitrary Lagrangian-Eulerian Transformation of the Navier-Stokes equations from the moving grid to a fixed reference grid.

- An implementation of the rotating micro-grid procedure on unstructured grids. In order to increase the accuracy and performance of the Fictitious Domain Method [Veeramani et al., 2007], we propose to fit the complex particle surface geometry with the elements in the computational mesh fixed with the particle.

- Two numerical studies of problems involving dynamics of high aspect ratio particles in the lungs

- A finite element algorithm for simulations of coupled dynamics of inhaled air modeled as a Newtonian fluid and airway walls modeled as a hyperelastic solid in the acinar lung generations.

- Numerical simulations of three-dimensional rhythmically expanding alveolus that offered a good comparison with the available results in the literature [Sznitman et al., 2007; Henry et al., 2012].

- A computational model of a single alveolus that allow more detailed studies of impact of nonuniform lung expansion on the observed flow patterns in the pulmonary acini.

5.2 Future work

Based on the presented accomplishments, we consider the following next steps as promising future developments:

1. **Deposition of high-aspect ratio fibers in the pulmonary acinus**
   Here, the two numerical techniques presented in this thesis can be combined to simulate high aspect ratio particle transport in the alveolated ducts under the periodic breathing conditions. To our knowledge, such studies have never been conducted before, and the questions about trajectory reversibility and chaotic rotation of long curved fibers subjected to the flow conditions in rhythmically expanding alveoli are yet to be answered.

2. **Effect of a non-uniform lung expansion on the flow patterns in the alveoli**
   In our simple model of alveolated duct, we observe that the alveolar wall deformation

is larger distal to the duct inlet. Taking into account significant structural heterogeneity of the real alveolar walls and that the geometric hysteresis of lung expansion is a known fact, the effect of the non-uniform wall deformation on the alveolar flow patterns has to be studied in more details. Provided that there are evidences for significant change in the flow patterns, particle transport simulations can be performed to assess the effect of those changes on particle deposition.

3. Constitutive model for alveolar walls

Development of realistic constitutive models for alveolar tissues is instrumental for accurate modeling of the air transport and particle deposition in the terminal airways. Nevertheless, very little is known about the stresses in the alveolar walls, and this is another large challenge for future work.

4. Application of the FSI scheme to other biological and engineering flows

The presented FSI approach was developed without any assumptions restricting its use outside of the human respiratory system model. Therefore, it can be applied without significant modifications to study complex flows in irregular deformable domains, including but not limited to blood-heart interaction and evolution of the arterial aneurysms.

5. Convergence and stability studies

Since the schemes presented in this thesis, particularly the FSI scheme, rely on many novel numerical techniques, it is useful to study the convergence rates of the schemes with respect to the time step and spatial resolution. When no solid phase is present, we expect both schemes to have formal second order. When the solid is taken into account, the order should decrease due to many factors, including skipping the iterations while resolving the solid motion, errors in the fluid-structure interface resolution on the Eulerian mesh, errors due to interpolation between meshes, *etc.*

Finally, the interplay of many numerical parameters influences the stability of the FSI method. Particularly, the effect of the time step, Eulerian and Lagrangian grid resolution, the choice of the numerical integration scheme over the cut elements, problem reiterations and stress transfer methods should be studied together in order to estimate the stability restrictions for the scheme.

Bibliography

Anczurowski, E. and Mason, S. G. (1967). The kinetics of flowing dispersions III. Equilibrium orientations of rods and discs (experimental). *Journal of Colloid and Interface Science*, 23(4):533–546.

Anczurowski, E. and Mason, S. G. (1968). Particle Motions in Sheared Suspensions. XXIV. Rotation of Rigid Spheroids and Cylinders. *Journal of Rheology*, 12(2).

Asgharian, B. and Ahmadi, G. (1998). Effect of Fiber Geometry on Deposition in Small Airways of the Lung. *Aerosol Science and Technology*, 29(6):459–474.

Asgharian, B. and Anjilvel, S. (1995). The Effect of Fiber Inertia on Its Orientation in a Shear Flow with Application to Lung Dosimetry. *Aerosol Science and Technology*, 23(3):282–290.

Asgharian, B., Hofmann, W., and Bergmann, R. (2001). Particle Deposition in a Multiple-Path Model of the Human Lung. *Aerosol Science and Technology*, 34(4):332–339.

Asgharian, B. and Yu, C. (1988). Deposition of Inhaled Fibrous Particles in the Human Lung. *Journal of Aerosol Medicine*, 1(1):37–50.

Asgharian, B. and Yu, C. P. (1989). A Simplified Model of Interceptional Deposition of Fibers at Airway Bifurcations. *Aerosol Science and Technology*, 11(1):80–88.

Azhdarzadeh, M., Olfert, J. S., Vehring, R., and Finlay, W. H. (2014). Effect of Electrostatic Charge on Deposition of Uniformly Charged Monodisperse Particles in the Nasal Extrathoracic Airways of an Infant. *Journal of Aerosol Medicine and Pulmonary Drug Delivery*, 27(0):1–5.

Balásházy, I., Heistracher, T., and Hofmann, W. (1996). Air Flow and Particle Deposition Patterns in Bronchial Airway Bifurcations: The Effect of Different CFD Models and Bifurcation Geometries. *Journal of Aerosol Medicine*, 9(3):287–301.

Balásházy, I., Hofmann, W., Farkas, A., and Madas, B. G. (2008). Three-dimensional model for aerosol transport and deposition in expanding and contracting alveoli. *Inhalation Toxicology*, 20(6):611–21.

Balásházy, I., Martonen, T. B., and Hofmann, W. (1990). Fiber Deposition in Airway Bifurcations. *Journal of Aerosol Medicine*, 3(4):243–260.

Borojeni, A. A., Noga, M. L., Vehring, R., and Finlay, W. H. (2014). Measurements of total aerosol deposition in intrathoracic conducting airway replicas of children. *Journal of Aerosol Science*, 73:39–47.

Bower, A. F. (2009). *Applied Mechanics of Solids*. CRC Press.

Cai, F. and Yu, C. (1988). Inertial and interceptional deposition of spherical particles and fibers in a bifurcating airway. *Journal of Aerosol Science*, 19(6):679–688.

Cebral, J. R. and Summers, R. M. (2004). Tracheal and central bronchial aerodynamics using virtual bronchoscopy and computational fluid dynamics. *IEEE Transactions on Medical Imaging*, 23(8):1021–33.

Celik, I. B., Ghia, U., Roache, P. J., Freitas, C. J., Coleman, H., and Raad, P. E. (2008). Procedure for Estimation and Reporting of Uncertainty Due to Discretization in CFD Applications. *Journal of Fluids Engineering*, 130(7):078001.

Cheng, Y.-S., Yeh, H.-C., and Allen, M. D. (1988). Dynamic Shape Factor of a Plate-Like Particle. *Aerosol Science and Technology*, 8(2):109–123.

Choi, J.-I. and Kim, C. S. (2007). Mathematical Analysis of Particle Deposition in Human Lungs: An Improved Single Path Transport Model. *Inhalation Toxicology*, 19(11):925–939.

Cox, R. G. (1970). The motion of long slender bodies in a viscous fluid Part 1. General theory. *Journal of Fluid Mechanics*, 44(04):791–810.

Cox, R. G. (1971). The motion of long slender bodies in a viscous fluid. Part 2. Shear flow. *Journal of Fluid Mechanics*, 45(04):625–657.

Dahneke, B. (1982). Viscous Resistance of Straight-Chain Aggregates of Uniform Spheres. *Aerosol Science and Technology*, 1(2):179–185.

Darquenne, C. and Paiva, M. (1994). One-dimensional simulation of aerosol transport and deposition in the human lung. *Journal of Applied Physiology (Bethesda, Md. : 1985)*, 77(6):2889–98.

Dasi, L. P., Simon, H. A., Sucosky, P., and Yoganathan, A. P. (2009). Fluid mechanics of artificial heart valves. *Clinical and Experimental Pharmacology & Physiology*, 36(2):225–37.

Davies, C. (1979). Particle-fluid interaction. *Journal of Aerosol Science*, 10(5):477–513.

Dechaume, A., Finlay, W. H., and Minev, P. D. (2010). A two-grid fictitious domain method for direct simulation of flows involving non-interacting particles of a very small size. *International Journal for Numerical Methods in Fluids*, 63:1241–1255.

Diaz-Goano, C., Minev, P., and Nandakumar, K. (2003). A fictitious domain/finite element method for particulate flows. *Journal of Computational Physics*, 192(1):105–123.

Doorly, D. J., Taylor, D. J., and Schroter, R. C. (2008). Mechanics of airflow in the human nasal airways. *Respiratory Physiology & Neurobiology*, 163(1-3):100–10.

Edwards, D. A. (1994). A general theory of the macrotransport of nondepositing particles in the lung by convective dispersion. *Journal of Aerosol Science*, 25(3):543–565.

Emmett, P., Aitken, R., and Hannan, W. (1982). Measurements of the total and regional deposition of inhaled particles in the human respiratory tract. *Journal of Aerosol Science*, 13(6):549–560.

Finlay, W. H. (2001). *The Mechanics of Inhaled Pharmaceutical Aerosols*. Academic Press, London.

Finlay, W. H., Lange, C. F., King, M., and Speert, D. P. (2000). Lung delivery of aerosolized dextran. *American Journal of Respiratory and Critical Care Medicine*, 161(1):91–7.

Fok, T. F., Monkman, S., Dolovich, M., Gray, S., Coates, G., Paes, B., Rashid, F., Newhouse, M., and Kirpalani, H. (1996). Efficiency of aerosol medication delivery from a metered dose inhaler versus jet nebulizer in infants with bronchopulmonary dysplasia. *Pediatric Pulmonology*, 21(5):301–9.

Gans, R. (1928). Zur Theorie der Brownschen Molekularbewegung. *Annalen der Physik*, 391(12):628–656.

Geuzaine, C. and Remacle, J.-F. (2009). Gmsh: A 3-D finite element mesh generator with built-in pre- and post-processing facilities. *International Journal for Numerical Methods in Engineering*, 79(11):1309–1331.

Gil, J., Bachofen, H., Gehr, P., and Weibel, E. R. (1979). Alveolar volume-surface area relation in air- and saline-filled lungs fixed by vascular perfusion. *Journal of Applied Physiology: Respiratory, Environmental and Exercise Physiology*, 47(5):990–1001.

Glowinski, R., Pan, T.-W., Hesla, T., and Joseph, D. (1999). A distributed Lagrange multiplier/fictitious domain method for particulate flows. *International Journal of Multiphase Flow*, 25(5):755–794.

Glowinski, R., Pan, T.-W., and Periaux, J. (1994). A fictitious domain method for external incompressible viscous flow modeled by Navier-Stokes equations. *Computer Methods in Applied Mechanics and Engineering*, 112(1-4):133–148.

Golshahi, L. and Finlay, W. H. (2009). Recent Advances in Understanding Gas and Aerosol Transport in the Lungs: Application to Predictions of Regional Deposition. In Wang, L., editor, *Advances in Transport Phenomena*, volume 1 of *Advances in Transport Phenomena*, pages 1–30. Springer Berlin Heidelberg.

Golshahi, L., Noga, M. L., Vehring, R., and Finlay, W. H. (2013). An in vitro study on the deposition of micrometer-sized particles in the extrathoracic airways of adults during tidal oral breathing. *Annals of Biomedical Engineering*, 41(5):979–89.

Guermond, J., Minev, P., and Shen, J. (2006). An overview of projection methods for incompressible flows. *Computer Methods in Applied Mechanics and Engineering*, 195(44-47):6011–6045.

Guermond, J.-L. and Minev, P. (2013). Efficient Parallel Algorithms for Unsteady Incompressible Flows. In Iliev, O. P., Margenov, S. D., Minev, P. D., Vassilevski, P. S., and Zikatanov, L. T., editors, *Numerical Solution of Partial Differential Equations: Theory, Algorithms, and Their Applications SE - 10*, volume 45 of *Springer Proceedings in Mathematics & Statistics*, pages 185–201. Springer New York.

Guermond, J.-L. and Salgado, A. (2009). A splitting method for incompressible flows with variable density based on a pressure Poisson equation. *Journal of Computational Physics*, 228(8):2834–2846.

Haefeli-Bleuer, B. and Weibel, E. R. (1988). Morphometry of the human pulmonary acinus. *The Anatomical Record*, 220(4):401–14.

Hammersley, J. R. and Olson, D. E. (1992). Physical models of the smaller pulmonary airways. *Journal of Applied Physiology*, 72(6):2402–2414.

Harris, R. and Fraser, D. (1976). A model for deposition of fibers in the human respiratory system. *American Industrial Hygiene Association Journal*, 37(2):73–89.

Harris Jr, R. and Timbrell, V. (1975). The influence of fibre shape in lung deposition-mathematical estimates. *Inhaled Particles*, 4:75.

Hegedűs, C., Balásházy, I., and Farkas, A. (2004). Detailed mathematical description of the geometry of airway bifurcations. *Respiratory Physiology & Neurobiology*, 141(1):99–114.

Heil, M. and Hazel, A. L. (2011). Fluid-Structure Interaction in Internal Physiological Flows. *Annual Review of Fluid Mechanics*, 43(1):141–162.

Heistracher, T. and Hofmann, W. (1995). Physiologically realistic models of bronchial airway bifurcations. *Journal of Aerosol Science*, 26(3):497–509.

Henry, F. S., Butler, J. P., and Tsuda, a. (2002). Kinematically irreversible acinar flow: a departure from classical dispersive aerosol transport theories. *Journal of Applied Physiology (Bethesda, Md. : 1985)*, 92(2):835–45.

Henry, F. S., Haber, S., Haberthür, D., Filipovic, N., Milasinovic, D., Schittny, J. C., and Tsuda, a. (2012). The simultaneous role of an alveolus as flow mixer and flow feeder for the deposition of inhaled submicron particles. *Journal of Biomechanical Engineering*, 134(12):121001.

Heyder, J., Blanchard, J. D., Feldman, H. A., and Brain, J. D. (1988). Convective mixing in human respiratory tract: estimates with aerosol boli. *Journal of Applied Physiology*, 64(3):1273–1278.

Heyder, J. and Gebhart, J. (1977). Gravitational deposition of particles from laminar aerosol flow through inclined circular tubes. *Journal of Aerosol Science*, 8(4):289–295.

Hinds, W. C. (1999). *Aerosol Technology: Properties, Behavior, and Measurement of Airborne Particles*. Wiley–Interscience, 2nd edition.

Horsfield, K., Dart, G., Olson, D. E., Filley, G. F., and Cumming, G. (1971). Models of the human bronchial tree. *Journal of Applied Physiology*, 31(2):207–217.

Humphrey, J. D. and Taylor, C. A. (2008). Intracranial and abdominal aortic aneurysms: similarities, differences, and need for a new class of computational models. *Annual Review of Biomedical Engineering*, 10:221–46.

Hwang, C. Y. (1983). Size and shape of airborne asbestos fibres in mines and mills. *British Journal of Industrial Medicine*, 40(3):273–9.

Inthavong, K., Tu, J., and Ahmadi, G. (2009). Computational Modelling of Gas-Particle Flows with Different Particle Morphology in the Human Nasal Cavity. *The Journal of Computational Multiphase Flows*, 1(1):57–82.

Jaques, P. A. and Kim, C. S. (2000). Measurement of total lung deposition of inhaled ultrafine particles in healthy men and women. *Inhalation Toxicology*, 12(8):715–731.

Javaheri, E., Golshahi, L., and Finlay, W. (2013). An idealized geometry that mimics average infant nasal airway deposition. *Journal of Aerosol Science*, 55:137–148.

Jeffery, G. B. (1922). The Motion of Ellipsoidal Particles Immersed in a Viscous Fluid. *Proceedings of the Royal Society of London. Series A, Containing Papers of a Mathematical and Physical Character (1905-1934)*, 102(715):161–179.

Johnson, D. L., Leith, D., and Reist, P. C. (1987). Drag on non-spherical, orthotropic aerosol particles. *Journal of Aerosol Science*, 18(1):87–97.

Kelly, J. T., Asgharian, B., Kimbell, J. S., and Wong, B. a. (2004). Particle Deposition in Human Nasal Airway Replicas Manufactured by Different Methods. Part I: Inertial Regime Particles. *Aerosol Science and Technology*, 38(11):1063–1071.

Kim, C. and Hu, S. (1998). Regional deposition of inhaled particles in human lungs: comparison between men and women. *Journal of Applied Physiology*, pages 1834–1844.

Kumar Mahto, S., Tenenbaum-Katan, J., and Sznitman, J. (2012). Respiratory physiology on a chip. *Scientifica*, 2012.

Li, J. J., Muralikrishnan, S., Ng, C.-T., Yung, L.-Y. L., and Bay, B.-H. (2010). Nanoparticle-induced pulmonary toxicity. *Experimental Biology and Medicine (Maywood, N.J.)*, 235(9):1025–33.

Liu, Y., Matida, E. A., Gu, J., and Johnson, M. R. (2007). Numerical simulation of aerosol deposition in a 3-D human nasal cavity using RANS, RANS/EIM, and LES. *Journal of Aerosol Science*, 38(7):683–700.

Longest, P. W. and Xi, J. (2007). Computational investigation of particle inertia effects on submicron aerosol deposition in the respiratory tract. *Journal of Aerosol Science*, 38(1):111–130.

Ma, B. and Darquenne, C. (2012). Aerosol bolus dispersion in acinar airways–influence of gravity and airway asymmetry. *Journal of Applied Physiology (Bethesda, Md. : 1985)*, 113(3):442–50.

Martin, A. R. and Finlay, W. H. (2008a). Enhanced deposition of high aspect ratio aerosols in small airway bifurcations using magnetic field alignment. *Journal of Aerosol Science*, 39(8):679–690.

Martin, A. R. and Finlay, W. H. (2008b). Magnetic Alignment of Aerosol Particles for Targeted Pulmonary Drug Delivery: Comparison of Magnetic and Aerodynamic Torques. *Journal of Computational and Theoretical Nanoscience*, 5(10):2067–2070.

Martinez, R. C., Roshchenko, A., Minev, P. D., and Finlay, W. H. (2013). Simulation of enhanced deposition due to magnetic field alignment of ellipsoidal particles in a lung bifurcation. *Journal of Aerosol Medicine and Pulmonary Drug Delivery*, 26(1):31–40.

Miki, H., Butler, J. P., Rogers, R. A., and Lehr, J. L. (1993). Geometric hysteresis in pulmonary surface-to-volume ratio during tidal breathing. *Journal of Applied Physiology (Bethesda, Md. : 1985)*, 75(4):1630–6.

Minev, P. and Ross Ethier, C. (1998). A characteristic/finite element algorithm for the 3-D Navier-Stokes equations using unstructured grids. *Computer Methods in Applied Mechanics and Engineering*, 178(1-2):39–50.

Myojo, T. (1987). Deposition of fibrous aerosol in model bifurcating tubes. *Journal of Aerosol Science*, 18(3):337–347.

Nowak, N., Kakade, P. P., and Annapragada, A. V. (2003). Computational Fluid Dynamics Simulation of Airflow and Aerosol Deposition in Human Lungs. *Annals of Biomedical Engineering*, 31(4):374–390.

Oldham, M. J., Mannix, R. C., and Phalen, R. F. (1997). Deposition of monodisperse particles in hollow models representing adult and child-size tracheobronchial airways. *Health Physics*, 72(6):827–834.

Oldham, M. J. and Phalen, R. F. (2002). Dosimetry implications of upper tracheobronchial airway anatomy in two mouse varieties. *The Anatomical Record*, 268(1):59–65.

Oseen, C. W. (1927). *Neuere Methoden und Ergebnisse in der Hydrodynamik*. Akademische Verlagsgesellschaft m. b. h., Leipzig.

Pilou, M., Antonopoulos, V., Makris, E., Neofytou, P., Tsangaris, S., and Housiadas, C. (2013). A fully Eulerian approach to particle inertial deposition in a physiologically realistic bifurcation. *Applied Mathematical Modelling*, 37(8):5591–5605.

Podgórski, A. and Gradon, L. (1990). Motion and deposition of fibrous flexible particles in laminar gas flow through a pipe. *Journal of Aerosol Science*, 21(7):957–967.

Podgórski, A. and Gradon, L. (1998). Mechanics of a Deformable Fibrous Aerosol Particle: General Theory and Application to the Modeling of Air Filtration. In Spurny, K. R., editor, *Advances in Aerosol Gas Filtration*, chapter 10, pages 193—-218. CRC Press.

Redman, G. E. S., Martin, A. R., Waszak, P., Thompson, R. B., Cheung, P.-Y., Thébaud, B., and Finlay, W. H. (2011). Pilot Study of Inhaled Aerosols Targeted via Magnetic Alignment of High Aspect Ratio Particles in Rabbits. *Journal of Nanomaterials*, 2011:1–7.

Sforza, D. M., Putman, C. M., and Cebral, J. R. (2009). Hemodynamics of Cerebral Aneurysms. *Annual Review of Fluid Mechanics*, 41:91–107.

Shang, Y., Finlay, W., and Moussa, W. (2008). Numerical analysis of thermally induced micro fiber deformation using a high frequency magnetic field in human lung. *Journal of Computational and Theoretical Nanoscience*, 5(3):294–301.

Stapleton, K., Guentsch, E., Hoskinson, M., and Finlay, W. (2000). On the suitability of k–ϵ turbulence modeling for aerosol deposition in the mouth and throat: a comparison with experiment. *Journal of Aerosol Science*, 31(6):739–749.

Sturm, R. (2014). Aerosol Bolus Inhalation as Technique for the Diagnosis of Various Lung Diseases–A Theoretical Approach. *Computational and Mathematical Biology*, 3(2).

Sturm, R. and Hofmann, W. (2006). A computer program for the simulation of fiber deposition in the human respiratory tract. *Computers in Biology and Medicine*, 36(11):1252–67.

Su, W.-C. and Cheng, Y. S. (2009). Deposition of man-made fibers in human respiratory airway casts. *Journal of Aerosol Science*, 40(3):270–284.

Subramanian, G. and Koch, D. L. (2005). Inertial effects on fibre motion in simple shear flow. *Journal of Fluid Mechanics*, 535:383–414.

Sugiyama, K., Ii, S., Takeuchi, S., Takagi, S., and Matsumoto, Y. (2011). A full Eulerian finite difference approach for solving fluid–structure coupling problems. *Journal of Computational Physics*, 230(3):596–627.

Sznitman, J. (2013). Respiratory microflows in the pulmonary acinus. *Journal of Biomechanics*, 46(2):284–98.

Sznitman, J., Heimsch, F., Heimsch, T., Rusch, D., and Rösgen, T. (2007). Three-dimensional convective alveolar flow induced by rhythmic breathing motion of the pulmonary acinus. *Journal of Biomechanical Engineering*, 129(5):658–65.

Tawhai, M. H. and Lin, C.-L. (2011). Airway gas flow. *Comprehensive Physiology*, 1(3):1135–57.

Timbrell, V. (1970). The inhalation of fibres. In SHAPIRO, H. A., editor, *Pneumoconiosis: Proceedings of the International Conference, Johannesburg, 1969*, pages 3–12. Oxford University Press.

Tsuda, A., Henry, F., and Butler, J. (2008). Gas and aerosol mixing in the acinus. *Respiratory Physiology & Neurobiology*, 163(0):139–149.

Tsuda, A., Henry, F. S., and Butler, J. P. (1995). Chaotic mixing of alveolated duct flow in rhythmically expanding pulmonary acinus. *Journal of Applied Physiology (Bethesda, Md. : 1985)*, 79(3):1055–63.

Tsuda, A., Rogers, R. A., Hydon, P. E., and Butler, J. P. (2002). Chaotic mixing deep in the lung. *Proceedings of the National Academy of Sciences of the United States of America*, 99(15):10173–8.

van de Vosse, F. N. and Stergiopulos, N. (2011). Pulse Wave Propagation in the Arterial Tree. *Annual Review of Fluid Mechanics*, 43(1):467–499.

Veeramani, C., Minev, P., and Nandakumar, K. (2007). A fictitious domain formulation for flows with rigid particles: A non-Lagrange multiplier version. *Journal of Computational Physics*, 224(2):867–879.

Wall, W. and Rabczuk, T. (2008). Fluid–structure interaction in lower airways of CT-based lung geometries. *International Journal for Numerical Methods in Fluids*, 57(5):653–675.

Wall, W., Wiechert, L., Comerford, A., and Rausch, S. (2010). Towards a comprehensive computational model for the respiratory system. *International Journal for Numerical Methods in Biomedical Engineering*, 26(7):807–827.

Weibel, E. R. (1986). Functional Morphology of Lung Parenchyma. In *Comprehensive Physiology*. John Wiley & Sons, Inc.

Weinberg, E. J., Shahmirzadi, D., and Mofrad, M. R. K. (2010). On the multiscale modeling of heart valve biomechanics in health and disease. *Biomechanics and Modeling in Mechanobiology*, 9(4):373–87.

Xi, J., Kim, J., Si, X. a., Su, W. C., and Zhou, Y. (2014). Effects of the facial interface on inhalation and deposition of micrometer particles in calm air in a child airway model. *Inhalation Toxicology*, 26(8):492–505.

Yeh, H. and Schum, G. (1980). Models of human lung airways and their application to inhaled particle deposition. *Bulletin of Mathematical Biology*, 42(3):461–480.

Zhang, L., Cui, T., and Liu, H. (2009a). A set of symmetric quadrature rules on triangles and tetrahedra. *Journal of Computational Mathematics*, 27(1):89–96.

Zhang, Y. and Finlay, W. (2005). Experimental measurements of particle deposition in three proximal lung bifurcation models with an idealized mouth-throat. *Journal of Aerosol Medicine*, 18(4):460–473.

Zhang, Z. and Kleinstreuer, C. (2004). Airflow structures and nano-particle deposition in a human upper airway model. *Journal of Computational Physics*, 198(1):178–210.

Zhang, Z., Kleinstreuer, C., and Kim, C. S. (2009b). Comparison of analytical and CFD models with regard to micron particle deposition in a human 16-generation tracheobronchial airway model. *Journal of Aerosol Science*, 40(1):16–28.

Zhao, H., Freund, J. B., and Moser, R. D. (2008). A fixed-mesh method for incompressible flow-structure systems with finite solid deformations. *Journal of Computational Physics*, 227(6):3114–3140.

Zhou, Y., Su, W.-C., and Cheng, Y. S. (2008). Fiber deposition in the tracheobronchial region: deposition equations. *Inhalation Toxicology*, 20(13):1191–8.

Zienkiewicz, O., Taylor, R., and Zhu, J. (2013). *The Finite Element Method: its Basis and Fundamentals*. Elsevier.

Zienkiewicz, O. and Zhu, J. (1992). The superconvergent patch recovery and a posteriori error estimates. Part 1: The recovery technique. *Journal for Numerical Methods in Engineering*, 33:1331–1364.